



SINGLET DELTA OXYGEN: A QUANTITATIVE ANALYSIS USING
OFF-AXIS INTEGRATED-CAVITY-OUTPUT-SPECTROSCOPY (ICOS)

THESIS

Jeffrey E Gallagher, Captain, USAF

AFIT/GAP/ENP/06-05

DEPARTMENT OF THE AIR FORCE
AIR UNIVERSITY

AIR FORCE INSTITUTE OF TECHNOLOGY

Wright-Patterson Air Force Base, Ohio

APPROVED FOR PUBLIC RELEASE; DISTRIBUTION UNLIMITED

The views expressed in this thesis are those of the author and do not reflect the official policy or position of the United States Air Force, the Department of Defense or the United States Government.

AFIT/GAP/ENP/06-05

SINGLET DELTA OXYGEN: A QUANTITATIVE ANALYSIS USING
OFF-AXIS INTEGRATED-CAVITY-OUTPUT-SPECTROSCOPY (ICOS)

THESIS

Presented to the Faculty
Department of Engineering Physics
Graduate School of Engineering and Management
Air Force Institute of Technology
Air University
Air Education and Training Command
In Partial Fulfillment of the Requirements for the
Degree of Master of Science (Applied Physics)

Jeffrey E Gallagher
Captain, USAF

March 2006

APPROVED FOR PUBLIC RELEASE; DISTRIBUTION UNLIMITED

SINGLET DELTA OXYGEN: A QUANTITATIVE ANALYSIS USING
OFF-AXIS INTEGRATED-CAVITY-OUTPUT-SPECTROSCOPY (ICOS)

Jeffrey E Gallagher
Captain, USAF

Approved:

/signed/ _____ Glen P. Perram (Chairman)	03 Mar 2006 _____ date
/signed/ _____ Paul J. Wolf (Member)	03 Mar 2006 _____ date
/signed/ _____ David E. Weeks (Member)	03 Mar 2006 _____ date
/signed/ _____ Skip Williams (Member)	03 Mar 2006 _____ date

Abstract

A new spectroscopic technique applicable to the detection of ultra-weak and forbidden molecular transitions is presented. The method is based on off-axis integrated-cavity-output spectroscopy (ICOS) and has been applied to the detection of singlet ($a^1\Delta_g$) oxygen in the (1,0) band of the electric-quadrupole allowed Noxon system ($b^1\Sigma_g^+ \leftarrow a^1\Delta_g$) of oxygen. The details of the method as well as spectroscopic data confirming the absolute line positions of twenty-one lines in the (1,0) band of the $b^1\Sigma_g^+ \leftarrow a^1\Delta_g$ have been completed to within 0.004 cm^{-1} . A Boltzmann analysis verified previously calculated and unproven integrated cross sections for each of the lines. Ten lines were also pressure broadened from 25 Torr to 100 Torr, and pressure broadening coefficients were determined from $\gamma_p = 3.61 \times 10^{-6}\text{ cm}^{-1}/\text{torr}$ to $5.81 \times 10^{-6}\text{ cm}^{-1}/\text{torr}$. These coefficients illustrate that rotationally-inelastic collisions are the dominant mechanism in molecular pressure broadening. The singlet oxygen was generated in a microwave plasma and the afterglow passed through an off-axis ICOS measurement system consisting of an 82 cm long, high-finesse ($F \approx 248000$) optical cavity. The mirror reflectivity, R , was determined by performing a cavity-ringdown measurement and observing ringdown times of $220\text{ }\mu\text{s}$ in a range from 1494 nm to 1512 nm. The diode laser was current tuned over ca. 0.33 cm^{-1} at 5-25 Hz. Light exiting the cavity was focused onto an InGaAs detector, and the cavity transmission was recorded as a function of laser frequency. The absorption within the cavity leads to a decrease in transmitted intensity, ΔI , given by $\frac{\Delta I}{I_o} = \frac{GA}{1+GA}$, where I_o is incident laser intensity, A is the single-pass absorption ($\approx 5 \times 10^{-8}$), and $G = \frac{2R^2}{1-R^2} \approx 80,000$ is the cavity enhancement factor.

Acknowledgements

I want to thank Dr. Skip Williams of the Air Force Research Lab for being my instructor and mentor. His experience, guidance, enthusiasm and dedication not only made this thesis possible, but also allowed me to learn a great deal on the subject of spectroscopy.

I want to thank Dr Glen Perram for coaching me through various theories of molecular spectroscopy. Without his insight, my level of comprehension would indeed be much lower.

I owe a great deal a gratitude to my wife and children for their understanding and encouragement through my whole experience here at AFIT. Without the love and spiritual support from my wife, I know for a fact that I would not be where I am today.

Most importantly of all, I want to thank my God for being with me every step of the way. I thank Him and praise Him for lifting me up whenever I fell. All I had to do was call on Him, and He was there.

Jeffrey E Gallagher

Table of Contents

	Page
Abstract	iv
Acknowledgements	v
List of Figures	viii
List of Tables	xi
List of Symbols	xii
List of Abbreviations	xvi
 I. Introduction	 1
1.1 Research Goals	1
1.2 Benefits to the DoD	1
1.2.1 The Chemical Oxygen-Iodine Laser	2
1.2.2 Atmospheric Modeling	3
1.2.3 Other Benefits	3
 II. Background	 4
2.1 History of Detecting the $b^1\Sigma_g^+ \leftarrow a^1\Delta_g$ Transition of Oxygen	4
2.2 History of Cavity Ringdown	7
2.3 History of Off-axis ICOS	7
2.4 Physical Theory	9
2.4.1 The Transition	9
2.4.2 The Electric-Quadrupole Moment	10
2.4.3 Angular Momentum in Molecules	12
2.4.4 Symmetry Operations and Properties	15
2.4.5 The Herzberg Diagram and Selection Rules	16
2.5 Spectral Lineshape Theory	19
2.5.1 Line Widths	19
2.5.2 Absorption Parameters	22
2.5.3 Pressure Broadening	24

	Page
III. Experimental Approach	25
3.1 Multi-Pass Absorption Spectroscopy	25
3.1.1 The Cavity RingDown	25
3.1.2 Off-Axis ICOS	29
3.2 The Apparatus	30
3.2.1 The Diode Lasers	32
3.3 Procedure	33
3.3.1 Calibration of Lasers	33
3.3.2 Optimization	34
3.3.3 Taking Data	41
3.3.4 Analyzing Data	43
IV. Results and Discussion	49
4.1 The Absolute Line Positions	49
4.2 Verification of the Integrated Absorption Cross Sections	51
4.2.1 Boltzmann Analysis	52
4.3 Pressure Dependence of Line Width (FWHM)	55
4.3.1 Rotational (J) Dependence on Pressure Broadening Coefficients	58
V. Summary and Recommendations	61
5.1 Summary	61
5.2 Recommendations For Further Research	63
Appendix A. Mathematical Development of GA	64
A.1 Beers Law to Off-Axis ICOS Theory	64
Appendix B. Term and Band Energies	71
B.1 Matlab Code	71
B.2 The Theoretical Term Energies	72
B.3 The Predicted Band Energies	73
Appendix C. Analyzed Data	76
Appendix D. Developing the Hamiltonian	87
D.1 The Rigid Rotor to the Case (a) Hamiltonian	87
Bibliography	91

List of Figures

Figure		Page
2.1.	John Noxon's emission spectra of the transition from $O_2(b)$ to $O_2(a)$. [15]	4
2.2.	Group from Germany and Canada detected all five branches using a fourier transform spectrometer. They achieved a resolution of $0.2cm^{-1}$ and were the first to validate the relative signal strength intensities among the rotational lines. [6]	5
2.3.	The Russians were the first to detect the absorption lines of the Noxon system. They used a technique called intra-cavity absorption spectroscopy and they achieved a resolution of $0.018cm^{-1}$. [18]	6
2.4.	Williams <i>et al</i> was the first to detect the (1,0) band of the Q branch. Williams used O'Keefe's off-axis ICOS technique to finely resolve the rotational lines. [24]	6
2.5.	Williams <i>et al</i> used the off-axis ICOS technique to finely resolve the (0,0) band of the Q branch. [13]	6
2.6.	Here is a basic schematic of the off-axis ICOS technique . The cavity outputs are collected and integrated to acquire the absorption feature.	8
2.7.	The first five electronic states of oxygen. [2]	9
2.8.	Vector diagram for a homonuclear diatomic [Hund's case(a)]. [25]	13
2.9.	Vector diagram for a homonuclear diatomic [Hund's case(b)]. [25]	15
2.10.	This is the Herzberg diagram for the $b^1\Sigma_g^+ \leftarrow a^1\Delta_g$ transition. This diagram is a handy tool for displaying the allowed rotational transitions which come about from the various selection rules for this particular transition. [8]	17
2.11.	This is a general line profile. [4]	20
2.12.	The Voigt profile. [4]	22
3.1.	The 1/e point on the downward curve of this square wave is where the ringdown time is measured. Although the x-axis is currently in point-space, this axis can be better thought of as a time axis for this example.	26

Figure		Page
3.2.	This is the experiment setup. The length of the optical cavity is 82 cm, the microwave power supply operated at 80 W, and the average pressure in the cavity was ca. 23 torr.	31
3.3.	Temperature dependence for the 1499.71 nm laser	34
3.4.	Flow rate dependence for singlet delta oxygen	36
3.5.	Relationship between the intensity of the signal and the number density of $O_2(a)$	36
3.6.	This is the Q8 line scanned at 25 Hz. Total pressure in the cavity was ca. 25 torr, with a ringdown time of 203 μ s. The data was averaged 10000 times and binned 40 times.	40
3.7.	This is the Q8 line scanned at 10 Hz. Total pressure in the cavity was ca. 25 torr, with a ringdown time of 203 μ s. The data was averaged 4000 times and binned 100 times.	40
3.8.	This is the Q8 line scanned at 5 Hz. Total pressure in the cavity was ca. 25 torr, with a ringdown time of 203 μ s. The data was averaged 1000 times and binned 200 times.	41
3.9.	The ringdown curve for $\tau = 219 \mu$ s.	42
3.10.	The raw data for R(7) with the etalon function.	44
3.11.	The etalon is used to convert the R(7) data to frequency-space.	44
3.12.	The absorbance is calculated.	46
3.13.	The baseline is removed and the R(7) peak is all that remains.	47
3.14.	A Voigt profile is fit to the peak and the peak cross section is calculated. This is the final step in the analysis process.	48
4.1.	The Q(8) line position at $6639.9878 cm^{-1}$. The total pressure in the cavity was ca. 25 torr, the ringdown time was 216 μ s, and the rep rate was 25 Hz. The data was binned 50 times.	52
4.2.	Boltzmann analysis.	54
4.3.	The Q(8) line pressure broadened at 25 Torr	55
4.4.	The Q(8) line pressure broadened at 50 Torr	56
4.5.	The Q(8) line pressure broadened at 75 Torr	56
4.6.	The Q(8) line pressure broadened at 100 Torr	57

Figure		Page
4.7.	Slope of regression line is the pressure broadening coefficient in $cm^{-1} Torr^{-1}$	58
4.8.	Rotational dependence on the pressure broadening coefficients.	60
C.1.	The O(6) line position at $6611.1418cm^{-1}$	76
C.2.	The O(8) line position at $6598.8226cm^{-1}$	77
C.3.	The P(9) line position at $6614.4826cm^{-1}$	77
C.4.	The P(13) line position at $6599.3977cm^{-1}$	78
C.5.	The P(15) line position at $6591.3228cm^{-1}$	78
C.6.	The Q(2) line position at $6642.9513cm^{-1}$	79
C.7.	The Q(4) line position at $6642.3227cm^{-1}$	79
C.8.	The Q(6) line position at $6641.3324cm^{-1}$	80
C.9.	The Q(8) line position at $6639.9878cm^{-1}$	80
C.10.	The Q(10) line position at $6638.2786cm^{-1}$	81
C.11.	The Q(12) line position at $6636.2118cm^{-1}$	81
C.12.	The Q(14) line position at $6633.7802cm^{-1}$	82
C.13.	The Q(16) line position at $6630.9987cm^{-1}$	82
C.14.	The R(3) line position at $6653.6667cm^{-1}$	83
C.15.	The R(7) line position at $6662.6576cm^{-1}$	83
C.16.	The R(9) line position at $6666.6174cm^{-1}$	84
C.17.	The R(11) line position at $6670.2048cm^{-1}$	84
C.18.	The R(13) line position at $6673.4308cm^{-1}$	85
C.19.	The R(17) line position at $6678.7650cm^{-1}$	85
C.20.	The R(19) line position at $6680.8693cm^{-1}$	86
C.21.	The S(8) line position at $6692.1316cm^{-1}$	86

List of Tables

Table		Page
3.1.	Lines that are within the safe temperature range for the 1499.71 nm tunable laser diode.	34
3.2.	List of the slopes and y-intercepts obtained for the five lasers.	35
4.1.	Absolute Line Positions in Wavenumbers (cm^{-1}).	50
4.2.	Verified Integrated Cross Sections ($\frac{cm^2}{cm^{-1}}$).	53
4.3.	Pressure Broadening Coefficients.	59

List of Symbols

Symbol		Page
$b^1\Sigma_g^+ \leftarrow a^1\Delta_g$	The Noxon System	1
$O_2(a^1\Delta_g)$	Singlet Delta Oxygen (1^{st} excited state)	2
$O_2(a)$	Singlet Delta Oxygen	2
$O_2(b)$	Singlet Sigma (2^{nd} excited state)	9
$\phi(r)$	An arbitrary scalar potential of an electric field	10
ϵ_0	Permittivity of free space	10
r	Distance from source charge q_i , to test charge P	10
r_i	Distance from origin to source charge q_i	10
q_i	The i^{th} electron charge	10
θ_i	The angle that test charge P makes with respect to the source charge q_i and origin	10
Q_{jk}	Component of the electric quadrupole moment tensor . . .	10
j_i and k_i	Spatial indices	10
δ_{jk}	Kronecker delta	10
l_j and l_k	Direction cosines	11
Q_{jk}^a	Components of an axially symmetric electric quadrupole moment tensor	11
Ω	Total electronic angular momentum about the internuclear axis	13
\mathbf{J}	Total orbital angular momentum	13
\mathbf{L}	Electronic orbital angular momentum	13
\mathbf{S}	Electronic spin angular momentum	13
Λ	Internuclear axis component of \mathbf{L}	13
Σ	Internuclear axis component of \mathbf{S}	13
\mathbf{R}	Angular momentum of nuclear rotation	13
$F(J)$	Rotational eigenenergies	13

Symbol		Page
B_v	Rotational constant	13
$C\Lambda^2$	Spin-orbit coupling term	13
D_v	Centrifugal distortion constant	14
\mathbf{K}	Total angular momentum without spin	15
$S_{J'J''}$	Signal strength intensity	15
σ	Absorption cross section	15
$D_{\infty h}$	A point group from group theory	15
$\hat{\sigma}$	Rotation operator	15
\hat{C}_n	Reflection operator	15
\hat{i}	Inversion operator	15
Q_{ba}	Scalar electric-quadrupole moment	16
\hat{Q}	Electric-quadrupole moment operator	16
\mathbf{I}	Nuclear spin angular momentum	17
ψ_{Tot}	Total wavefunction	17
ψ_{el}	Electronic wavefunction	17
ψ_{vib}	Vibrational wavefunction	17
ψ_{nuc}	Nuclear wavefunction	17
ψ_{rot}	Rotational wavefunction	17
φ	Angle made by \mathbf{L} from some reference point on the circle traced out by the precession of \mathbf{L} about the internuclear axis to the current point on the circle that \mathbf{L} is now pointing	18
a and b	Arbitrary constants	18
ν	Frequency	19
ΔE	Energy of the gap	19
E_i	Energy of the upper state	19
E_k	Energy of the lower state	19
ν_0	Central frequency	19
$\Delta\nu$	FWHM or HWHM in general	19

Symbol		Page
τ_{sp}	Spontaneous lifetime	20
m	Mass of the molecule	21
c	Speed of light in a vacuum	21
k	Boltzmann's constant	21
T	Temperature	21
α_0	Area under the Voigt profile	21
$\Delta\nu_L$	HWHM of the Lorentzian	21
$\Delta\nu_D$	HWHM of the Gaussian or Doppler width	21
F	Flux	22
h	Planck's constant	22
α	Absorption coefficient	22
σ_I	Integrated absorption cross section	22
$B_{b\leftarrow a}$	Einstein coefficient for absorption between state's a and b	22
ρ	Radiation density	22
N_a and N_b	Number densities of lower and upper state respectively . .	22
$g(\nu - \nu_{ba})$	Line function	23
σ	Absorption cross section	24
R	Reflectivity	27
N	Number of trips in the optical cavity	27
τ	Ringdown time	27
L	Length of the optical cavity	27
G	Cavity enhancement factor	30
A	Single-pass absorption	30
ΔI	Change in the steady-state signal output intensity	30
$I(\alpha L = 0)$	Signal intensity through cavity in absence of absorber, α .	30
$I(\alpha L)$	Signal intensity through the cavity with the absorber present	30
f_B	Boltzmann factor	52
E_J	Rotational energy	52

Symbol		Page
$[O_2(a)]$	Concentration of $O_2(a)$	52
γ_p	Pressure broadening coefficient	57
p	Pressure in torr	57

List of Abbreviations

Abbreviation		Page
SOG	Singlet Oxygen Generator	3
RDC	Ringdown Cavity	7
CRDS	Cavity Ringdown Spectroscopy	7
ICOS	Integrated-Cavity-Output-Spectroscopy	7
FWHM	Full Width at Half Maximum	19
HWHM	Half Width at Half Maximum	19
FSR	Free Spectral Range	29
SPA	Single-Pass Absorption	46
SNR	Signal to Noise Ratio	51

SINGLET DELTA OXYGEN: A QUANTITATIVE ANALYSIS USING OFF-AXIS INTEGRATED-CAVITY-OUTPUT-SPECTROSCOPY (ICOS)

I. Introduction

The $b^1\Sigma_g^+ \leftarrow a^1\Delta_g$ system of oxygen is an electric-quadrupole transition and is therefore very weak and extremely difficult to detect. In addition, this particular absorption band (referred to as the Noxon Band after John Noxon [15]) has a radiative lifetime of about 72 minutes [7], which classifies this as a metastable species. Measuring the absorption of a metastable species is in itself very difficult. This weak signal combined with the long lifetime is why these transitions have not been directly observed until quite recently [24]. The research goals for this experiment and the benefits to the Department of Defense (DoD) are explained in the following sections.

1.1 *Research Goals*

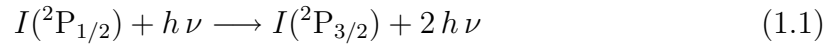
The primary goal for this research effort is to utilize a relatively new spectroscopic technique and demonstrate it's ability to provide quantitative data of singlet delta oxygen. This thesis will focus on three areas of characterization to achieve this goal. First, the absolute line positions will be determined and compared to values derived from the most recent theory. Second, the integrated absorption cross-sections will be verified using Boltzmann analysis. Finally, pressure broadening coefficients will be determined for select lines using a range of pressures from 25 to 100 Torr. After the coefficients are determined, this experiment will hope to be the first in discerning a rotational dependence on pressure broadening for an electric-quadrupole allowed transition.

1.2 *Benefits to the DoD*

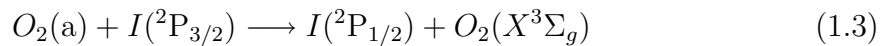
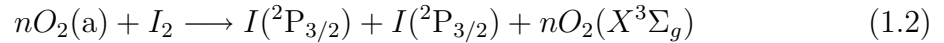
The DoD is concerned about characterizing singlet delta oxygen because this knowledge will help diagnose the collisional environment of the Chemical Oxygen-

Iodine Laser (COIL). Additional areas that singlet delta oxygen ($O_2(a)$) plays a role in include biological weapons detection, satellite communications, semiconductor technology, and propulsion systems.

1.2.1 The Chemical Oxygen-Iodine Laser. The COIL as a mega-watt class chemical laser that is currently being integrated onto an aircraft for the purpose of missile defense called the Airborne Laser program or ABL. The production of singlet delta oxygen [$O_2(a^1\Delta_g)$], or simply $O_2(a)$, is a very important part of the lasing process in the COIL since this is the molecule used as the energy reservoir due to it's long lifetime. As the $O_2(a)$ goes through the supersonic nozzle, gaseous Iodine is introduced into the system where the $O_2(a)$ eventually transfers it's energy in a near-resonant collision to a dissociated Iodine atom ($I(^2P_{3/2})$). The actual lasing transition occurs between $I(^2P_{1/2})$ and $I(^2P_{3/2})$, in the following process,



$O_2(a)$, however, plays a crucial role in a series of chemical reactions which lead to the production of the needed excited Iodine atom, $I(^2P_{1/2})$ [13].



The n is used in equation 1.2 because more than one $O_2(a)$ molecules are required to disassociate the Iodine molecule. In equation 1.3 the $O_2(a)$ molecule reacts with $I(^2P_{3/2})$ in a near resonant transfer to produce ground state oxygen $O_2(X)$ and the desired $I(^2P_{1/2})$. It is therefore very important to understand the properties of $O_2(a)$ in order to better control its production. Scientists and engineers in the COIL community are striving for a method to directly measure the concentration of $O_2(a)$ prior

to the lasing process. The singlet oxygen generator (SOG) used in the current COIL is believed to produce high yields of $O_2(a)$ molecules because of the following reaction. It produces only $O_2(a)$. The off-axis ICOS apparatus used in this experiment will be able to quantify the number density of this $O_2(a)$ production prior to entering the nozzle assembly. The research and technique used in this thesis will help develop that method.

1.2.2 Atmospheric Modeling. In the upper atmosphere, namely the thermosphere, singlet delta oxygen is fairly abundant and contributes strongly to the radiation transfer which takes place there. Much like the COIL, the kinetics involved in the thermosphere are not completely understood. Consequently, gaining a better understanding of the earth's atmosphere will be very important and would improve our satellite communications network and other forms of energy propagating through the atmosphere.

1.2.3 Other Benefits. On the topic of biological weapons detection, it has been shown that air plasmas produce large quantities of $O_2(a)$ with demonstrated reactivity with hydrocarbons and biological agents. In the semiconductor industry, $O_2(a)$ and atomic oxygen are used for ashing photoresist films onto semiconductor wafers. Finally, the study of $O_2(a)$ may also lead to more efficient propulsion systems.

II. Background

Absorption from $O_2(a)$ to singlet sigma oxygen ($O_2(b)$) is very weak and the optical transitions are highly forbidden. This chapter will explore the underlying reasons why this molecule is difficult to detect and quantify. First, a short history will be presented of those who tried to characterize $O_2(a^1\Delta_g)$ both experimentally and theoretically. Then, various topics on the theory will be discussed. These topics are intended to aid the reader in comprehending the data contained in this thesis. Finally there is a short discussion on the use of the Hamiltonian to derive the theoretical line positions.

2.1 History of Detecting the $b^1\Sigma_g^+ \leftarrow a^1\Delta_g$ Transition of Oxygen

The history of detecting the $b^1\Sigma_g^+ \leftarrow a^1\Delta_g$ system of molecular oxygen is very brief. It began when Noxon [15] first observed the $b^1\Sigma_g^+ \rightarrow a^1\Delta_g$ emission spectra in a laboratory in 1961. Constrained with 1950s technology, Noxon merely saw a

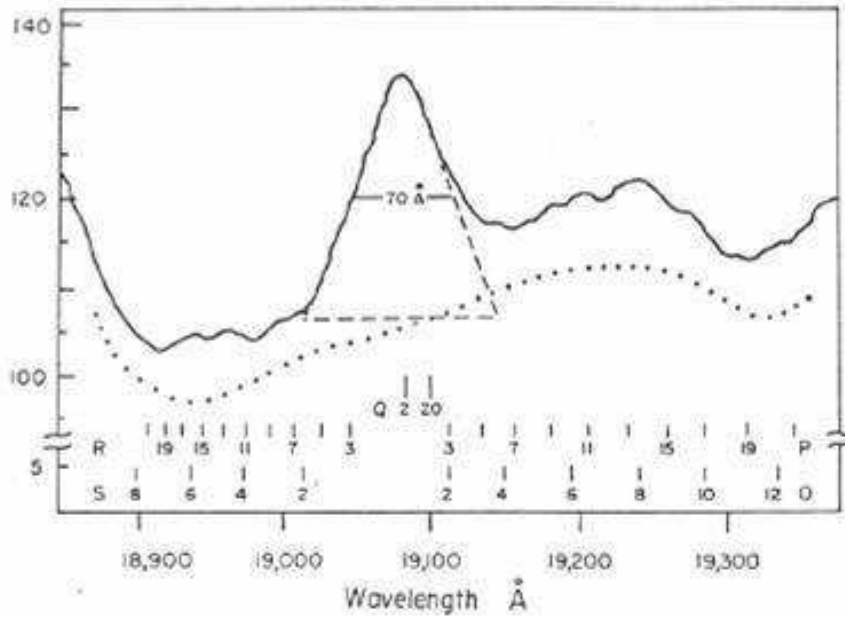


Figure 2.1: John Noxon's emission spectra of the transition from $O_2(b)$ to $O_2(a)$. [15]

convolution of the Q branch viewed as a single peak. None of the rotational levels were discernable, although he noted their theoretical positions on his spectra. With

the inability to achieve better resolution of these lines, the theoreticians then played a part to better understand these highly forbidden systems. In 1964, Ying-Nan Chiu [3] derived the theoretical line-strength formulas for both magnetic-dipole and electric-quadrupole radiation. Then, in 1986, 25 years after John Noxon's work, German and Canadian scientists [6] unearthed Noxon's and Chiu's work and calculated and detected twenty rotational levels in each of the five allowed branches of the emission of the $b^1\Sigma_g^+ \leftarrow a^1\Delta_g$ transition. Fink *et al* was the first to validate the relative signal

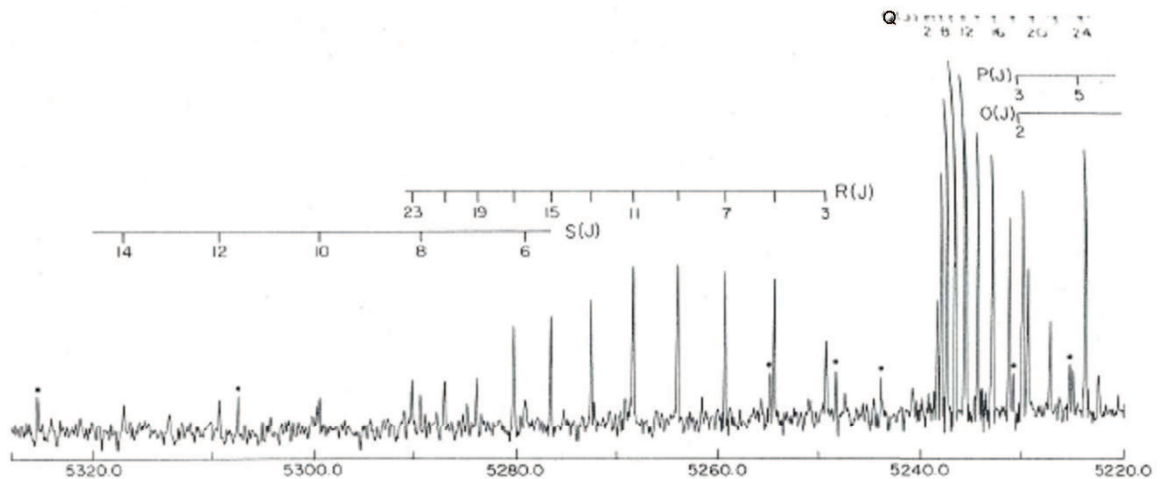


Figure 2.2: Group from Germany and Canada detected all five branches using a fourier transform spectrometer. They achieved a resolution of 0.2cm^{-1} and were the first to validate the relative signal strength intensities among the rotational lines. [6]

strength intensities among the rotational levels in each of the five branches.

Another 15 years go by before anyone else detects this transition. A group from Russia [18] in 2001 detected the absorption spectra of the Noxon system for the first time with a technique called intra-cavity laser spectroscopy. Finally in 2003, Williams *et al* further enhanced the off-axis ICOS method and quantitatively detected rotational levels in the Q branch of the $b^1\Sigma_g^+ \leftarrow a^1\Delta_g$ system for the (0,0) band [13] and the (1,0) band [24].

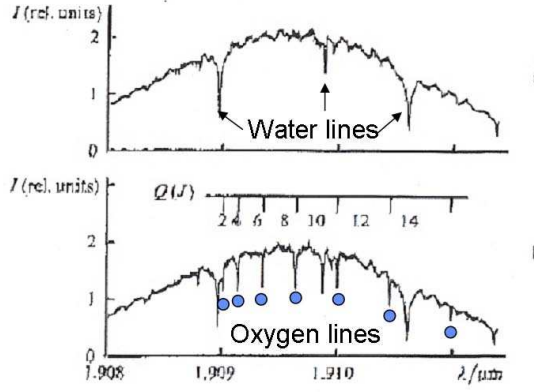


Figure 2.3: The Russians were the first to detect the absorption lines of the Noxon system. They used a technique called intra-cavity absorption spectroscopy and they achieved a resolution of 0.018cm^{-1} . [18]

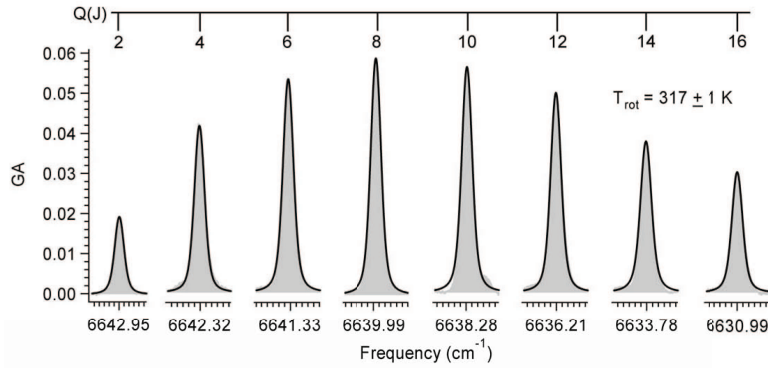


Figure 2.4: Williams *et al* was the first to detect the (1,0) band of the Q branch. Williams used O'Keefe's off-axis ICOS technique to finely resolve the rotational lines. [24]

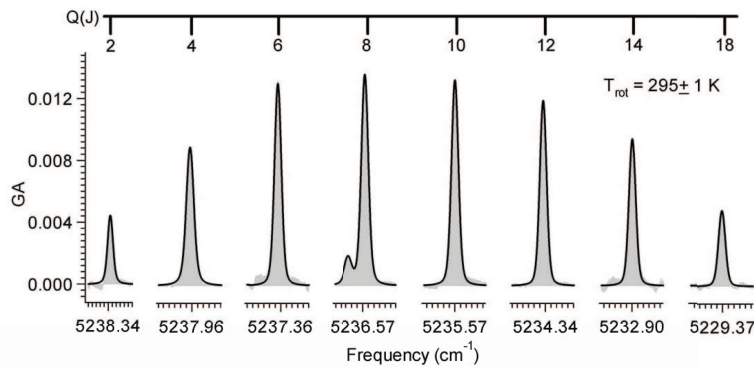


Figure 2.5: Williams *et al* used the off-axis ICOS technique to finely resolve the (0,0) band of the Q branch. [13]

2.2 History of Cavity Ringdown

In the early 90's the cavity ringdown technique emerged from the spectroscopic community [11]. This technique allowed the experimentalists to observe weaker transitions in the spectra and set the stage for the eventual detection and quantification of singlet oxygen concentrations. In 1992 Romanini and Lehmann [23] describe their successes in detecting weak overtones of HCN using a ringdown cavity (RDC) absorption scheme. Here they achieved ringdown times of 40 μs and effective path lengths of 24 km. This technique became the spring board for detecting very weak transitions.

By 1998, the RDC absorption scheme, now called cavity ringdown spectroscopy (CRDS) had become widely accepted by spectroscopists. In this year, an extensive survey on the theory and applications of CRDS was written by scientists from the UK [14]. Three years later, radiative lifetimes of $O_2(a^1\Delta_g)$ were measured using CRDS [7].

Although CRDS is not used in this experiment, the technique in this effort will use the method of obtaining the ringdown time from the optical cavity. This ringdown time will be a key factor in amplifying the weak signals associated with the $b^1\Sigma_g^+ \leftarrow a^1\Delta_g$ transition of oxygen.

2.3 History of Off-axis ICOS

In 1998, O'Keefe [16] explored a new variation of CRDS, called integrated-cavity-output-spectroscopy (ICOS). ICOS employs the same methodology from CRDS [i.e. highly reflective mirrors, ringdown time measurements (τ) and effective path length measurements, L], however, in ICOS instead of observing the single-pass output intensity (as is done in CRDS), all of the output intensities are collected and focused onto an InGaAs detector where the signals are then integrated to produce the absorption feature (See Figure 2.6). Also, since the effective path lengths are so large ($\approx 100km$), Beer's Law can then be represented as an infinite series. The limit

at which this series converges will produce a factor that amplifies the weak signal. This concept will be more rigorously explained in the succeeding chapters.

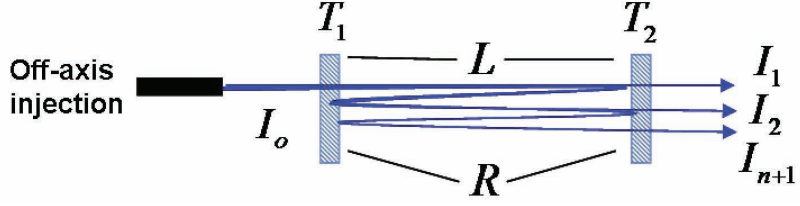


Figure 2.6: Here is a basic schematic of the off-axis ICOS technique . The cavity outputs are collected and integrated to acquire the absorption feature.

An Off-axis version of ICOS was then developed by O’Keefe in 2001. In the same year, Paul *et al* used diode lasers (instead of the typical dye laser) with the newly developed off-axis ICOS method to get an extremely narrow bandwidth [12]. A narrower bandwidth means more resolving power, which in turn allows for the searching of very weak absorption lines. Paul *et al* used the off-axis configuration because diode lasers are very sensitive to optical feedback. To rectify this, the diode laser is simply injected off the optical axis. Not only did the noise due to the optical feedback decrease significantly, but the effective path length increased by creating a Lissajous spot pattern on the mirrors. Measurements in the near infrared region using off-axis ICOS was then achievable [5]. This research group was also the first to define the following relation (2.1) which is paramount in ICOS theory today [12].

$$\frac{\Delta I}{I(\alpha L = 0)} = \frac{GA}{1 + GA} \quad (2.1)$$

Where $G = \left(\frac{2R^2}{1-R^2} \right)$ is the cavity enhancement factor, $A = 1 - e^{-\alpha L}$ is the single-pass absorption, $I(\alpha L = 0)$ is the laser intensity through the empty cavity, and $\Delta I = I(\alpha L = 0) - I(\alpha L)$ is the the change in the steady-state cavity output. This equation is further explained in Section 3.1.2, and Appendix A explores the full mathematical development of this equation from Beers Law.

2.4 Physical Theory

Singlet delta oxygen is a diatomic homonuclear molecule that couples its angular momenta according to Hund's case (b). This section will describe the $b^1\Sigma_g^+ \leftarrow a^1\Delta_g$ transition, how angular momenta are defined in molecules, and finally the symmetry properties and selection rules pertaining to the $b^1\Sigma_g^+ \leftarrow a^1\Delta_g$ transition.

2.4.1 The Transition. As mentioned earlier, the Noxon band is the electric-quadrupole transition between the first two excited electronic states of molecular oxygen (Figure 2.7). Specifically, this experiment will detect transitions between the first vibrational level ($v = 0$) of $O_2(a)$ and the second vibrational level ($v = 1$) of $O_2(b)$. This band is written in shorthand as the (1,0) band, where the numbers refer to the vibrational levels of the upper state and lower state respectively.

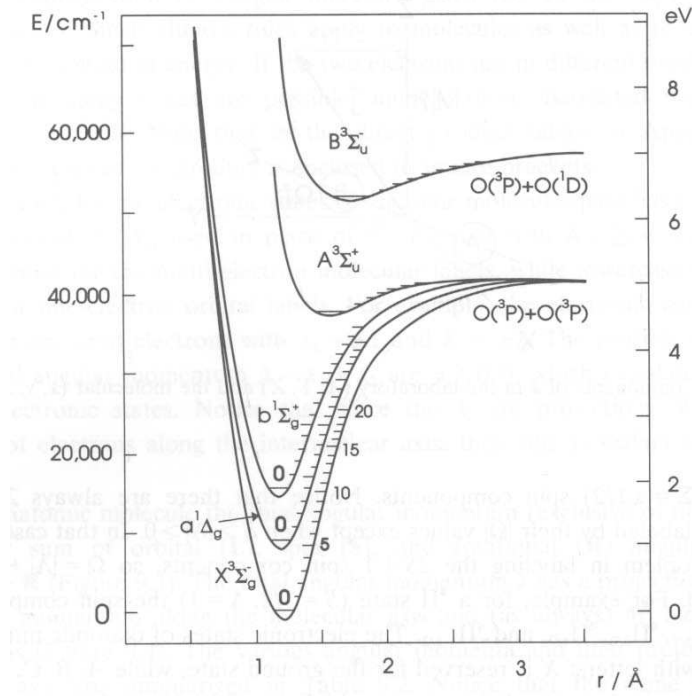


Figure 2.7: The first five electronic states of oxygen. [2]

A general statement to put this transition into perspective, is the fact that the electric-dipole moment is 10^7 times more likely to occur than the electric-quadrupole moment [8].

2.4.2 The Electric-Quadrupole Moment. When solving for the matrix elements of the time-dependent Schrodinger equation for this particular transition, one discovers that the first non-zero moment is the electric-quadrupole moment. That is to say, the electric-dipole and magnetic-dipole moments both vanish for this transition, making the Noxon system a pure electric-quadrupole allowed transition. Therefore, it will be worthwhile to discuss very briefly about the electrostatic field that results. This field is mathematically described by the third term in the multipole expansion of an arbitrary scalar potential, $\phi(r)$, shown below [28],

$$\phi(r) = \frac{1}{4\pi\epsilon_0 r} \sum_{i=1}^N q_i + \frac{1}{4\pi\epsilon_0 r^2} \sum_{i=1}^N q_i r_i \cos\theta_i + \frac{1}{4\pi\epsilon_0 r^3} \sum_{i=1}^N \frac{q_i r_i^2}{2} (3 \cos^2\theta_i - 1) + \dots \quad (2.2)$$

Where ϵ_0 is the permittivity of free space, r is the distance from the origin to the test charge, r_i is the distance from the origin to some internal charge within the molecule, q_i is the magnitude of that charge (since we are dealing with electrons $q_i = e_i$), and θ_i is the angle separating r and r_i . It is apparent from equation 2.2 that the electric-quadrupole field weakly interacts with any test charge compared to the first two terms because of it's $\frac{1}{r^3}$ dependence. After substituting the $\cos^2\theta_i$ term with direction cosines, the third summation in equation 2.2 becomes a tensor. The components of the quadrupole moment tensor can then be written as follows [28],

$$Q_{jk} = \sum_{i=1}^N q_i (3 j_i k_i - r_i^2 \delta_{jk}) \quad (2.3)$$

Where Q_{jk} is the component of the electric quadrupole moment tensor, both j_i and k_i spatial indices, and δ_{jk} is the Kronecker delta (recall $(j, k = x, y, z)$). It is this

tensor which is inserted into the three-dimensional wave equation as an operator, \hat{Q} , to generate the scalar electric-quadrupole moment which is then used to calculate the integrated absorption cross sections (σ_I) and the signal strength intensities ($S_{J'J''}$). The quadrupole term of equation 2.2 can be written in terms of the quadrupole moment tensor [28],

$$\phi(r)_Q = \frac{1}{4\pi\epsilon_0 r^3} \frac{1}{2} \sum_{j=x,y,z} \sum_{k=x,y,z} l_j l_k Q_{jk} \quad (2.4)$$

Where l_j and l_k are the direction cosines. Since the quadrupole tensor is a symmetric tensor¹ the number of independent quantities reduces from nine to six. By summing up the diagonal,

$$Q_{xx} + Q_{yy} + Q_{zz} = 0 \quad (2.5)$$

the tensor further reduces to five terms. The tensor can be further reduced because molecular oxygen has an axis of rotational symmetry. This symmetry diagonalizes the tensor because all of the off diagonal terms cancel each other out, $Q_{jk}^a = 0$ for $j \neq k$. Therefore, only three terms are left [28],

$$Q_{xx}^a + Q_{yy}^a + Q_{zz}^a = 0 \quad (2.6)$$

In fact, this symmetry states that for every charge at a given value x , there will be an equal charge at the same numerical value for y for the same value of r . This means that,

$$Q_{xx}^a = Q_{yy}^a \quad (2.7)$$

¹ $Q_{jk} = Q_{kj}$ for $j \neq k$

When this relation is inserted into equation 2.6, the result is [28]

$$Q_{xx}^a = Q_{yy}^a = -\frac{1}{2}Q_{zz}^a \quad (2.8)$$

Equation 2.8 shows that there is only one independent component of the quadrupole moment tensor. This component is typically written as Q^a and is defined as the term associated with the axis which coincides with the axis of symmetry. Therefore, if the internuclear axis of O_2 is defined as the z-axis, then $Q^a = Q_{zz}^a$.

With this definition of the quadrupole moment, the scalar potential that results from an electric-quadrupole moment can be written as [28],

$$\phi(r)_Q^a = \frac{Q^a}{4\pi\epsilon_0} \frac{(3\cos^2\theta - 1)}{4r^3} \quad (2.9)$$

Include some AP coupling references from Steinfeld example (pg21)

2.4.3 Angular Momentum in Molecules. In defining the angular momentum vectors, diatomic molecules must reference their internuclear axis. (Figure 2.9 graphically shows this concept.) The various Hund's cases (a-e) describe the ways in which the angular momentum vectors are coupled to the internuclear axis. Only case (a) and case (b) will be discussed here as they relate to this study.

2.4.3.1 Hund's Case (a). The theoretical line positions in this experiment were derived using a Hamiltonian from Hund's case (a) for the $b^1\Sigma_g^+ \leftarrow X^3\Sigma_g^-$ and the $a^1\Delta_g \leftarrow X^3\Sigma_g^-$ transitions. The Hamiltonian and spectroscopic constants were taken from a paper written by Cheah and Lee [27]. They were able to use the case (a) Hamiltonian because the transitions they were looking at both consisted of the triplet ground state of molecular oxygen².

Hund's case (a) states that the electronic motion of the molecule (which includes both the orbital and spin angular momentum) is strongly coupled to the internuclear

²The term triplet refers to the 3 degenerate spin states

axis, thereby strongly defining the $\mathbf{\Omega}$ vector, which is the total electronic orbital angular momentum about the internuclear axis. Recall that the total angular momentum in atomic systems is defined as³ $\mathbf{J}=\mathbf{L}+\mathbf{S}$, whereas for molecules in case (a) configurations it is written as $\mathbf{\Omega}=\mathbf{\Lambda}+\mathbf{\Sigma}$. Where $\mathbf{\Lambda}$ is the internuclear axis component of \mathbf{L} and $\mathbf{\Sigma}$ is the internuclear axis component of \mathbf{S} . Furthermore, the $\mathbf{\Omega}$ and \mathbf{R} (angular momentum of nuclear rotation) form the resultant \mathbf{J} for molecules in case (a). This can all be seen in Figure 2.8. Since this coupling configuration is very similar to the

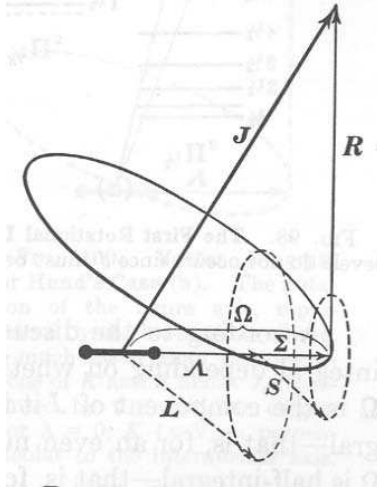


Figure 2.8: Vector diagram for a homonuclear diatomic [Hund's case(a)]. [25]

symmetric top, the resulting rotational energy levels for a molecule in Hund's case (a) will have the form of the symmetric top. If we consider a rigid rotor, this energy is [8],

$$F(J) = B_v J(J+1) + (C - B_v) \Lambda^2 \quad (2.10)$$

Where $F(J)$ is the rotational energy, B_v is the rotational constant, and $C\Lambda^2$ can be considered as the spin-orbit coupling term [25], but since $S=0$ for singlet states, $C=0$.

³Where \mathbf{L} is the electronic orbital angular momentum and \mathbf{S} is the electronic spin angular momentum.

Therefore we have

$$F(J) = B_v[J(J+1) - \Lambda^2] \quad (2.11)$$

However, a much better approximation is the non-rigid rotor model, so the equation then becomes,

$$F(J) = B_v[J(J+1) - \Lambda^2] - D_v[J(J+1) - \Lambda^2]^2 \quad (2.12)$$

Where D_v is the centrifugal distortion constant. Finally, when the vibrational term is inserted,

$$F(J) = \nu_0 + B_0[J(J+1) - \Lambda^2] - D_0[J(J+1) - \Lambda^2]^2 \quad (2.13)$$

This is the final form of the Hamiltonian used by Cheah and Lee [27]. They reasoned that although the two bands they looked at were actually in transition from case (b) to case (a), the case (a) Hamiltonian gave the better fit to their data. Therefore, in this experiment this same Hamiltonian was used to calculate the band energies for the $b^1\Sigma_g^+ \leftarrow a^1\Delta_g$ system. This was done by simply subtracting the two term energies found by the case(a) Hamiltonian. A MatLab[®] program was written for this experiment to generate a list of band energies for $b^1\Sigma_g^+ \leftarrow a^1\Delta_g$ (1,0). This program is presented in Appendix B.

2.4.3.2 Hund's case (b). The Hund's case (b) Hamiltonian more accurately predicts the theoretical energies for the $b^1\Sigma_g^+ \leftarrow a^1\Delta_g$ band, because both are singlet states. A singlet state has no spin component and consequently $\mathbf{\Omega}$ is no longer defined. Case (b) applies to all transitions where the electron spin angular momentum \mathbf{S} is either weakly coupled to the internuclear axis, or is not present at all (Refer to Figure 2.9). Therefore, the good quantum number is K , which is the total angular momentum without spin. The resulting equation for the total angular

momentum is $\mathbf{J} = \mathbf{K} + \mathbf{S}$. For the case of $O_2(a)$ and $O_2(b)$, $\mathbf{J} = \mathbf{K}$ since $\mathbf{S} = 0$. This fact is important when considering selection rules (See Figure 2.10).

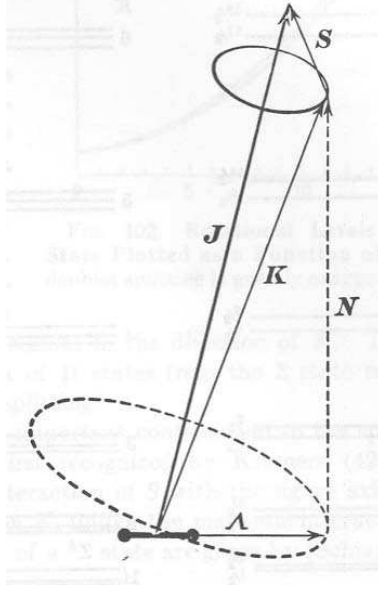


Figure 2.9: Vector diagram for a homonuclear diatomic [Hund's case(b)]. [25]

The case (b) Hamiltonian was not used in this study because the spectroscopic constants (such as B_v , D_v , $\omega_e\chi_e$ and $\omega_e y_e$) are not yet available for the $b^1\Sigma_g^+ \leftarrow a^1\Delta_g$ transition. However, Williams did utilize the case (b) Hamiltonian in previous work to determine the line strength intensities ($S_{J',J''}$) and the integrated absorption cross sections (σ). These calculated cross sections were used in this study.

Furthermore, the atomic notation $^{2S+1}\mathbf{L}$ is now written as $^{2S+1}\mathbf{\Lambda}$ for molecules. Therefore, singlet delta oxygen ($a^1\Delta_g$) refers to $\mathbf{S} = 0$ and $\mathbf{\Lambda} = 2$ and singlet sigma oxygen ($b^1\Sigma_g^+$) refers to $\mathbf{S} = 0$ and $\mathbf{\Lambda} = 0$.

2.4.4 Symmetry Operations and Properties. The $O_2(a)$ molecule is both diatomic and homonuclear, therefore it is classified as a $D_{\infty h}$ point group [2]. The $D_{\infty h}$ group is unique because in addition to the usual rotation $\hat{\sigma}$ and reflection \hat{C}_n operations for diatomic molecules, the inversion operator, \hat{i} , is also used. When the inversion operator is performed on a molecule, it's corresponding wavefunction is either changed or unchanged. Spectroscopists keep track of this symmetry property

by the use of the subscripts g (gerade or even) and u (ungerade or odd). In Dirac notation [2],

$$i|g\rangle = |g\rangle \quad (2.14)$$

$$i|u\rangle = -|u\rangle \quad (2.15)$$

Therefore, in the case of singlet delta oxygen ($a^1\Delta_g$) the subscript g refers to the fact that when the inversion operator is applied, it's original wavefunction remains unchanged.

2.4.5 The Herzberg Diagram and Selection Rules. Quantum mechanically, the allowed transitions result from the computation of the following equation.

$$Q_{ba} = \langle \Psi_b | \hat{Q} | \Psi_a \rangle \quad (2.16)$$

Where Q_{ba} is the scalar electric-quadrupole moment, Ψ_a and Ψ_b are the three-dimensional wavefunctions for the a and b states respectively, and \hat{Q} is the electric-quadrupole moment operator. Of course, the equation doesn't cause the selection rules, but more precisely is the mathematical model of what occurs physically in nature between these two electronic states. To avoid performing the mathematics every time one wanted the selection rules, Gerhard Herzberg developed a diagram which accounts for these allowed transitions (and the resulting selection rules) and symmetry properties of the rotational levels for a given transition [8]. The Herzberg diagram is a pictorial representation that neatly encapsulates all of the selection rules and displays the allowed transitions between rotational levels and consequently the resulting lines and branches that are detectable. As shown in Figure 2.10 five branches are allowed for the $b^1\Sigma_g^+ \leftarrow a^1\Delta_g$ system of O_2 . The O,P,Q,R and S branches correspond to $\Delta K = -2, -1, 0, 1, 2$ respectively⁴. This is the first selection rule for an electric-quadrupole transition. Another selection rule involves the electric-quadrupole allowed

⁴Recall that since $\mathbf{J} = \mathbf{K}$, then $\Delta\mathbf{J} = \Delta\mathbf{K} = -2, -1, 0, 1, 2$.

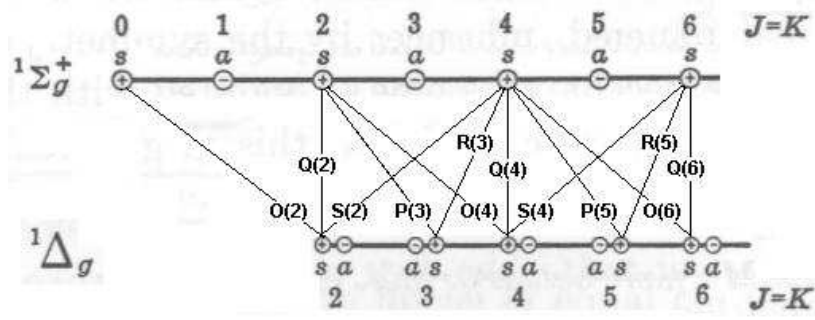


Figure 2.10: This is the Herzberg diagram for the $b^1\Sigma_g^+ \leftarrow a^1\Delta_g$ transition. This diagram is a handy tool for displaying the allowed rotational transitions which come about from the various selection rules for this particular transition. [8]

transitions between electronic states of O_2 . This selection rule is $\Delta\Lambda = 0, \pm 1, \pm 2$. For the $b^1\Sigma_g^+ \leftarrow a^1\Delta_g$ transition, the Σ symbol for $O_2(b)$ means $\Lambda = 0$ and the Δ symbol in $O_2(a)$ means $\Lambda = 2$, therefore, $\Delta\Lambda = 2$. The other selection rules for an electric quadrupole transition deal with the molecular symmetry labels. These selection rules are $g \leftrightarrow g$, $u \leftrightarrow u$, $+\leftrightarrow +$, and $-\leftrightarrow -$. The forbidden transitions are $g \leftrightarrow u$ and $+\leftrightarrow -$ [2] [8] [25].

Referring to Figure 2.10, it can be seen that there does not exist any transitions among the anti-symmetric states. The reason for this is due to the fact that the nuclear spin (\mathbf{I}) for an oxygen atom is zero. The zero quantity then classifies the oxygen atom, and consequently the molecule, as a boson. In quantum mechanics, the total wavefunction for a bosonic system must be symmetric according to Pauli's Exclusion Principle. Looking briefly at the total wavefunction (ψ_{Tot}), we have

$$\psi_{Tot} = \psi_{el} \frac{1}{r} \psi_{vib} \psi_{rot} \psi_{nuc} \quad (2.17)$$

Where ψ_{el} is the electronic wavefunction, and is symmetric for $b^1\Sigma_g^+ \leftarrow a^1\Delta_g$ due to the g subscripts for each state. ψ_{vib} is the vibrational wavefunction, yet this is solely dependent on the internuclear separation, r , so this is also symmetric. As mentioned earlier $\mathbf{I} = 0$ for oxygen, so the nuclear wavefunction (ψ_{nuc}) is symmetric. This leaves the rotational wavefunction, ψ_{rot} . However, since the exclusion principle dictates that

the total wavefunction must be symmetric, then ψ_{rot} must also be symmetric. This is why only symmetric transitions occur in the $b^1\Sigma_g^+ \leftarrow a^1\Delta_g$ transition.

The symmetry properties (i.e. the $+$ and $-$ associated with each electronic state) depend on the symmetry properties of the field in which the electrons move. First, consider the precession of the \mathbf{L} vector in Figure 2.9. If an angle φ is defined in one direction, say counterclockwise, then a $-\varphi$ will exist in the clockwise direction. Therefore, two electronic eigenfunctions will exist [8],

$$\psi_{el} = \chi e^{+i\Lambda\varphi_1} \quad (2.18)$$

$$\psi_{el} = \bar{\chi} e^{-i\Lambda\varphi_1} \quad (2.19)$$

Since the Schrödinger equation is linear, the linear combination of the above two eigenfunctions will also be a solution to the same eigenvalue. The total electronic eigenfunction can be combined two ways [8],

$$\psi_{el}^+ = a\chi e^{+i\Lambda\varphi_1} + b\bar{\chi} e^{-i\Lambda\varphi_1} \quad (2.20)$$

$$\psi_{el}^- = a\chi e^{+i\Lambda\varphi_1} - b\bar{\chi} e^{-i\Lambda\varphi_1} \quad (2.21)$$

Where a and b are arbitrary constants. Since Σ states are non-degenerate (because $\Lambda = 0$), ψ_{el} has only one solution and is no longer dependent on φ_1 . Therefore, the eigenfunction can either be ψ_{el}^+ or ψ_{el}^- . In fact all Σ states oscillate between having a ψ_{el}^+ and a ψ_{el}^- , however the labels ($+$ or $-$) on the Σ states describe which electronic eigenfunction state they begin as. For example, $b^1\Sigma_g^+$ will start out being symmetric and consequently all positive \mathbf{K} values will be symmetric. All odd \mathbf{K} values are then antisymmetric. This is why in molecular spectroscopy all Σ states are labeled with either $+$ or $-$. The state $a^1\Delta_g$ however, will contain both the symmetric and the antisymmetric component of ψ_{el} for every \mathbf{K} level. This is why Π states and higher have a two-fold degeneracy. All of this is shown in the Herzberg diagram in Figure 2.10.

It is important to note that the rotational levels of a diatomic molecule are classified according to the behavior of the total eigenfunction (not of the rotational eigenfunction alone) with respect to reflection at the origin. A rotational level is called positive or negative depending on whether the total eigenfunction remains unchanged or changes sign for such a reflection. This property is also called parity and corresponds to the evenness and oddness of atomic energy levels. [8]

2.5 *Spectral Lineshape Theory*

There are some basic concepts of spectroscopy that need to be mentioned for the purpose of defining commonly used phrases, such as the FWHM, the Lorentzian, the Gaussian, and the Voigt. These concepts and others are mentioned in the following sections.

2.5.1 Line Widths. Spectral lines are never completely monochromatic in absorption or emission spectra. If they were, they would appear as infinitely thin lines at their center frequency. However, there is always a spectral distribution $I(\nu)$ around the central frequency $\nu_0 = \frac{E_i - E_k}{h}$ corresponding to a molecular transition with an energy difference $\Delta E = E_i - E_k$ between the upper and the lower states. The function $I(\nu)$ in the vicinity of ν_0 is called the line profile, and the frequency interval $\Delta\nu = |\nu_2 - \nu_1|$ is called the Full Width at Half Maximum (FWHM) of the line [4]. There is another line width that is used called the Half Width at Half Maximum (HWHM). The HWHM is simply half the FWHM. Two other parts of the line profile are the line kernel and the line wings. The kernel is simply the region within the FWHM and the wings are the region outside the FWHM. This is graphically shown in Figure 2.11 [4].

If the isolated molecule or atom were to be ideally at rest, then natural lifetime broadening would be the dominate feature of the line profile. The shape of this feature is called the Lorentzian profile. Classical mechanics is used to describe this frequency distribution as a damped oscillator and ultimately describes the shape of

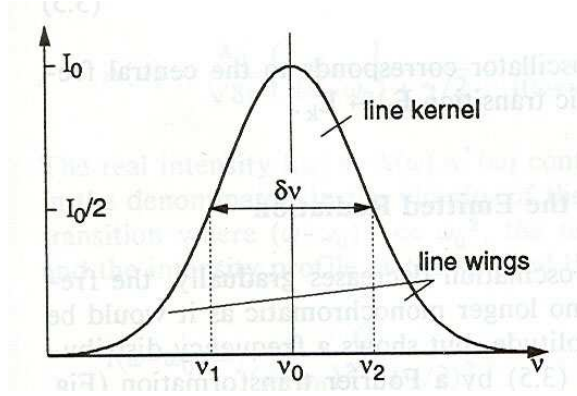


Figure 2.11: This is a general line profile. [4]

the Lorentzian profile⁵. The normalized Lorentzian line function is defined as [19],

$$L(\nu) = \frac{\frac{\Delta\nu}{2\pi}}{(\nu_0 - \nu)^2 + (\frac{\Delta\nu}{2})^2} \quad (2.22)$$

Where $\Delta\nu$ is the FWHM⁶. Pressure broadening also contributes to the Lorentzian lineshape of a given transition. more...

However, real molecules are never at rest. There will always be some thermal characteristic to the molecule. At thermal equilibrium, the molecules of a gas follow a Maxwellian velocity distribution. This distribution, which is fundamentally Gaussian, is the dominant profile for the lineshape. Since we are dealing with velocities, the resulting FWHM is often called the Doppler width. This width is the major contributor to the lineshape and consequently the Lorentzian lineshape is concealed by

⁵For a more complete explanation refer to Laser Spectroscopy by Demtröder. [4]

⁶Bernath [2] describes the FWHM as $\Delta\nu = 1/(2\pi\tau_{sp})$ where τ_{sp} is the spontaneous lifetime of the state. Bernath further shows that the FWHM agrees with the uncertainty principle $\Delta E \Delta t \geq \hbar$,

$$\frac{\Delta E}{\hbar} \tau_{sp} \sim \frac{1}{2\pi} \quad (2.23)$$

$$\Delta\nu \sim \frac{1}{2\pi\tau_{sp}} \quad (2.24)$$

it. Equation 2.25 is the form of the Gaussian line function [2].

$$G(\nu) = \frac{1}{\nu_0} \sqrt{\frac{m c^2}{2 \pi k T}} e^{-\frac{m c^2 (\nu - \nu_0)^2}{2 k T \nu_0^2}} \quad (2.25)$$

Where m is the mass of the molecule, c is the speed of light in a vacuum, k is Boltzmann's constant, T is temperature in kelvin, and the Doppler FWHM is defined as, [2].

$$\Delta \nu_D = 2 \nu_0 \sqrt{\frac{2 k T \ln(2)}{m c^2}} \quad (2.26)$$

One can clearly see the thermal properties of the molecule contained within equations 2.25 and 2.26.

The true shape of the spectral line is neither Lorentzian nor Gaussian, but a convolution of the two, called a Voigt lineshape. Equation 2.27 shows the result of the mathematics behind convoluting equations 2.22 and 2.25 together [19].

$$V(\nu) = \alpha_0 \frac{\ln 2}{\pi^{3/2}} \frac{\Delta \nu_L}{(\Delta \nu_D)^2} \int_{-\infty}^{\infty} \frac{e^{-t^2} dt}{\left(\frac{\Delta \nu_L}{\Delta \nu_D} \right)^2 \ln 2 + \left(\frac{\nu - \nu_0}{\Delta \nu_D} \ln 2 - t \right)^2} \quad (2.27)$$

Where α_0 is the area under the Voigt profile, $\Delta \nu_L$ is the HWHM of the Lorentzian and $\Delta \nu_D$ is the Doppler HWHM. This pressure broadening is a direct consequence of collisions which occur due to the molecules' individual velocities. In other words, the gas is pressure broadening itself. Figure 2.12 compares the Voigt lineshape to both the Gaussian and the Lorentzian lineshapes.

The Voigt profile plays a crucial role in the analysis of this experiment. The raw data which is fit against a Voigt lineshape is used to determine the area of the line. This fit area is necessary in calculating the peak cross section. Also, accurate measurements of the Voigt line wings enables the Lorentzian FWHM and the Gaussian FWHM to be extracted. Although extracting the Lorentzian and Gaussian lineshapes is done throughout the entire experiment, this technique is especially important in

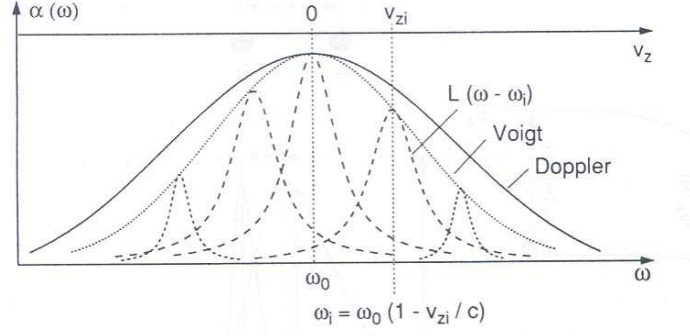


Figure 2.12: The Voigt profile. [4]

determining the pressure broadening coefficients. In this part of the experiment the Lorentzian FWHM's of a line are plotted against the pressure they were scanned at. The slope from this linear relationship is precisely the pressure broadening coefficient of that particular line. It is interesting to note that at low pressures ($\Delta\nu_D \gg \Delta\nu_p$) the Voigt reduces to the Gaussian lineshape, and at high pressures ($\Delta\nu_D \ll \Delta\nu_p$) the Voigt reduces to the Lorentzian lineshape.

2.5.2 Absorption Parameters. The absorption coefficient relates the change in flux (dF) of a stream of photons as they propagate through some distance (dx) containing an absorbing species to their original flux ($F = \frac{I}{h\nu}$), where h is Planck's constant [2] [9]. This defines the absorption coefficient as,

$$\frac{1}{F} \frac{dF}{dx} = -\alpha \quad (2.28)$$

The rate equation for a two level system must be considered in order to understand how the absorption coefficient (α) relates to the integrated absorption cross section (σ_I). Since this experiment deals only with the absorption band,

$$\frac{dN_b}{dt} = B_{b \leftarrow a} \rho N_a \quad (2.29)$$

Where $B_{b \leftarrow a}$ is the Einstein coefficient for absorption, ρ is the radiation density ($\rho = \frac{h\nu F}{c}$), and both N_a and N_b are the number densities of $O_2(a)$ and $O_2(b)$ respectively.

Substituting the definition for the Einstein B coefficient (namely $B_{b \leftarrow a} = \frac{2\pi^2}{3\epsilon_0 h^2} Q_{ba}^2 g(\nu - \nu_{ba})$) and rearranging terms, it can be shown that equation 2.29 becomes,

$$\frac{dN_b}{dt} = \frac{2\pi^2 Q_{ba}^2 \nu}{3\epsilon_0 h c} g(\nu - \nu_{ba}) N_a F \quad (2.30)$$

Where Q_{ba} is the electric-quadrupole moment that governs the transition between $O_2(a)$ and $O_2(b)$ ⁷. The symbol ν is the frequency of the observed transition and $g(\nu - \nu_{ba})$ is the line shape function⁸. The integrated absorption cross section can now be defined from equation 2.30 as,

$$\sigma_I(\nu) = \frac{2\pi^2 Q_{ba}^2}{3\epsilon_0 h c} \nu g(\nu - \nu_{ba}) \quad (2.31)$$

This is the "effective area" that the molecule presents to that stream of photons of flux F [2].

The rate at which $O_2(a)$ populates $O_2(b)$ (*i.e.* $\frac{dN_b}{dt}$) is proportional to the change in flux of the photons by $O_2(a)$ over some distance, and can be expressed as,

$$\frac{dF}{dx} = -\frac{dN_b}{dt} \quad (2.32)$$

Combining equations 2.30, 2.31 and 2.32, it can be shown that,

$$\frac{dF}{dx} = -\sigma_I N_b F \quad (2.33)$$

Finally, the absorption coefficient can be shown to be a function of the integrated absorption cross section by inserting equation 2.33 into equation 2.28,

$$\alpha = \sigma_I N_b \quad (2.34)$$

⁷This is the scalar quantity that results from equation 2.16.

⁸Which is typically normalized with the following relation, $\int_{-\infty}^{\infty} g(\nu) d\nu = 1$.

This suggests that the absorption coefficient of an absorbing species (in this case $O_2(a)$) is directly proportional to the effective absorbing area of that absorbing species multiplied by the number density of the excited state it is populating (in this case $O_2(b)$).

There is another absorption cross section (σ) that is frequently reported in papers, and this is the cross section which is dependent on the temperature and pressure of the optical cavity. The units for this cross section is cm^2 . This value is specific to a certain frequency. So, when the phrase peak cross section is used, this is referring to the cross section at line center, ν_0 . This cross section is often confused with the intrinsic value, called the integrated absorption cross section (defined in this study as σ_I). This value is not dependent on the temperature nor the pressure and is reported in units of $\frac{cm^2}{cm^{-1}}$.

2.5.3 Pressure Broadening. Pressure broadening refers to the widening of the spectral line due to an increase in pressure. This rise in pressure increases the probability of collisions among the molecules within a gaseous mixture. This is why pressure broadening is often referred to as collisional broadening. To conserve energy and momentum, the spectral line's absorbency (as well as its peak cross section) decreases as it broadens. This shortening and widening of the spectral line is clearly shown in the results presented in Chapter IV.

In previous work [21] [22] [19], there is a clear dependence on the rotational quantum number for the magnetic-dipole allowed transition of the $b^1\Sigma_g^+ \leftarrow X^3\Sigma_g^-$ system of oxygen. Work by Steinfeld *et al* [10] reflects the views of many experimental spectroscopists that rotationally-inelastic collisions are the dominant mechanism in molecular pressure broadening. Therefore, this study will plot this trend for the first time for the Noxon system.

III. Experimental Approach

After grasping a firm understanding of the theories presented in Chapter II, it is now necessary to explain the experimental approach to fully appreciate the data obtained. Therefore, this chapter will be divided into three main sections. The first section deals with the technique used in this experiment. The second section describes the apparatus, while the third section explains the overall procedure, from optimizing the apparatus to analyzing the data.

3.1 *Multi-Pass Absorption Spectroscopy*

The spectroscopic method used in this experiment is aptly named multi-pass absorption spectroscopy. However, the name is really a general phrase for the methods employed in this experiment. It is called multi-pass because the cavity has the ability to bounce light on the order of 80,000 times. This allows a gain of the absorbance feature to occur within the cavity. The word absorption refers to the fact that this technique deals with the observation of absorption lines in the spectrum as opposed to transmission lines. More specifically, however, multi-pass absorption spectroscopy incorporates cavity ringdown measurements and the off-axis integrated-cavity-output-spectroscopy (ICOS) technique. These methods will be individually discussed below.

3.1.1 The Cavity RingDown. The only element of cavity ringdown spectroscopy (CRDS) used in this experiment will be the calculation of the ringdown time. The ringdown time, τ , is used to verify how well the laser light is "trapped" in the optical cavity. In order to acquire the best performance out of the mirrors in the cavity, they must be devoid of any additional lossy materials such as water and dust particulates. The ringdown time will therefore give a measure of these losses. The value of the ringdown time is also used in calculating the intensity of the observed absorption line. This will be further explained later in this chapter.

In CRDS, the lifetime of a photon (This is simply the rate at which it takes light to enter and exit the cavity, commonly referred to as the ringdown time) in an

optical cavity is used to obtain the total internal cavity losses (per pass) as a function of the photon frequency [16]. When these losses are dominated by the scatter and transmission of the two mirrors (i.e. a very clean cavity), then the mirror reflectivity can be obtained. When a narrow band absorbing species is present (i.e. $O_2(a)$), absolute molecular absorption intensities can be inferred by subtracting the baseline losses of the cavity¹ [16]. The subtracting of this baseline will be further explained in the Section 3.3.

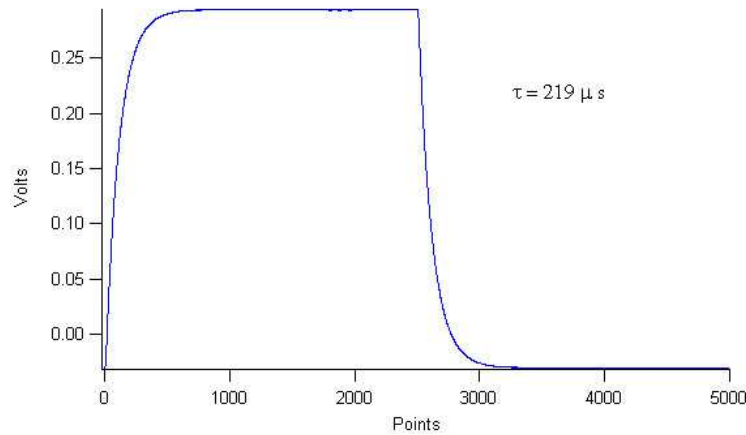


Figure 3.1: The $1/e$ point on the downward curve of this square wave is where the ringdown time is measured. Although the x-axis is currently in point-space, this axis can be better thought of as a time axis for this example.

The ringdown time is acquired in this experiment by first modulating the laser signal with a square wave. This modulation will simulate a pulsed laser which is necessary in measuring the ringdown time (As shown in Figure 3.9). At the end of one pulse, the output waveform has a rampdown exponential curve which corresponds to the time decay of the photon population leaving the cavity. The ringdown time is obtained by exponentially fitting this time decay curve. Typical ringdown times are on the order of ca. $50\mu s$, however, this experiment has acquired ringdowns as high as $220\mu s$. Optimizing this ringdown time is crucial when detecting weak signals, such as those generated by an electric-quadrupole transition. To understand the physical

¹This statement refers to the relation $\frac{I(\alpha L=0)}{I(\alpha L)} - 1$. See a further explanation in Appendix A.

nature and usefulness of the ringdown time, it is necessary to develop some simple equations which will relate τ to other physical quantities of the cavity.

Consider when the reflectivity, R , raised to the number of trips in the cavity, N , is equal to the $1/e$ point of the output intensity²

$$R^N = \frac{1}{e} \quad (3.1)$$

Solve for N ,

$$N = -\frac{1}{\ln R} \quad (3.2)$$

In the limit of high reflectivity, the following series expansion is used,

$$\ln(x) \approx (x - 1) - \frac{1}{2}(x - 1)^2 + \frac{1}{3}(x - 1)^3 - \dots \quad (3.3)$$

Letting $R = x$. Therefore, the first order approximation to equation (3.3) becomes

$$\ln R \approx R - 1 \quad (3.4)$$

Substituting equation (3.4) into equation (3.2) yields the following relation for N ,

$$N = \frac{1}{1 - R} \quad (3.5)$$

Now a relation is needed for the ringdown time, τ , which describes how long it takes light to travel through the cavity N times, at a total distance L (the length of the

²The ringdown time also physically refers to the time it takes the output intensity, I , to equal the incident laser intensity divided by e [14]. Therefore the ringdown time is acquired when $I = \frac{I_0}{e}$. This relation can then be used in the Beer-Lambert formula for two trips (equation (A.3)) inside the cavity, $I = I_0 R^2 e^{-3\alpha L}$. Transmittancy has no part in these equations because we are only concerned about the time inside the cavity. So, $\frac{I_0}{e} = I_0 R^2 e^{-3\alpha L}$. Now, I_0 cancels out, $\alpha = 0$ since a ringdown is the time it takes light to travel through an empty cavity. The equation then becomes, $\frac{1}{e} = R^2$. If we then consider the light to travel through the cavity N times, we have the final form $\frac{1}{e} = R^N$.

cavity). Assuming a vacuum state, τ is expressed as,

$$\tau = \frac{N L}{c} \quad (3.6)$$

where c is the speed of light in a vacuum. Solving for N ,

$$N = \frac{\tau c}{L} \quad (3.7)$$

Finally, set equations (3.5) and (3.7) equal and solve for τ ,

$$\tau = \frac{L}{c(1 - R)} \quad (3.8)$$

Equation (3.8) explicitly shows the importance of high reflectivity. As $R \rightarrow 1$, $\tau \rightarrow \infty$. This equation will help the experimenter determine if the laser, mirrors, detector, etc. are all operating properly, since maximum τ is desired. Additionally, this equation will allow the conversion efficiency, or yield of $O_2(a)$ generated by the plasma to be determined for a given data set. This quantity is also very important when optimizing the apparatus for maximum $O_2(a)$ detection.

Most spectroscopists, when performing CRDS experiments, use a high-powered pulsed IR laser. A pulsed laser is the obvious choice due to the fact that measuring a decay rate of the photon population is at the heart of CRDS. This is necessary, since the detector needs to "see" a quanta of light to perform the required decay rate calculation mentioned above. However, pulsed IR sources usually do not have the high frequency resolution (narrow-band) necessary for many IR applications, such as detecting $O_2(a)$. Therefore, tunable diode lasers are needed to provide the required narrow-band resolution. However, diode lasers cannot simply be used in place of the pulsed laser in a CRDS set-up. One reason is the fact that CRDS set-ups require laser light to be injected into the cavity on the optical axis. Although this provides a stable cavity configuration, the noise level associated with the optical feedback to the diode laser due to the on-axis configuration is drastic and counter-productive. Therefore,

an off-axis design is required. Specifically, the design developed by O’Keefe [16] will be utilized in this experiment. This design is capable of tuning over many modes.

3.1.2 Off-Axis ICOS. The theory of off-axis paths in optical cavities have been around since the 1960’s. The reflections of light rays in such configurations are spatially separated until the ”re-entrant” condition is fulfilled [12]. The ”re-entrant” condition refers to when the light ray begins to retrace it’s path within the cavity. This spatial separation greatly reduces the optical feedback for the tunable laser diode. Depending on the design of the cavity, the re-entrant condition can be met from a few passes to an infinite number of passes. In order to achieve cavity enhancement of the absorption feature, our experiment requires a large number of passes before the re-entrant condition is met. This is accomplished with the use of parabolic mirrors and made use of their natural astigmatism. Specifically the mirrors are designed after the parabolic mirrors in the Herriott cell. When astigmatic mirrors are used the laser light creates a Lissajous spot pattern on the mirrors and throughout the cavity. This pattern alleviates the central spot pattern along the optical axis which creates the unwanted optical feedback to the tunable laser diode. Because of this, off-axis ICOS is truly the only method currently developed to utilize the diode lasers with the required resolution to detect $O_2(a)$.

Once the re-entrant condition is met with the desired amount of passes, the next factor to be concerned about is the ratio between the cavity free spectral range (FSR) and the bandwidth of the absorbing feature. In order to scan linearly through the cavity with the laser frequency, the FSR of the cavity must be narrower than the absorption feature. (Due to the incredibly long path length of our design, the modes within the cavity basically overlap and we have effectively a continuous mode. This allows for the laser to scan linearly very effectively. This linear relationship is crucial in the analysis of the data, since a polynomial is fit to the baseline and is subtracted from the absorption feature. The more the baseline resembles a line, the more accurate the analysis.

Starting from Beers Law and incorporating the above concepts we arrive at the following equation which is the heart of off-axis ICOS theory,

$$\frac{\Delta I}{I(\alpha L = 0)} = \frac{GA}{1 + GA} \quad (3.9)$$

Where $G = \frac{R}{1-R}$ is the cavity enhancement factor, $A = 1 - e^{-\alpha L}$ is the single-pass absorption, and $\Delta I = I(\alpha L = 0) - I(\alpha L)$ is the change in the cavity output. Essentially, this equation says that the absorption information (A) is contained within that change in the cavity output [16]. This allows for a direct measurement of the absorption feature. A more detailed explanation of each mathematical step is presented in Appendix A.

3.2 The Apparatus

The apparatus used in this experiment is designed for the off-axis integrated-cavity-output-spectroscopy (ICOS) technique, and utilizes the method of cavity ring-down to determine the decay time, (τ), of the light within the cavity. The reason why this particular device is unique is because of it's ability to "trap" light to such a high degree. In Section 2.1 it was explained that off-axis ICOS was developed by Anthony O'Keefe in 2001. However, O'Keefe was only able to achieve approximately 400 passes in his cavity, whereas this device allows for greater than 80,000 passes.

Since the resolving power of the apparatus depends on the number of passes the photons will complete in the cavity, it becomes critical to have highly reflective mirrors. The mirrors used in this experiment are coated to highly reflect the near IR (1400–1600 nm) and have a radius of curvature of ca. 1m. Reflectivities of more than 99.9987% were achieved and confirmed with the ringdown time³. As mentioned above, the shape of the mirrors were modeled after the Herriott cell (parabolic mirrors) which is designed to "trap" light. Therefore, the heart of this experiment lies within the two

³Use equation (3.8) and solve for R. In this experiment the highest ringdown time achieved was 220 μ s. This corresponds to $R = 99.9988\%$

mirrors placed in the cavity. Keeping the mirrors devoid of any particulates, especially water, becomes an ongoing concern whenever a series of data is taken. After cleaning the mirrors, they stayed clean for about 10 days.

To generate the needed $O_2(a)$ species of oxygen, a mixture of ultra high purity helium (99.999%) and research grade oxygen is used. This mixture is then sent to a quartz tube via mass flow meters which control both the flow rates and the ratio between the two gases. A McCarroll cavity is placed over a region of the quartz tube so that a microwave discharge can be applied across the mixture. A Tesla Coil is used to apply the required initial ionization to ignite the gas to create the plasma. The plasma will then sustain itself and no further voltage is required. The McCarroll cavity is cooled with pressurized air to prevent over-heating. This plasma will generate the singlet delta oxygen needed for the experiment. The $O_2(a)$ then travels through the main cavity of the apparatus and is evacuated using a vacuum pump. A schematic diagram of the experiment setup is shown below in Figure 3.2. The main cavity contains the highly reflective parabolic mirrors at either end to

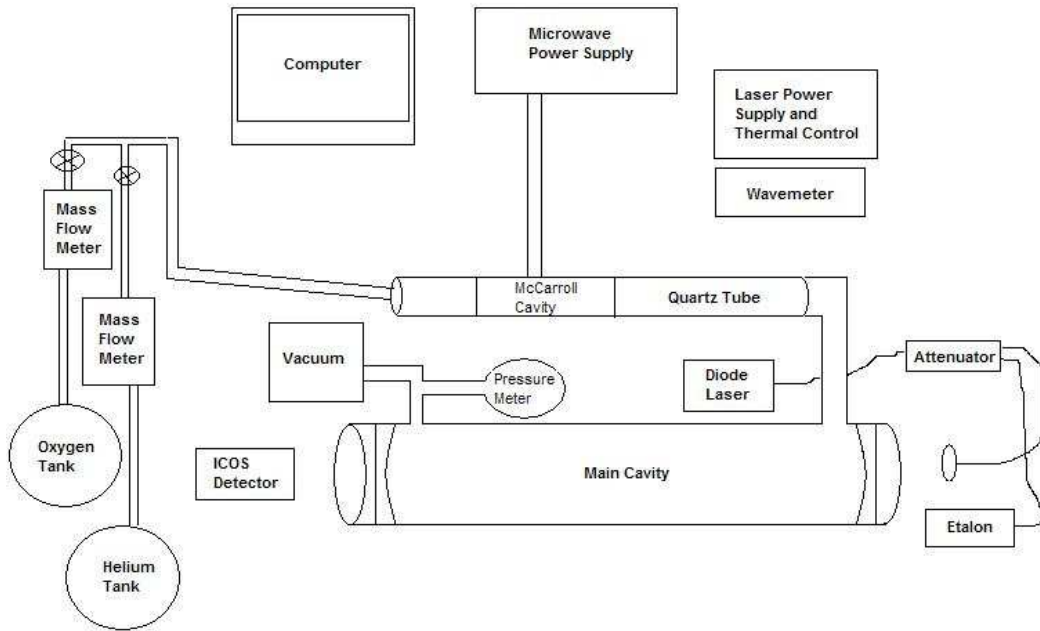


Figure 3.2: This is the experiment setup. The length of the optical cavity is 82 cm, the microwave power supply operated at 80 W, and the average pressure in the cavity was ca. 23 torr.

increase the path length of the transmitted laser light. A tunable laser diode, which is coupled to a fiber, is first connected to a light attenuator, which splits the light into two separate fibers. This first fiber has a 1:0.99 light intensity ratio, and is mounted near the entrance of the cavity. The light beam enters the cavity through the back of one of the mirrors. The light then exits the cavity by means of the extremely low transmittancy of the back mirror, passes through a lens which focuses the photons onto the InGaAs detector which then sends the data to a computer where it is stored as 1's and 0's in a text file. The second fiber on the attenuator has a 10:1 light intensity ratio. This decrease in intensity is needed for the wavemeter which is used to determine the absolute location of the spectral lines. The wavemeter specified a safe range of light intensities from 0 to 20 dBm. After going through the attenuator, the laser beam decreased from 90 dBm to about 10 dBm.

3.2.1 The Diode Lasers. Five distributed feedback (DFB) laser diodes were utilized in this experiment. Tunable DFB laser diodes were preferred for their resolution with the added convenience of being able to change their scanning wavelength peak by controlling the amount of current being sent to it. Broad tuning is achieved by adjusting the temperature of the diode, and fine tuning is achieved by adjusting the current supplied to the diode. These lasers were designed to scan at and around the following wavelengths: 1494.48 nm, 1499.71 nm, 1505.74 nm, 1512.575 nm, and 1515.63 nm. Diode lasers are excellent for this type of work since their scanning wavelengths are controlled via a thermal coupler. This experiment will operate in a safe temperature range of 10°C to 49°C. With this operating range, the lasers can only search over a wavelength range of 4 nm. Furthermore, each laser has a linewidth of 0.0001 cm^{-1} . This aids in the resolution required to observe ultra-weak transitions which had linewidths of ca. 0.008 cm^{-1} .

An etalon measurement of the diode laser was made during each scan of a line. This is necessary in forming a baseline during the analysis, since the etalon allows for the conversion of each data point into frequency-space.

3.3 Procedure

As with any experiment, the procedure for this experiment began with calibration and cleaning. In the first section below, a brief description is given as to how the tunable laser diodes were calibrated. This calibration was crucial in determining the exact locations of the absolute line positions. The next step in the procedure was to optimize various elements of the equipment to produce the best results. For this experiment, the best results correspond to high signal strength (i.e. maximize the ringdown time) and low noise. Therefore, a brief history is laid out which describes the optimization process for this experiment. Next, a section is provided below that briefly discusses how the data was taken. Finally, the last section provides a short description of how the data was analyzed. This is necessary, because the results presented in both Chapter IV and Appendix C are actually the end result of a series of steps performed by a computer program called IGOR Pro[®]. IGOR Pro[®] is a powerful data analysis program.

3.3.1 Calibration of Lasers. The purpose of calibrating the DFB laser diode is to extract the required temperature setting which corresponds to a line in the $O_2(a)$ spectra. Since these laser diodes only scan through 0.33 cm^{-1} , only one line can be seen at a time. This narrow scanning window is another reason why calibrating the lasers is so important.

This experiment utilized a wavemeter to calibrate the lasers. As mentioned above, a safe operating range of 10°C to 49°C was used in this experiment. Anything below 10°C risked condensation forming on the diode and anything above 49°C risked the chance of thermally damaging the electronics within the diode. Starting at 10°C , the laser was fed into the wavemeter which read the peak wavelength of the laser in wavenumbers (cm^{-1}). The laser temperature was then increased in steps of 3°C until 25°C , and then in steps of 2°C until 49°C . At each step, the peak wavelength was recorded. A graph was then generated for each laser which showed its temperature as a function of frequency (in cm^{-1}). See Figure 3.3 for an example of one such graph. As

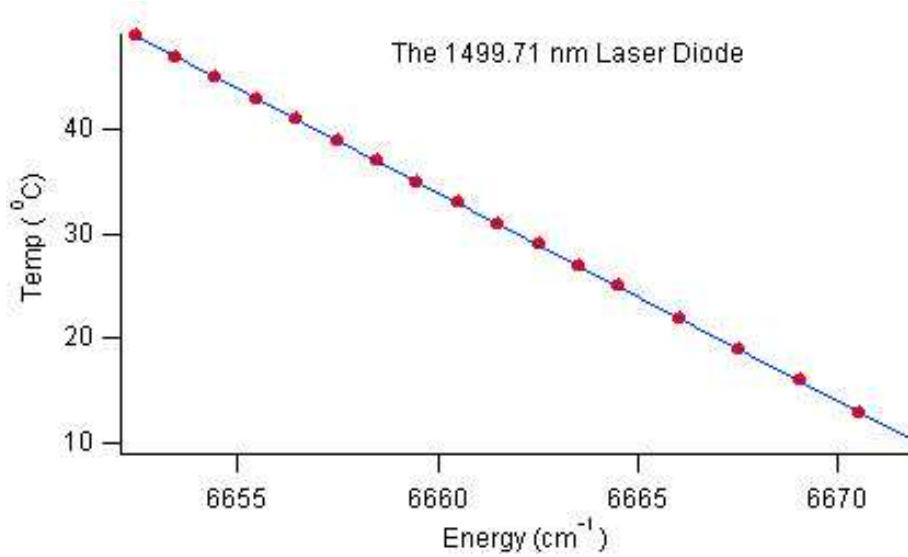


Figure 3.3: Temperature dependence for the 1499.71 nm laser

Table 3.1: Lines that are within the safe temperature range for the 1499.71 nm tunable laser diode.

Line	Energy (cm^{-1})	Laser Temperature ($^{\circ}C$)
S2	6662.169255	29.5888
R3	6653.662739	46.5181
R5	6658.343271	37.2031
R7	6662.661218	28.6097
R9	6666.615169	20.7407
R11	6670.203603	13.5992

expected, there is a clear linear relationship between the temperature of the diode and the peak (or center) wavelength it will scan around. A linear regression is performed on the data in order to extract the slope and y-intercept. These parameters were then used to calculate the temperature the laser needed to be at for a given spectral line's energy. For example, for the laser shown in Figure 3.3, Table 3.2 lists the lines that can be observed with their corresponding laser temperatures. Tables such as these were generated for each of the five laser diodes.

3.3.2 Optimization.

Table 3.2: List of the slopes and y-intercepts obtained for the five lasers.

Laser (nm)	Slope ($^{\circ}\text{C}/\text{cm}^{-1}$)	Y-intercept ($^{\circ}\text{C}$)
1494.71	-2.0905 ± 0.0046	14008 ± 31.0
1499.71	-1.9902 ± 0.0003	13288 ± 1.89
1505.74	-2.0956 ± 0.0053	13942 ± 35.5
1512.575	-2.1323 ± 0.0037	14114 ± 24.2
1515.63	-2.1345 ± 0.0038	14109 ± 24.9

3.3.2.1 Flow Rate Dependence. One of the most important elements is understanding the relationship between the concentration of $O_2(a)$ and the flow rate ratio of oxygen and helium. In order to accomplish this we first set the laser to the strongest line in the Noxon Band, Q(8). Fixing the helium flow at 4000 sccm⁴, the oxygen was first brought in at 40 sccm, then 100 sccm, 200 sccm, 400 sccm, and finally 500 sccm. At each increment of oxygen the Q(8) line was recorded and then analyzed using IGOR Pro[®]. From the analysis, the number density (N_a) of $O_2(a)$ ⁵, the yield

⁴sccm stands for Standard Cubic Centimeter per Minute. Where "Standard" refers to Standard Temperature (273 K) and Pressure (1 atm) or STP.

⁵The number density is found by the following method. Since the single-pass absorption is defined as $A_\lambda = 1 - e^{-\sigma_\lambda N_\lambda L}$ (where σ_λ is the cross section of a certain wavelength, of $O_2(a)$, N_λ is the number density of a certain wavelength of $O_2(a)$, and L is the length of the cavity), then we can say $\sigma_\lambda N_\lambda L = \ln(1 - A_\lambda)$. From our analysis we measure both G (from the ringdown time) and GA (which is the peak signal strength). Therefore, we are able to calculate A_λ from the relation $\frac{GA}{G}$. Now we can write $\sigma_\lambda N_\lambda L = \ln(1 - \frac{GA}{G})$. Next we need two relations for the number density of $O_2(a)$, namely $[O_2(a)] = N_T f_b$ (where f_b is the boltzmann factor for a certain wavelength and N_T is the total number density of $O_2(a)$), and $A_\lambda = [O_2(a)] L \sigma_\lambda$. Setting each equal to $[O_2(a)]$ and then each other, we generate a formula for the total number density of $O_2(a)$,

$$N_T = \frac{A_\lambda}{\sigma_\lambda f_b L} \quad (3.10)$$

If we series expand the exponent in $A_\lambda = 1 - e^{-\sigma_\lambda N_\lambda L}$, we find that the first order approximation will be $A_\lambda = \sigma_\lambda N_\lambda L$. This means that $A_\lambda \approx \ln(1 - \frac{GA}{G})$. Inputting this result for A_λ into equation 3.10, the total number density of $O_2(a)$ can finally be written as,

$$N_T = \frac{\ln(1 - \frac{GA}{G})}{\sigma_\lambda f_b L} \quad (3.11)$$

of $O_2(a)$ ⁶, and the relative intensity (GA) were all able to be extracted. Figures 3.4 and 3.5 illustrate the relation among these quantities. Referring to Figure 3.4, we see

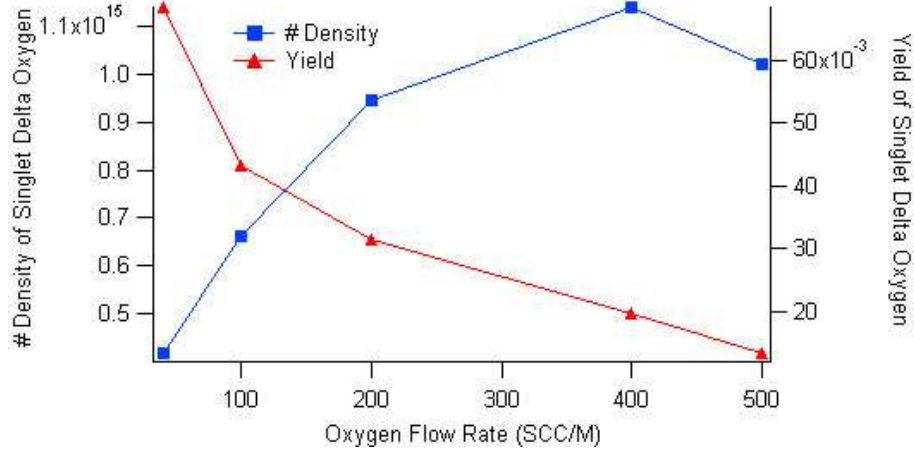


Figure 3.4: Flow rate dependence for singlet delta oxygen

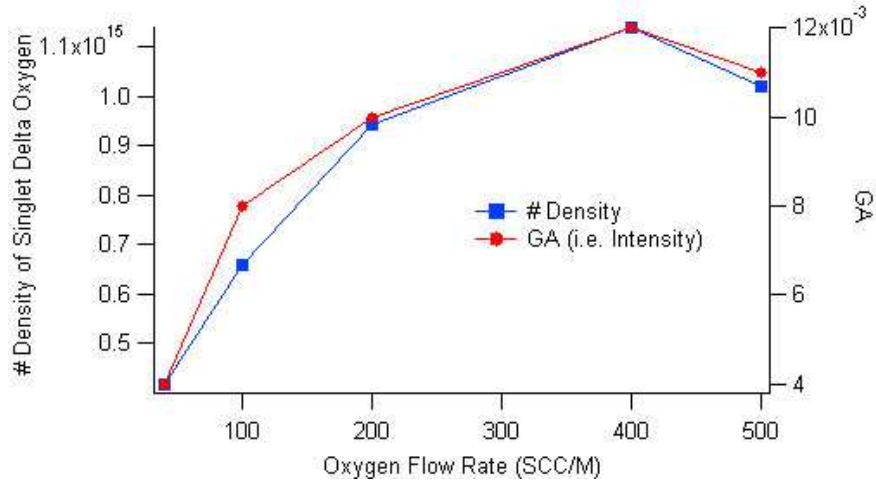
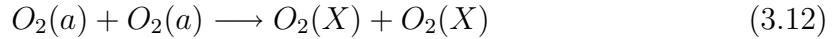


Figure 3.5: Relationship between the intensity of the signal and the number density of $O_2(a)$.

that the number density of $O_2(a)$ increases to a point as more oxygen is introduced. However, as more oxygen is introduced the yield of $O_2(a)$ decreases. This is mainly

⁶The yield is obtained by simply dividing the number density of $O_2(a)$ by the total number density of oxygen.

due to the self-quenching mechanism of $O_2(a)$.



Therefore, with more $O_2(a)$ produced there is a higher probability of self-quenching among the $O_2(a)$. Although having a background in kinetic theory would have provided an a priori to this part of the experiment, there was not enough time to explore this subject in detail. Trial and error proved to fair just as well, however, and it was concluded that setting the oxygen flow meter to 400 sccm (10% of the helium) provided the higher signal strength (Figure 3.5), even though the yield was not the highest it could have been. For measuring the exact location of the lines in $O_2(a)$, it is more important to maximize the signal-to-noise ratio than it is to maximize the yield.

3.3.2.2 Power Dependence. Another aspect to optimize in this experiment is the amount of power the microwave power supply generates. As mentioned in Section 3.2, microwaves are sent across a quartz tube via a McCarroll cavity. A Tesla coil is used to ignite the plasma, but afterwards it becomes self sustaining and stable for several hours. The microwave power supply has two analog readouts, one for the forward power and the other for the reflected power. By adjusting controls on the McCarroll cavity, it was possible to reduce the reflected power to about zero.

Once again the Q(8) line was chosen as the test line. The line was first analyzed at 60 Watts forward, and then stepped in increments of 10 Watts until 90 Watts. From the data collected and from prior experience (Williams *et al* previous work), it was concluded to use 80 Watts forward power.

3.3.2.3 Alignment. There are two very critical areas that require alignment. The first is the alignment of the cavity. Since this apparatus is designed for off-axis ICOS it is extremely important that the mirrors were aligned to give the maximum ringdown time. Recall from above that the ringdown time refers to the

amount of time it takes a photon to leave the cavity. Also recall that as the ringdown time increases, the cavity enhancement factor increases as well. So, a great deal of time was devoted to the proper alignment of this cavity. A computer was used to show the ringdown time in real-time, so that the ringdown time could be seen with each adjustment made. This alignment was only done at the start of the experiment.

The second item that required careful alignment was the laser itself. The tunable laser diodes were coupled to a fiber at one end and the other end was mounted near the entrance of the cavity. It is this mount that controls the direction of the laser beam. Once again the ringdown time was monitored as the mount was minutely adjusted. This particular alignment required a bit of give and take between maximizing the ringdown time and minimizing the noise. The ringdown time would increase as the laser beam approached the optical axis (but not on the axis), but the noise level would increase because the optical feedback would increase as the beam approached the optical axis. This alignment was probably checked every other week for about three months.

3.3.2.4 Various Other Optimizations. There are other elements that required optimizing on a more regular basis. One is the lens at the end of the cavity. Prior to collecting a series of lines for a given laser, the lens was adjusted to make sure the light exiting the cavity was focused directly onto the InGaAs detector. This ensured maximum intensity. Another aspect of optimizing is cleaning the mirrors. In earlier sections it was emphasized that the reflectivity of the mirrors play a paramount role in the cavity enhancement factor. This being said, the mirrors were cleaned from once a week to a few times a day, depending on the value of the ringdown time. The mirror reflectivities would degrade mainly due to water build up. This experiment used only helium and oxygen, but there was still traces of water from the ambient air. Even though a vacuum pump was used to pump out the ambient air from the cavity, an ideal vacuum can never be obtained. As a result, there will always be

some traces of water in the cavity⁷. In fact, water lines were frequently observed when the diode lasers were dialed through a range of energies. There were even cases when a water line either overlapped with the $O_2(a)$ line (such as R(5), P(11) and S(6)) or was within the 0.33 cm^{-1} window near the $O_2(a)$ line.

3.3.2.5 Optimizing for Pressure Broadening. After the lines were located, the next step to the experiment is to pressure broaden select lines in the $O_2(a)$ spectra. Now the importance is more on the yield of $O_2(a)$ than on the intensity. This is due to the fact that at higher pressures the probability of self-quenching increases and it becomes difficult to keep $O_2(a)$ sustained in the cavity. For example, if the flow rate of oxygen was kept at 400 sccm and the total pressure in the cavity is increased to 100 Torr (from about 20 Torr), then the line would simply vanish into the noise level. In fact, under these conditions the Q(8) line was difficult to see at 50 Torr. Having this knowledge, and the information from Figure 3.4, the oxygen was chosen to be set at 50 sccm. This corresponds to about 1% of the helium.

In order to extract a pressure broadening coefficient for a given line, the Lorentzian linewidth must be determined from the fit data. It becomes critical then that the shape of the Voigt lineshape, especially the wings, is not distorted as the laser scans through the line. For determining the positions of the lines a scanning rate of 25 Hz was more than adequate. For pressure broadening, however, this was too fast. Many trial runs were conducted using 25 Hz, 10 Hz, and 5 Hz scan rates. The distortion can be observed when the Voigt profile is fit to the data. Specifically, the raw data would lean to the left or right on either side of the fitted Voigt profile⁸. The 25 Hz scan proved too fast, because the Voigt fit clearly misses the data in Figure 3.6. However, there was virtually no distortion observed in either the 10 or the 5 Hz scan (Figures 3.7 and 3.8 respectively). In fact, there didn't appear to be any significant difference between the two other than the 5 Hz scan produced more noise. Actually,

⁷The porous nature of the plastic gas lines used in the apparatus allowed water to always be present.

⁸For examples of this refer to the data presented in Appendix C.

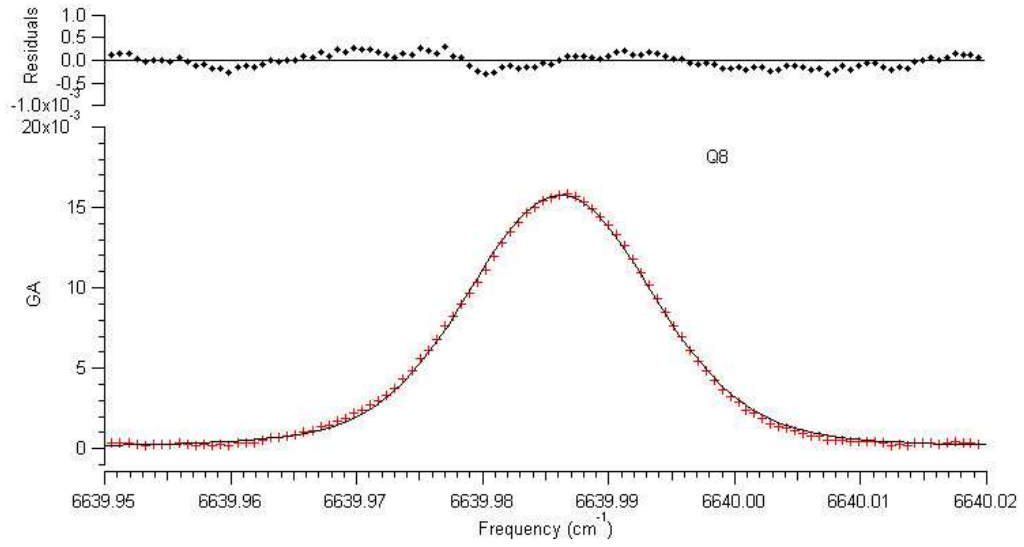


Figure 3.6: This is the Q8 line scanned at 25 Hz. Total pressure in the cavity was ca. 25 torr, with a ringdown time of 203 μs . The data was averaged 10000 times and binned 40 times.

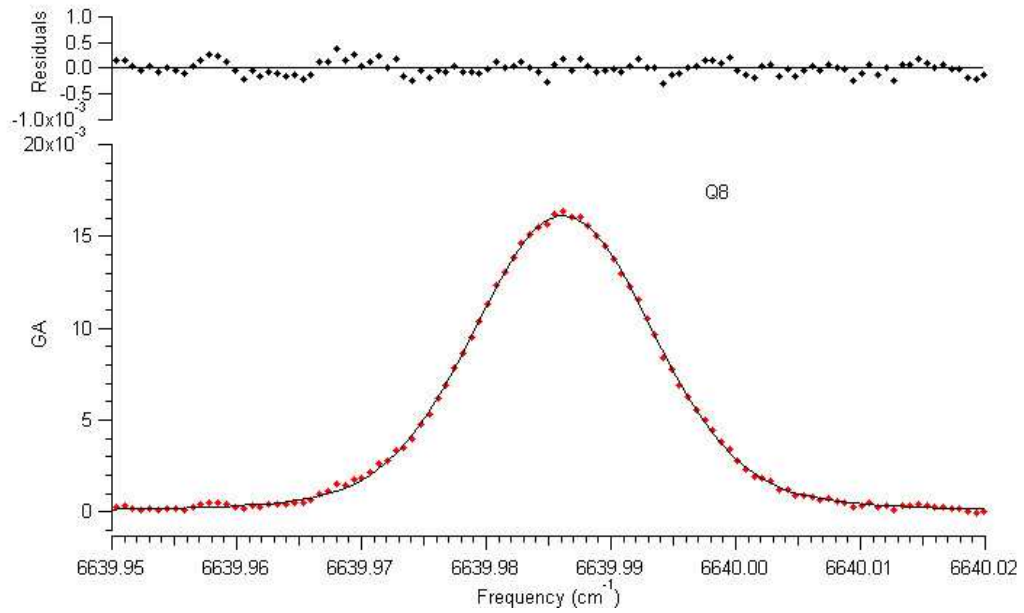


Figure 3.7: This is the Q8 line scanned at 10 Hz. Total pressure in the cavity was ca. 25 torr, with a ringdown time of 203 μs . The data was averaged 4000 times and binned 100 times.

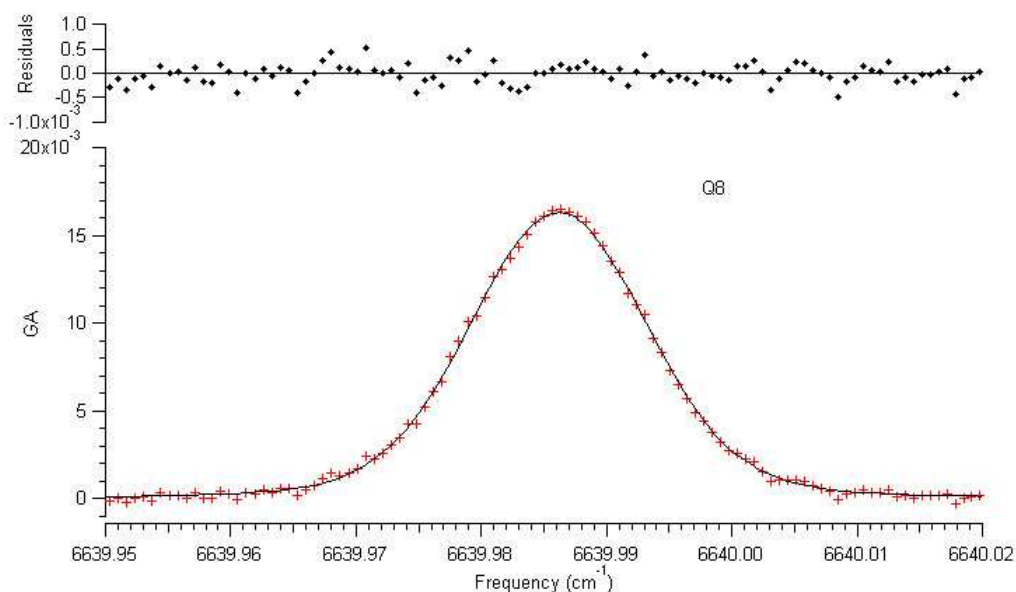


Figure 3.8: This is the Q8 line scanned at 5 Hz. Total pressure in the cavity was ca. 25 torr, with a ringdown time of 203 μ s. The data was averaged 1000 times and binned 200 times.

the reason why the 5 Hz scan appeared to produce more noise was because the 25 Hz scan was averaged 10,000 times, the 10 Hz scan 4,000 times and the 5 Hz scan 1,000 times. These averages were chosen in order to keep each scan per line under ten minutes. When pressure broadening, each line was scanned at four different pressures from 25 Torr to 100 Torr, so each line took about 45 minutes to scan.

3.3.3 Taking Data. Section 3.2 dealt with the apparatus in the sense of how the singlet delta oxygen is produced and how it is collected by the laser and the detector. This section will instead focus on the computer program used to collect the raw data.

There are actually two programs used when taking the data. The first is called *Noxon*. This program displays and exponentially fits the ringdown curve in real-time and calculates the ringdown time. This program was essential in both determining the ringdown time for a given series of scans, and aided in the maintenance of the apparatus since a low ringdown time corresponded to dirty mirrors or bad alignment. Figure 3.9 shows an example of the ringdown curve. The shape is a result from

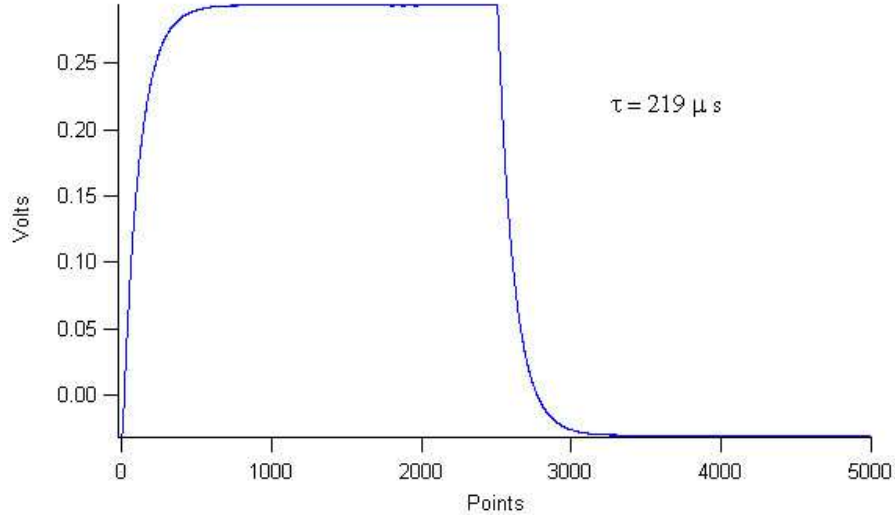


Figure 3.9: The ringdown curve for $\tau = 219 \mu s$.

modulating the laser with a square wave which simulates the pulsed lasers mentioned earlier. When the laser is "switched off" the exponential decay of the light within the cavity is clearly seen. The light will also decay "up" until the cavity reaches steady-state conditions, which corresponds to when the re-entrant condition is met. This occurs at approximately 80,000 passes in the cavity for this experiment.

The other computer program is aptly called *ICOS*. This program is the main interface between the user and the apparatus. This program displays both the real-time signal and the averaged signal on the same screen. It is this program that allows the user to adjust the sampling rate, the repetition rate, the signal type, the voltage offset and amplitude, the input channel, and the number of averages. The repetition rate (or rep rate) means that each data point will be sampled a certain number of times; this is measured in Hertz. Whereas the sampling rate is measured in points per second and refers to the total amount of samples taken by the detector, regardless of repetitions. For example if the sampling rate is 500,000 Hz and the rep rate is 25 Hz, then there will be 20,000 data points that will describe a line. When a ringdown is measured, using this program, the rep rate is set at 100 Hz, so there will be 5,000 data points to describe the ringdown curve. This is shown along the x-axis in Figure ??.

The signal type refers to the type of waveform with which the laser can be modulated. A square waveform is used for generating a ringdown curve and a sawtooth waveform is used when scanning a line. The input channel allows the user to toggle between the InGaAs detector and the etalon measurement. Finally the number of averages refers to how many times a frequency will be averaged. When determining the line's position the number of averages was set to 10,000 times. It was mentioned above that at 25 Hz rep rate there will be 20,000 data points to describe the line, so each of the 20,000 points will now be averaged 10,000 times. This is why it took approximately ten minutes to scan each line. The following section will cover the process of analyzing the data that these programs saved as text files.

3.3.4 Analyzing Data. The raw data obtained from the InGaAs detector, which was saved as a text file, is then processed using another computer program called IGOR Pro[®]. Williams wrote macro program files specifically for the analysis of this type of data.

When the data is first uploaded into the program it is convenient to overlay the raw data trace (the absorption line in the sawtooth waveform) with the etalon function. This is displayed in Figure 3.10.

Explain better (include the binning process)

The etalon function tells the user how many fringes were present within the laser's 0.33 cm^{-1} scanning "window" for each line. More importantly however, the etalon provides the function which will determine the non-linear relationship between point-space (labeled as Point Number) and frequency-space. Although it is not apparent in this example (Figure 3.10), the fringe peaks are not equally spaced in point space. In fact, if the laser was allowed to scan at a higher rep rate, then many fringes would be seen and there would be a visible bunching of fringe peaks of varying separation intervals. However, an etalon will alleviate this problem since the free-spectral range⁹ of that etalon is the spacing between the fringes in frequency-space.

⁹The free-spectral range is 2 GHz for the etalon used.

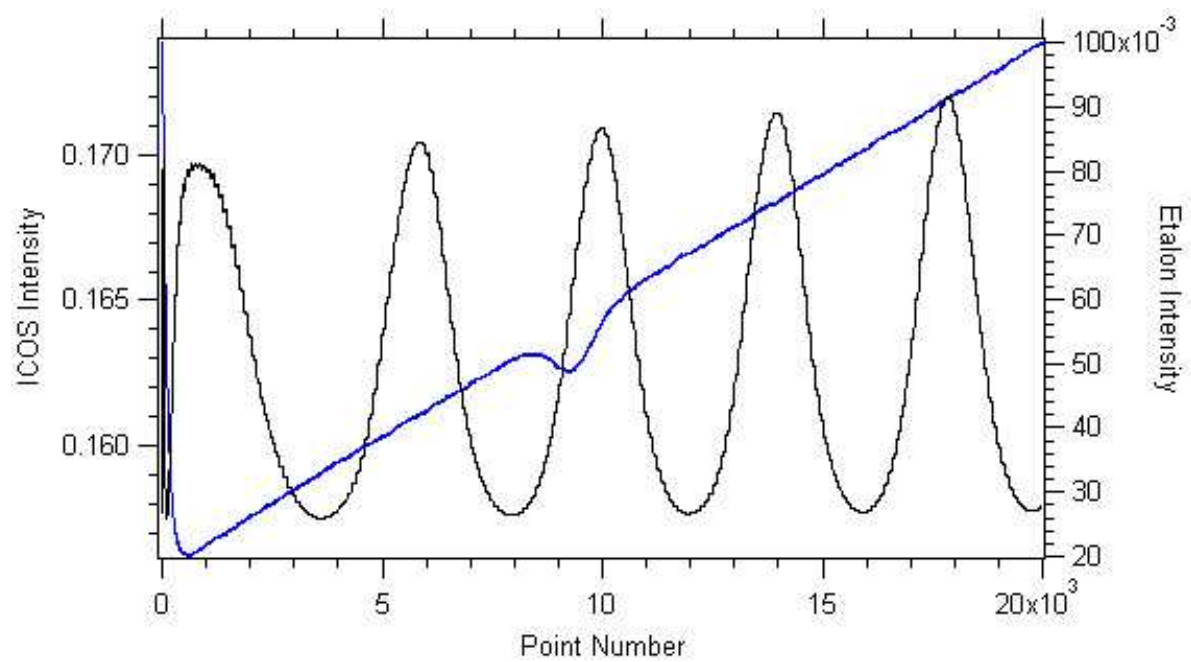


Figure 3.10: The raw data for R(7) with the etalon function.

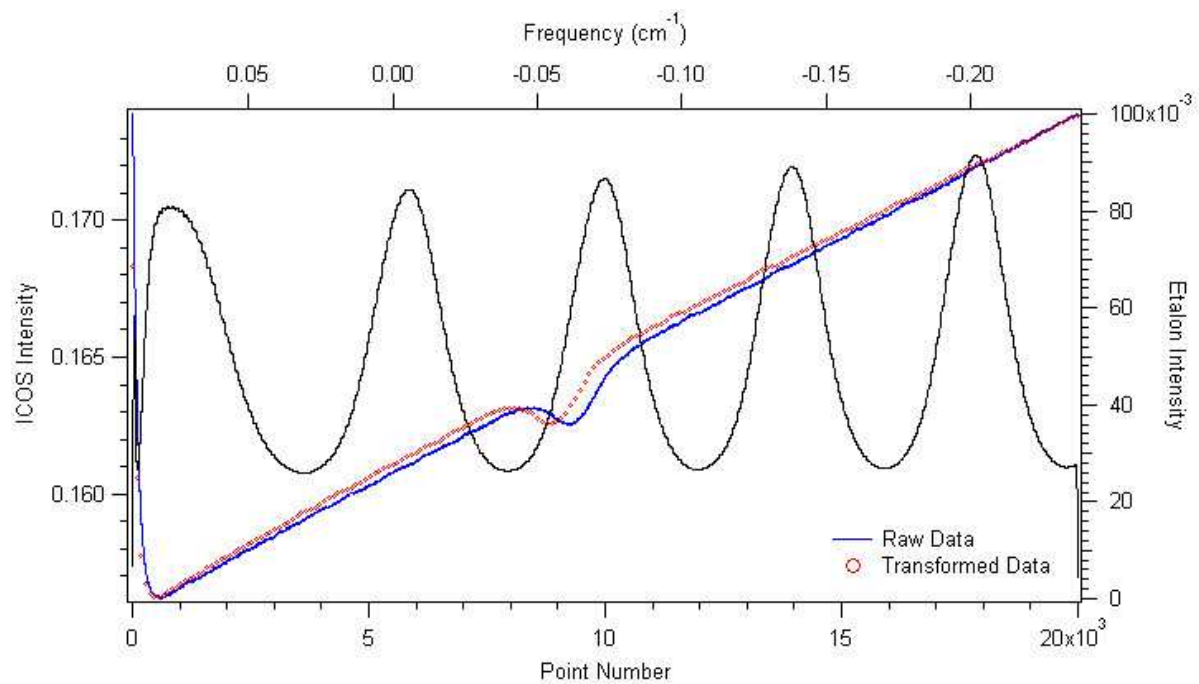


Figure 3.11: The etalon is used to convert the R(7) data to frequency-space.

Therefore, the step being performed between Figure 3.10 and Figure 3.11 is first identifying the mathematical function which will transform the data points to points in frequency-space, and then performing this function on the raw data. The result of this transformation is shown in Figure 3.11 and the new absorption feature is now plotted as a function of some arbitrary frequency of units cm^{-1} . The data in frequency-space is bowed out from the original data because the non-linear transformation function is parabolic.

After the data has been corrected for frequency-space, the data is then binned. Binning refers to the process of averaging a group of points together to form one point. This averaging will also reduce the statistical noise level. It was mentioned earlier that the sampling rate and scan rate both play a factor as to how many points will represent a particular line in the spectra. Since the sampling rate was fixed at 500 kHz throughout the entire experiment, a 10 Hz scan produced 50,000 points and a 25 Hz scan produced 20,000 points. Now, in this experiment 10 Hz scans were binned at 100 times, which reduced 50,000 points to 500 points, and the 25 Hz scans were binned at 40 times, which reduced 20,000 points to 500 points. These two scan rates (10 Hz and 25 Hz) can now be properly compared to one another, given the fact that they now have the same number of data points representing the absorption feature.

The next step is where physics plays a role. ICOS theory provides a relationship among the intensity of the empty cavity ($I(\alpha L = 0)$), the intensity of the cavity with the absorber present ($I(\alpha L)$) and the Voigt profile of that absorber (GA). These quantities are related to each through the following equation¹⁰.

$$\frac{I(\alpha L = 0)}{I(\alpha L)} - 1 = GA \quad (3.13)$$

This is the exact form used in the macro file in IGOR Pro[®]. How this relation is used is better understood if some direct comparisons are made to (3.13). Since G

¹⁰A full mathematical development of this equation from the Beer-Lambert formula is provided in Appendix A.

is the cavity enhancement factor and A is the single-pass absorption (SPA) feature, then GA can be viewed as the enhanced single-pass absorption of the absorption species; in other words $G(SPA)$. Since $I(\alpha L = 0)$ is the output intensity of the empty cavity, then we can equate this quantity to the baseline polynomial fit ($I(\alpha L = 0) = \text{Baseline}$). Since $I(\alpha L)$ is the output intensity of the cavity with the absorbing species present, then we can equate this quantity to the raw data taken from the InGaAs detector ($I(\alpha L) = \text{Rawdata}$). Writing this out in equation form we have,

$$\frac{\text{Baseline}}{\text{RawData}} - 1 = G(SPA) \quad (3.14)$$

Figure 3.12 shows the polynomial fit to the baseline, the Voigt fit to the peak and

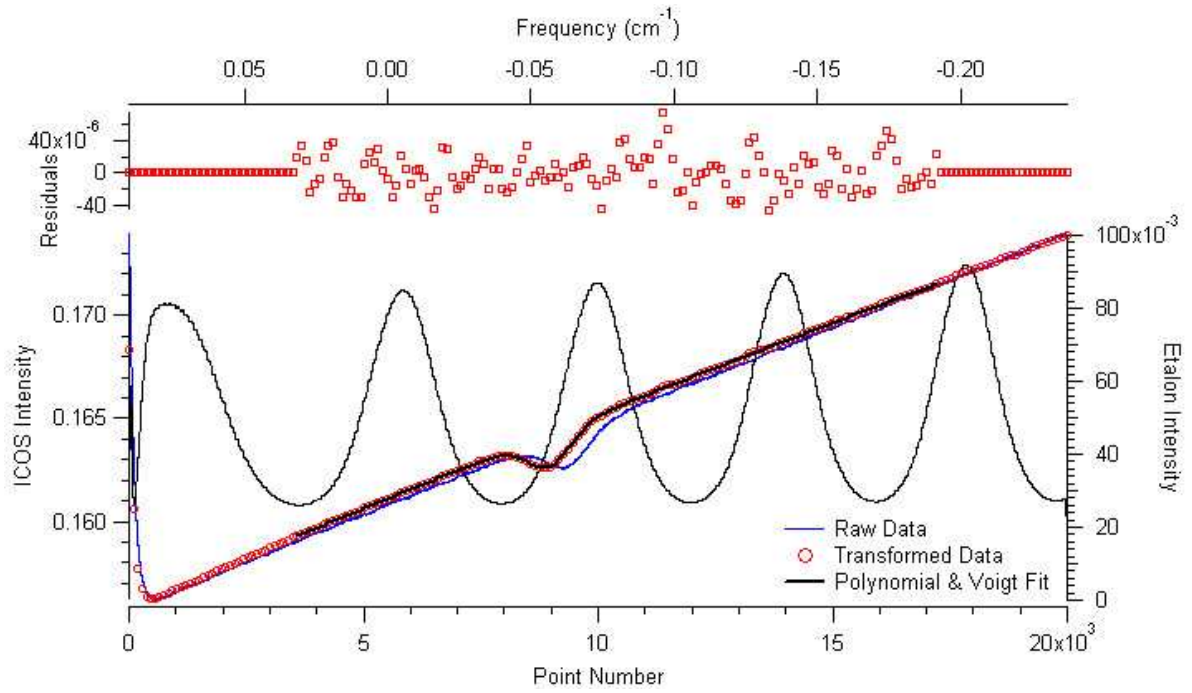


Figure 3.12: The absorbance is calculated.

the corresponding residuals. According to equation (3.14) the macro then divides the baseline out of the raw data, subtracts one (this will invert the absorption peak) and then calculates the value of GA . This GA value will correspond to the peak of the line shape. The result is shown in Figure 3.13. Finally, the last macro is performed

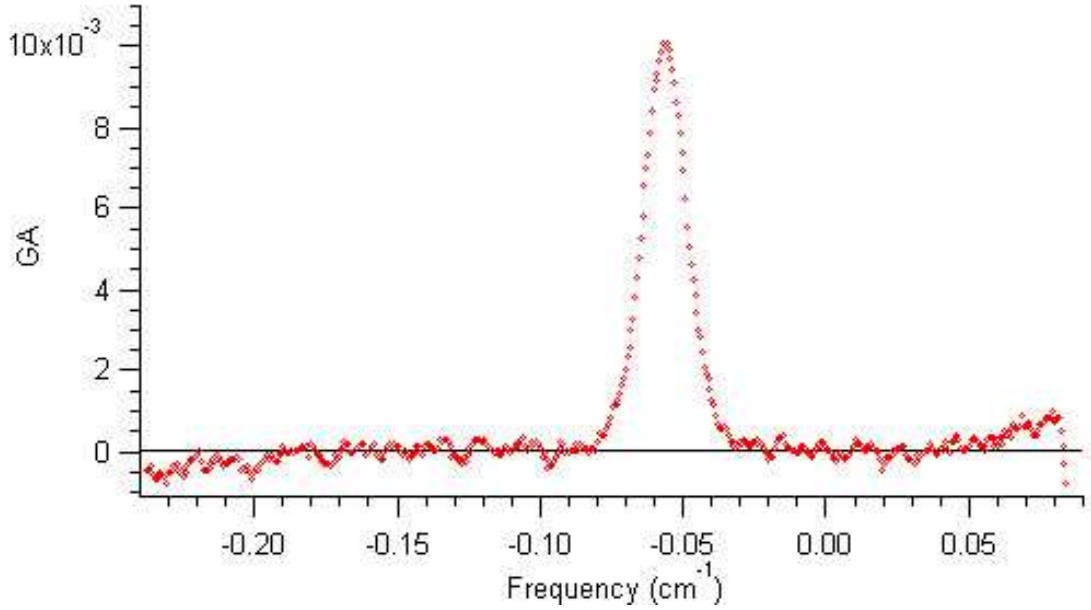


Figure 3.13: The baseline is removed and the R(7) peak is all that remains.

and those result are shown in Figure 3.14. Three main calculations take place in this macro. First, another more accurate Voigt profile is fit to the data. This is done now that the baseline is removed, so the values for the Gaussian and the Lorentzian lineshape functions will be more accurate. The next calculation involves the cross section of the line. The third and final calculation finds the peak location in frequency-space by inserting the value obtained from the wavemeter. The wavemeter was used during the collection of each line, via the fiber optic attenuator. The wavemeter provided the frequency of the peak of the laser line width to an accuracy of 0.004 cm^{-1} . The peak of the laser line width correspond to the center point of the raw data in point-space (i.e. the center of the graph in Figure 3.10). Since the line is already transformed to the laser's frequency-space, the program simply replaces the center frequency with the peak frequency found by the wavemeter. The x-axis is then scaled to this new frequency, and the result is shown in Figure 3.14.

3.3.4.1 Taking Data for Pressure Broadening. When acquiring data for pressure broadening all of the above procedures are still followed. The only differ-

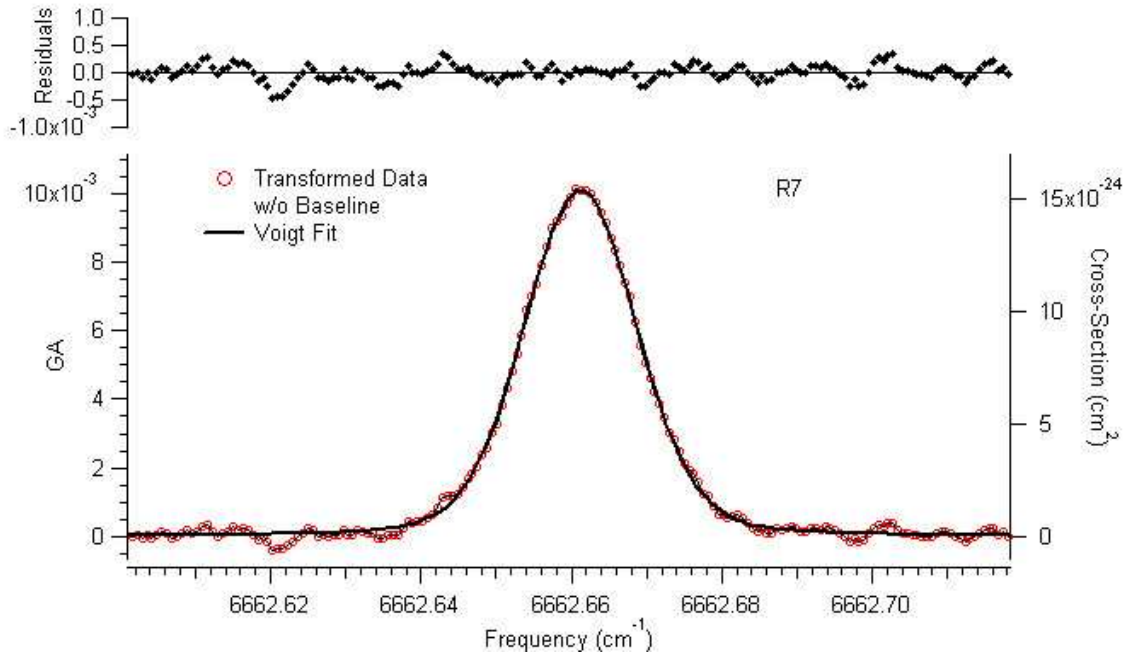


Figure 3.14: A Voigt profile is fit to the peak and the peak cross section is calculated. This is the final step in the analysis process.

ence is the fact that each line must now be scanned four times in a row, corresponding to each of the four pressures. Those four pressures are 25 Torr, 50 Torr, 75 Torr and 100 Torr. These four pressures are unique in and of themselves since most spectroscopists start at or above 100 Torr.

IV. Results and Discussion

The results presented in this chapter prove with great success the ability off-axis ICOS has to detect extremely weak absorption signals. All results are focused on the (1,0) band of the $b^1\Sigma_g^+ \leftarrow a^1\Delta_g$ system in oxygen. The first set of results confirms the absolute line positions of 21 lines and are compared with the expected positions predicted from the Cheah and Lee results [27] of the $O_2(a)$ and $O_2(b)$ term energies. Thirteen of these lines have never been observed before. These lines encompass all five branches, which are predicted by quantum mechanics and are shown in the Herzberg diagram in Section 2.2.5. The next set of results verify the integrated cross sections¹ using a form of Boltzmann analysis. The final set of results list pressure broadening coefficients for select lines in the (1,0) band and verifies, for the first time, the rotational dependence on pressure broadening for an electric-quadrupole transition. Although the results are mainly presented in tabular form in this chapter, all of the analyzed lines are presented graphically in Appendix C.

4.1 The Absolute Line Positions

The direct quantitative determination of the absolute line positions for the O,P,R and S branches of the $b^1\Sigma_g^+ \leftarrow a^1\Delta_g$ (1,0) transition of oxygen had not been accomplished before this experiment. Williams *et al* [24], however, already measured the Q branch quantitatively from J=2 through J=16. The same Q's were measured in this experiment and the values agree to within 0.001cm^{-1} of Williams' values.

All of the measured values from this experiment, presented in Table 4.1, are compared to their predicted values calculated from the Cheah and Lee results^{2,3}. Prior to the invention of the off-axis ICOS technique, the energies for the Noxon band could only be calculated from subtracting the term energies $a^1\Delta_g \leftarrow X^3\Sigma_g^-$ from $b^1\Sigma_g^+ \leftarrow X^3\Sigma_g^-$. The measured values differ from the predicted values by 0.0001cm^{-1}

¹These integrated cross sections were first calculated by Dr. Skip Williams

²The process of how Cheah and Lee's results were used to determine the band energies are presented in Appendix C, in the form of a Matlab® code.

³The spectroscopic values used for the Hamiltonian were taken from the Cheah and Lee paper [27].

Table 4.1: Absolute Line Positions in Wavenumbers (cm^{-1}).

Line	Quantitative Measurement	1σ Error	Predicted from Cheah <i>et al</i>	Difference
O6	6611.1418	± 0.0046	6611.13567869935	0.0061
O8	6598.8226	± 0.0046	6598.81569124817	0.0069
P9	6614.4826	± 0.0046	6614.47987116784	0.0027
P13	6599.3977	± 0.0046	6599.39161739536	0.0060
P15	6591.3228	± 0.0046	6591.31499534225	0.0077
Q2	6642.9513	± 0.0047	6642.94970151615	0.0015
Q4	6642.3227	± 0.0046	6642.32129012862	0.0013
Q6	6641.3324	± 0.0046	6641.33355116894	0.0011
Q8	6639.9878	± 0.0046	6639.98617083616	0.0016
Q10	6638.2786	± 0.0046	6638.27872121984	0.0001
Q12	6636.2118	± 0.0046	6636.21066030018	0.0011
Q14	6633.7802	± 0.0046	6633.78133194786	0.0011
Q16	6630.9987	± 0.0046	6630.98996592416	0.0087
R3	6653.6667	± 0.0047	6653.66273921216	0.0039
R7	6662.6576	± 0.0047	6662.6612178316	0.0035
R9	6666.6174	± 0.0047	6666.61516949024	0.0022
R11	6670.2048	± 0.0047	6670.20360286338	0.0012
R13	6673.4308	± 0.0047	6673.42488042498	0.0059
R17	6678.7650	± 0.0047	6678.75884746335	0.0061
R19	6680.8693	± 0.0047	6680.86769134183	0.0016
S8	6692.1316	± 0.0047	6692.12146915857	0.0101

for Q(10), to $0.01cm^{-1}$ for S(8). The S(8) line was the weakest line measured ($GA = 2.47554 \times 10^{-3}$ for S(8) compared to $GA = 1.99853 \times 10^{-2}$ for Q(8)) in this experiment and was the most difficult to fit. It is clearly shown in Appendix C that the fitted peak slightly misses the 'real' peak of the data. This was the best fit, however, for this line.

The error has been derived from the wavelength accuracy of the wavemeter used to locate the peak center of the laser linewidth when scanning through an absorption line. For example, the calibration chart that came with the wavemeter indicated that for a line at $1500nm$ the wavemeter would have an error ($\Delta \lambda$) of 1.05 ppm⁴.

⁴parts per million

Therefore, the error in wavenumbers was found using the following equation.

$$|\tilde{\nu}| = \left| \frac{\Delta \lambda}{\lambda^2} \right| \quad (4.1)$$

The measured results in Table 4.1 agree well with the known spectroscopic theory. This means that the off-axis ICOS technique does indeed find extremely weak transitions, such as produced from electric-quadrupole transition.

The Q(8) line shown in Figure 4.1 is an example of what the line looks like in frequency-space after being fully analyzed from the raw data collected by the apparatus⁵. The line's cavity enhanced absorption (GA) is plotted as a function of frequency (cm^{-1}). The black line represents the actual data which has been transformed non-linearly and has had its baseline removed. The red line is the Voight fit to the data. Recall that the peak cross section, which is along the right y-axis, can be thought of as a cavity enhanced integrated absorption cross section. The residuals above the peak represent the difference between the raw data and the Voight fit. The best signal to noise ratio (SNR) obtained in this experiment was 40:1⁶. Although much time and effort was devoted to increasing this ratio, it still fell short of the 150:1 results Williams *et al.* [24] had achieved. Williams was able to achieve such a high SNR because he had both a higher ringdown time ($250\mu s$ compared to $220\mu s$) and a higher yield of $O_2(a)$ (5% conversion efficiency compared to 2.7%). However, this experiment did achieve noise levels lower than Williams *et al.*

4.2 Verification of the Integrated Absorption Cross Sections

This experiment also successfully verified the intrinsic integrated absorption cross sections for all the lines of Table 4.1. This was done by using a form of Boltzmann analysis. These integrated absorption cross sections were neither measured nor calculated in this experiment, but were first calculated by Williams *et.al.* [24].

⁵See Chapter III for a detailed explanation of the procedure.

⁶This ratio was calculated for the Q(8) line. The worst SNR obtained was 5:1 for the very weak S(8) line.

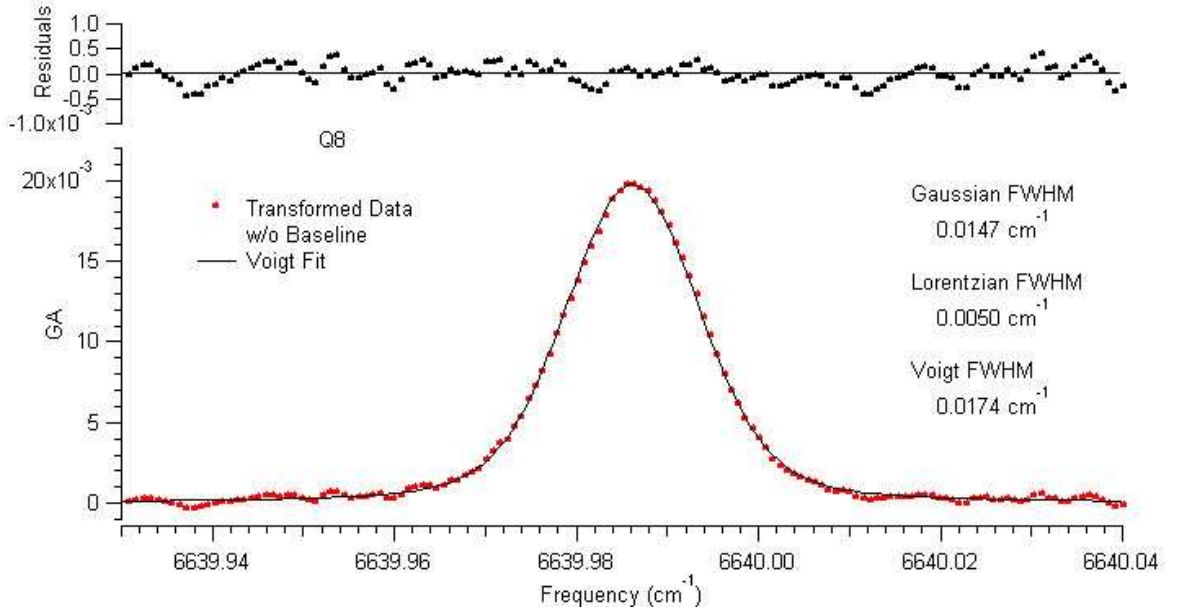


Figure 4.1: The Q(8) line position at 6639.9878cm^{-1} . The total pressure in the cavity was ca. 25 torr, the ringdown time was $216\ \mu\text{s}$, and the rep rate was 25 Hz. The data was binned 50 times.

4.2.1 Boltzmann Analysis. To verify the integrated absorption cross sections listed in Table 4.2, the following three equations were used.

$$f_B = (2S + 1)(2J + 1)e^{-\frac{E_J}{kT}} \quad (4.2)$$

$$[O_2(a)] = N_a f_B \quad (4.3)$$

$$A = [O_2(a)] L \sigma_I \quad (4.4)$$

Where f_B is the boltzmann factor, E_J is the rotational energy, T is the rotational temperature, $[O_2(a)]$ is the concentration of $O_2(a)$, N_a is the number density of $O_2(a)$, A is the peak area from the Voigt fit⁷, L is the length of the cavity, and σ_I is the integrated absorption cross section. After substitution and manipulation of the above

⁷This is found from the following relation, $\frac{GA}{G}$.

Table 4.2: Verified Integrated Cross Sections ($\frac{cm^2}{cm^{-1}}$).

Line	Integrated Absorption Cross Sections, $\sigma_I \frac{cm^2}{cm^{-1}}$
O6	$1.50233753287255 \times 10^{-25}$
O8	$1.34644197315733 \times 10^{-25}$
P9	$4.44880627547526 \times 10^{-25}$
P13	$4.23990875270618 \times 10^{-25}$
P15	$4.16985296122742 \times 10^{-25}$
Q2	$4.44797314593381 \times 10^{-25}$
Q4	$5.45732707987711 \times 10^{-25}$
Q6	$5.65692593379 \times 10^{-25}$
Q8	$5.72787157770784 \times 10^{-25}$
Q10	$5.75900341017908 \times 10^{-25}$
Q12	$5.77335389737773 \times 10^{-25}$
Q14	$5.77909588510437 \times 10^{-25}$
Q16	$5.77973206313335 \times 10^{-25}$
R3	$2.23476375652766 \times 10^{-25}$
R7	$3.14138016279576 \times 10^{-25}$
R9	$3.31260656007808 \times 10^{-25}$
R11	$3.42615296599517 \times 10^{-25}$
R13	$3.5073662886619 \times 10^{-25}$
R17	$3.61623411380298 \times 10^{-25}$
R19	$3.65446514511864 \times 10^{-25}$
S8	$6.8986524783927 \times 10^{-26}$

equations it can be easily shown that,

$$\ln \left(\frac{A}{\sigma_I (2S+1)(2J+1)} \right) = -\frac{E_J}{kT} \quad (4.5)$$

If the lines are plotted with their $\ln \left(\frac{A}{\sigma_I (2S+1)(2J+1)} \right)$ values as a function of their individual rotational energy, E_J , the slope that results will simply be $-\frac{1}{kT}$. From this slope, the temperature within the cavity is obtained. Now, when the $O_2(a)$ leaves the plasma and travels to the cavity the temperature of the $O_2(a)$ will decrease quickly to a value near room temperature ($\approx 300K$). Therefore, the slope must yield a temperature near room temperature in order to verify the integrated cross

sections. All 21 lines have been used in this experiment to generate the slope shown

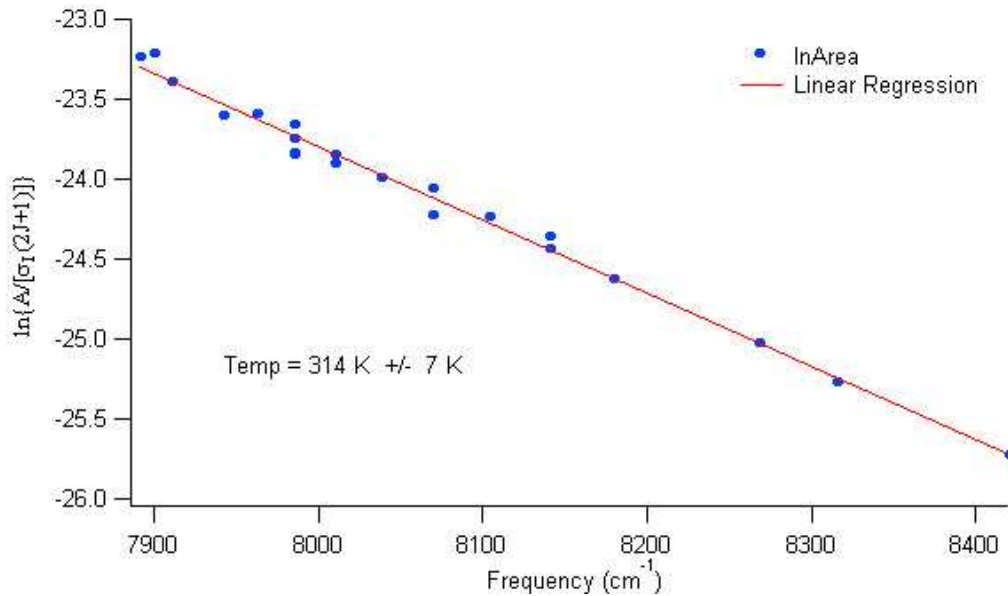


Figure 4.2: Boltzmann analysis.

in Figure 4.2. A temperature of $314K \pm 7K$ was obtained from the slope of the linear regression of the data. This result compares extremely well to published results. In 2004, Williams *et al.* [24] calculated a temperature of $312K \pm 14K$ using the same Boltzmann analysis on the same transition band of oxygen⁸. In 1985, Fink *et.al.* [6] calculated a temperature of $313K \pm 10K$ using the same Boltzmann analysis from the emission spectra of the (0,0) band of the $b^1\Sigma_g^+ \rightarrow a^1\Delta_g$ system of oxygen. More importantly, however, this temperature of $314K \pm 7K$ is consistent with the integrated absorption cross sections calculated by Williams. Therefore, the calculated integrated cross sections correlating to the lines in this experiment have been verified experimentally.

This temperature plays a crucial role in extracting the Lorentzian line widths of the lines when pressure broadened. This is done by fixing the Gaussian width at this temperature. This can be done since the Gaussian profile is a result of Doppler broadening which is dependent on the temperature. The following equation illustrates

⁸ $b^1\Sigma_g^+ \leftarrow a^1\Delta_g (1,0)$

this relationship.

$$\Delta \nu_D = 2 \nu_0 \sqrt{\frac{2 k T \ln(2)}{m c^2}} \quad (4.6)$$

Where $\Delta \nu_D$ is the Doppler FWHM, ν_0 is the natural FWHM, T is the temperature, and m is the mass of the molecule or atom. The pressure broadening results will be presented in the following section

4.3 Pressure Dependence of Line Width (FWHM)

The final goal for this experiment is to pressure broaden select lines in order to extract a pressure broadening coefficient. The ten strongest lines were chosen for their ability to be detectable at 100 Torr⁹. Four pressures were used in this experiment; 25, 50, 75, and 100 Torr. Figures 4.3-4.6 graphically illustrates the Q(8) line being pressure broadened at four pressures. To obtain the pressure

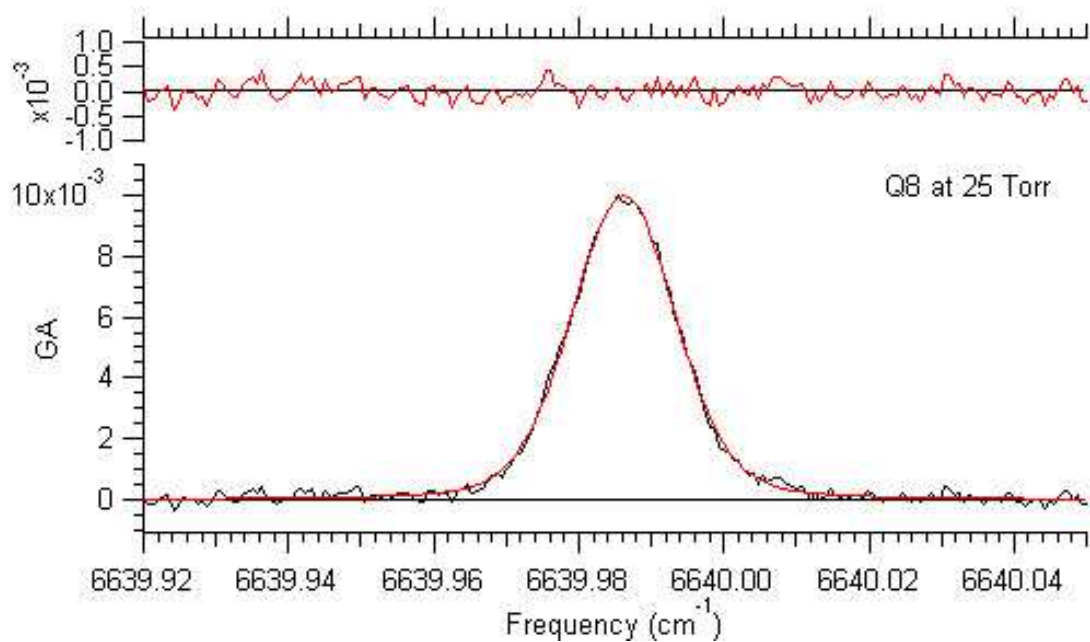


Figure 4.3: The Q(8) line pressure broadened at 25 Torr

broadening coefficient, the resulting Lorentzian linewidth are then plotted against

⁹The cavity was typically at 20 Torr with the back valve completely open

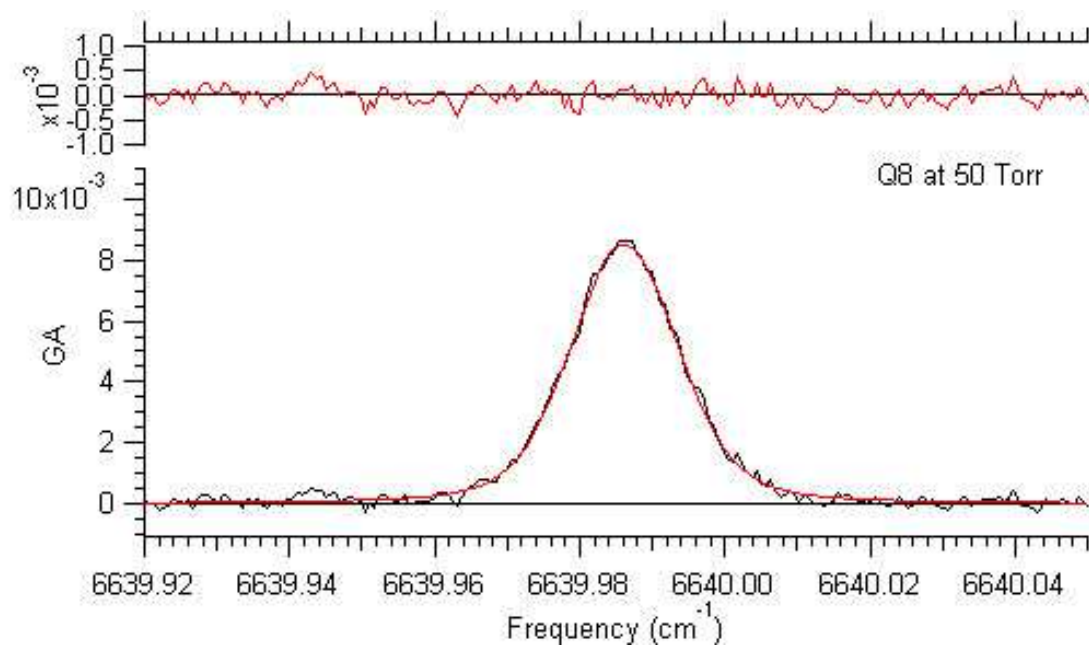


Figure 4.4: The Q(8) line pressure broadened at 50 Torr

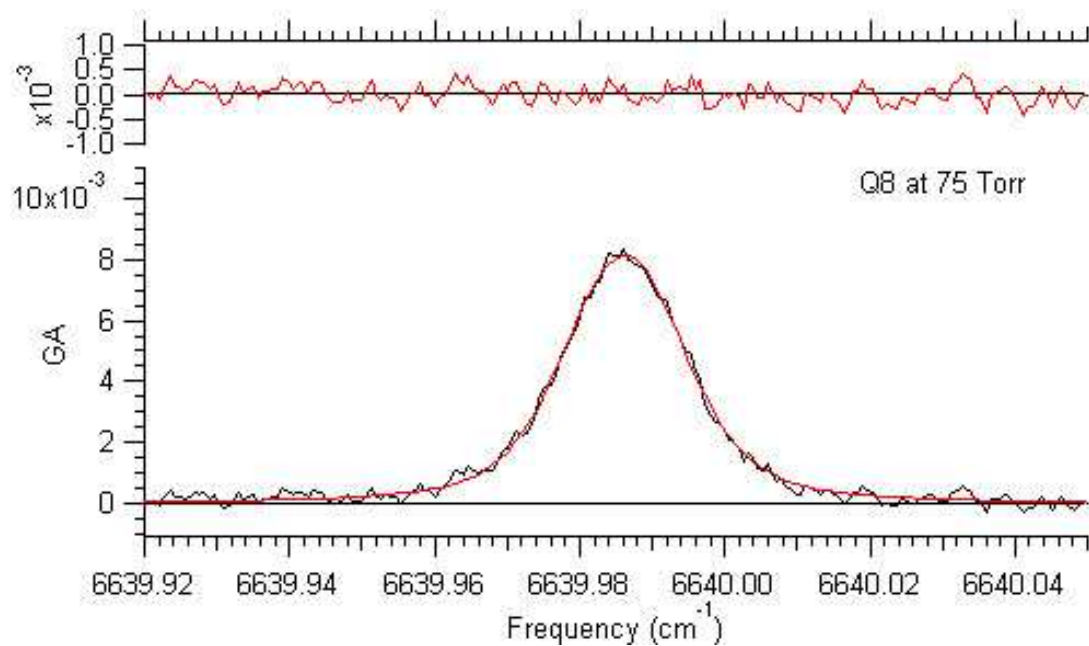


Figure 4.5: The Q(8) line pressure broadened at 75 Torr

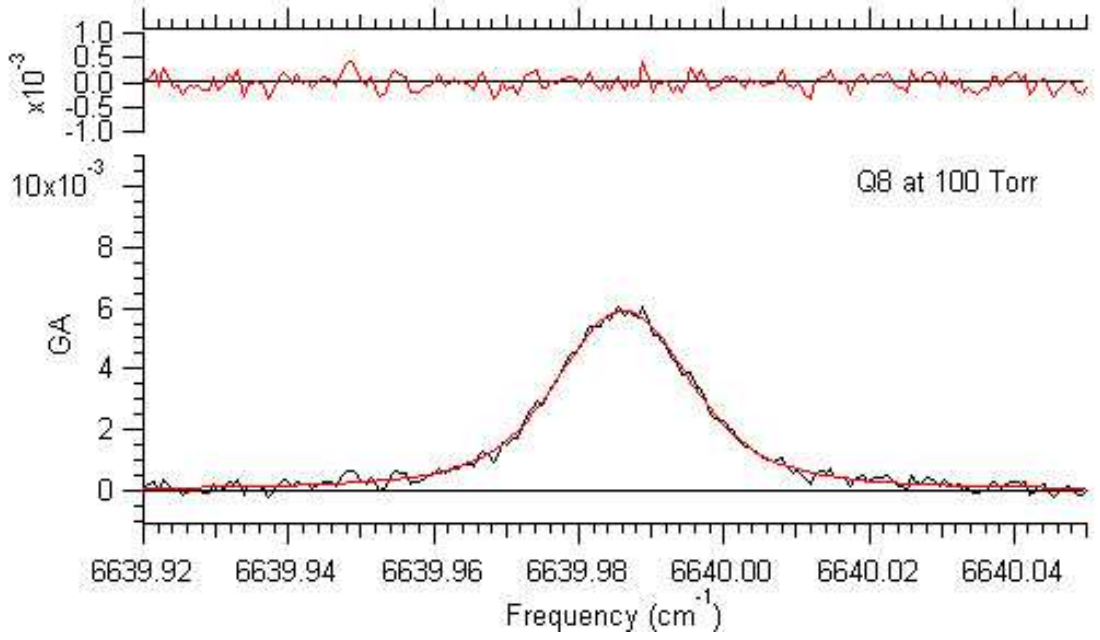


Figure 4.6: The Q(8) line pressure broadened at 100 Torr

pressure, shown in Figure 4.7. Each data point is a full ten minute scan at the specified pressure. The error bars are a 2σ uncertainty in the fit to the Lorentzian FWHM. To acquire decent survey data of the Q(8) line sixteen scans were taken, four for each of the four mentioned pressures. After plotting the results, a linear regression was taken with a weighted error. The parameters from this line equation yielded two important quantities. The most important parameter was the slope, since this is equal to the peak's pressure broadening coefficient, γ_p . Once the the pressure broadening coefficient is determined, the Lorentzian FWHM ($\nu_{1/2}$) of the line can then be calculated at any given pressure (p) from the relation [2],

$$\nu_{1/2} = \gamma_p p + \text{intercept} \quad (4.7)$$

The pressure broadening coefficients for the chosen ten lines are presented in Table 4.3 along with their 1σ uncertainties.

The second parameter is the y-intercept. This quantity proved to be both interesting and perplexing. In the absence of pressure, equation 4.7 states that the

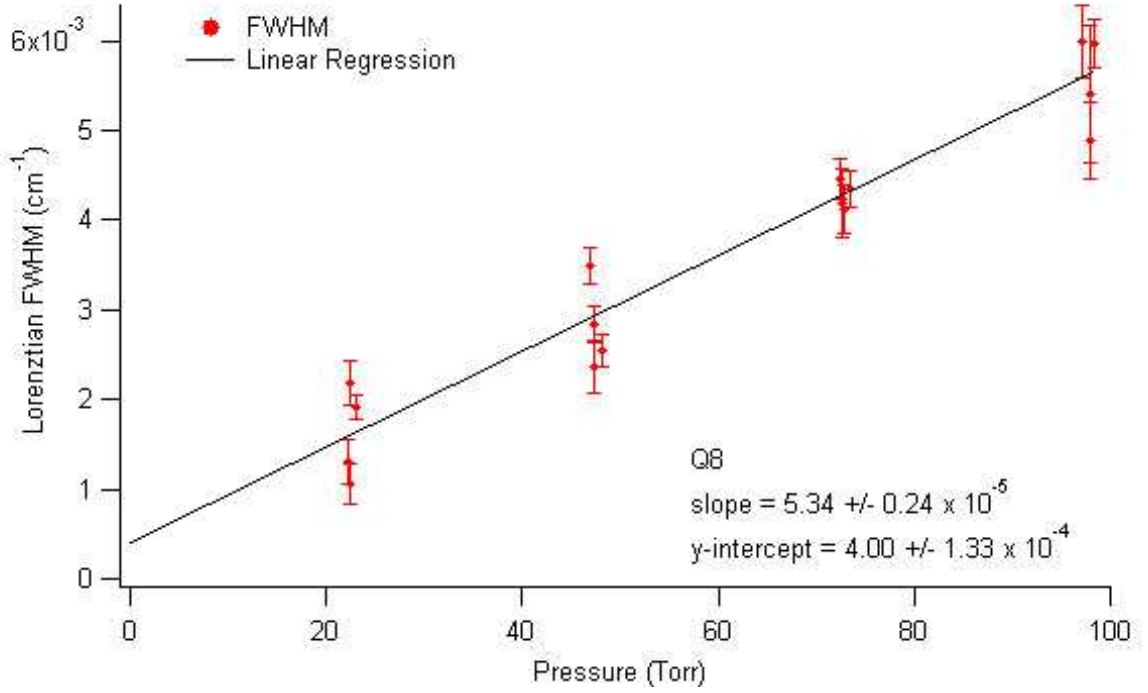


Figure 4.7: Slope of regression line is the pressure broadening coefficient in $\text{cm}^{-1} \text{Torr}^{-1}$.

FWHM should be zero. This means the linear regression line in Figure ?? needs to pass through the origin or near the origin within reasonable uncertainty. The data in this experiment did not show this. One cause for this y-intercept could be the signal response function of the instrument used in this experiment. This is possible because this experiment resolves linewidths as small as 0.001 cm^{-1} . Further work will be required to fully explain this issue. The y-intercepts along with their error is also presented in Table 4.3.

4.3.1 Rotational (J) Dependence on Pressure Broadening Coefficients. The final graph of this chapter (Figure 4.8) depicts the rotational dependence of the pressure broadening coefficients. Newman and Orr-Ewing [26] created a similar graph for the $a^1\Delta_g \leftarrow X^3\Sigma_g^- (0,0)$ transition. The trend for their data and the trend shown in Figure 4.8 both suggest that as the rotational quantum number increases, the influence that the collisions have on the Lorentzian lineshape decreases. Pope, for his

Table 4.3: Pressure Broadening Coefficients.

Line	Pressure Broadening Coefficient ($cm^{-1}/torr$)	1σ Error ($cm^{-1}/torr$)	Y-Intercept (cm^{-1})	1σ Error (cm^{-1})
P9	4.83×10^{-05}	$\pm 2.76 \times 10^{-06}$	4.37×10^{-04}	$\pm 1.54 \times 10^{-04}$
Q4	5.81×10^{-05}	$\pm 3.51 \times 10^{-06}$	6.42×10^{-04}	$\pm 2.30 \times 10^{-04}$
Q6	5.06×10^{-05}	$\pm 2.72 \times 10^{-06}$	4.75×10^{-04}	$\pm 1.55 \times 10^{-04}$
Q8	5.34×10^{-05}	$\pm 2.43 \times 10^{-06}$	4.01×10^{-04}	$\pm 1.33 \times 10^{-04}$
Q10	4.98×10^{-05}	$\pm 5.51 \times 10^{-06}$	3.18×10^{-04}	$\pm 2.97 \times 10^{-04}$
Q12	4.19×10^{-05}	$\pm 2.91 \times 10^{-06}$	7.99×10^{-04}	$\pm 1.65 \times 10^{-04}$
Q14	3.76×10^{-05}	$\pm 6.59 \times 10^{-06}$	7.75×10^{-04}	$\pm 3.84 \times 10^{-04}$
Q16	3.61×10^{-05}	$\pm 6.87 \times 10^{-06}$	8.95×10^{-04}	$\pm 3.66 \times 10^{-04}$
R7	5.77×10^{-05}	$\pm 5.17 \times 10^{-06}$	2.48×10^{-04}	$\pm 2.93 \times 10^{-04}$
R9	4.07×10^{-05}	$\pm 5.67 \times 10^{-06}$	8.03×10^{-04}	$\pm 3.11 \times 10^{-04}$

dissertation [19] [21] [22], plotted the same trend for the A band of oxygen¹⁰. This experiment documents for the first time a rotational dependence on the Lorentzian lineshape for an electric-quadrupole transition. These results are consistent with the known theory that rotationally-inelastic collisions are the dominant mechanism in molecular pressure broadening [19] [21] [22].

¹⁰The A band refers to the $A^3\Sigma_u^+ \leftarrow X^3\Sigma_g^-$ transition in oxygen. This transition is governed by the electric dipole moment.

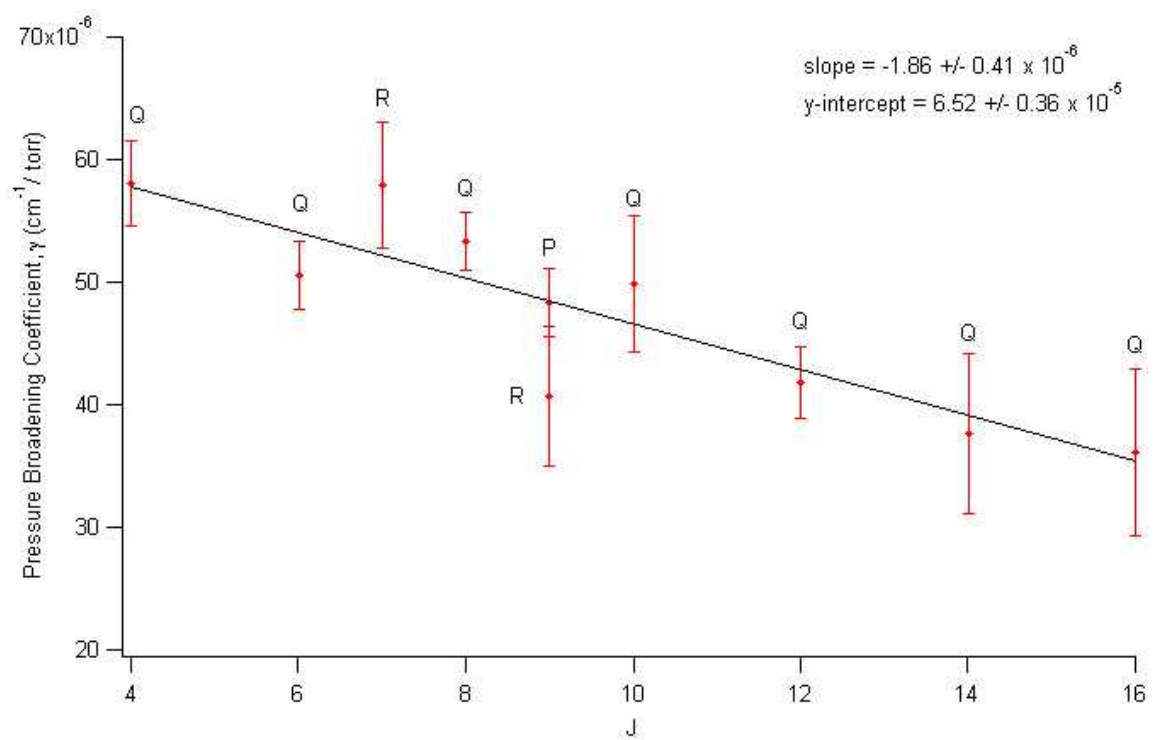


Figure 4.8: Rotational dependence on the pressure broadening coefficients.

V. Summary and Recommendations

All of the main research goals were achieved through the course of this experiment. The results presented in Chapter IV were acquired and compared to theory with great success and accuracy. In addition to this, the results also establish off-axis ICOS as a proven spectroscopic technique to observe ultra-weak transitions, such as those exclusively dependent on the electric-quadrupole moment. In this experiment, twenty-one lines were found, their integrated absorption cross sections were verified, and ten lines were pressure broadened with helium. Time did not allow, however, the ability to pressure broaden the ten lines with other noble gases, such as Ne, Ar, Kr or Xe. This chapter will provide a short summary of the results and then provide recommendations that will aid in the continuation of this or related research.

5.1 Summary

The results of Chapter IV verifies the sensitivity of the spectroscopic method used in this experiment to locate the $b^1\Sigma_g^+ \leftarrow a^1\Delta_g(1,0)$ band energies. Absolute line positions were determined to within 0.004cm^{-1} . The measured absolute line positions of the twenty-one lines differed from their predicted values by about 0.005cm^{-1} , which is on the order of the 1σ error from the wavemeter (See Table 4.1). The degree of accuracy achieved in this research effort may result in a slight correction to existing known spectroscopic constants for the $O_2(a)$ and $O_2(b)$ term energies, in addition to calculating the spectroscopic constants for the $b^1\Sigma_g^+ \leftarrow a^1\Delta_g(1,0)$ band itself, which has not been done before. The accuracy of these line positions may also benefit the HITRAN database¹.

The rotational temperature of $314 \pm 7\text{K}$, derived from a Boltzmann analysis of the 21 detected lines, was also found to be consistent with the integrated absorption cross sections calculated by Williams *et al.* This rotational temperature also compares nicely with similarly published results. Williams *et al* calculated $312 \pm 14\text{K}$ for the

¹This database catalogs all known absorption lines of the atmosphere and is maintained by MIT.

same band, and Fink *et al* calculated $313 \pm 10K$ for the emission of the $b^1\Sigma_g^+ \rightarrow a^1\Delta_g$ (0,0) band [6] [24].

Pressure broadening coefficients for ten lines were obtained ranging from $\gamma_p = 3.61 \times 10^{-6} cm^{-1}/torr$ to $5.81 \times 10^{-6} cm^{-1}/torr$. These coefficients are simply the slope of a regression line through the data set for each particular line. Since these specific lines had not been pressure broadened before, there were no published values to compare these results to. The values for the coefficients were reasonable and decreased as the rotational quantum number increased from J=4 to J=16. This particular property of pressure broadening has been observed and reported for other transitions [26] [19] [21] [22]. Being able to graph this trend was the only method used to determine if the coefficients collected in this experiment were indeed reasonable. Duplicating the pressure broadening analysis done in this research effort will be necessary in solidifying the results found.

In terms of applications, this research effort clearly proved the ability of off-axis ICOS to detect singlet delta oxygen, which is of great concern to the COIL community. From it's inception in the 70's to present-day technology, there has not been a method yet to detect the concentration of $O_2(a)$ generated from the SOG of a COIL. This apparatus works so well that the Chemical Branch at Kirtland AFB has just acquired a system similar to the apparatus used in this research effort. The spectroscopic data documented in this thesis should be a great foundation for their research and integration efforts with the COIL.

The atmospheric community will most benefit from the pressure broadening analysis. The coefficients derived in this study should aid in the understanding of the radiation transfer of the upper atmosphere. Now that the Lorentzian widths can be determined at any pressure (in torr), these coefficients will provide a better model for absorption processes which take place in the upper atmosphere.

5.2 *Recommendations For Further Research*

There are areas of this experiment that have the ability to be either expanded upon or added to for the purpose of creating a new thesis research topic. Some of those potential topics are presented below.

One idea is to acquire an RF discharge to generate the plasma instead of the microwave discharge that was used. This may be worth exploring for the purpose of increasing the yield of $O_2(a)$. It was mentioned in previous sections that Williams et.al. [24] obtained conversion efficiencies of 5%, which was double of what was generated in this experiment. Part of the reason may have been the higher ringdown time, but another reason could be the RF discharge that they used. With higher yields, some of the more weaker lines may become strong enough to analyze and report on.

Another topic involves the area of pressure broadening. This area was only slightly explored in this experiment since time only allowed for the use of He. In fact, some lines pressure broadened in this experiment by He were only scanned four or eight times, whereas the Q(8) line was scanned sixteen times. Therefore, better survey data could be taken of all the lines in this experiment using helium.

Another option would be to use the off-axis ICOS apparatus to analyze a completely different ultra-weak transition besides the Noxon Band. This will require the ordering of new tunable diode lasers, gases and mirrors that will reflect the new desired frequency range of interest. If new mirrors are ordered, then funds on the order of \$10,000 must be considered since each mirror costs approximately \$5,000.

Appendix A. Mathematical Development of GA

A.1 Beers Law to Off-Axis ICOS Theory

According to Beers Law, the output intensity with an absorbing species present ($I(\alpha L)$) is related to the incident laser intensity (I_0) through the following equation,

$$I(\alpha L) = I_0 e^{-\alpha L} \quad (\text{A.1})$$

where α is the absorption coefficient of the molecular absorber ($\alpha = \sigma(N_0 - N_1)$), and L is the length of the main cavity. For a single pass in the main cavity, the transmittancy of the mirrors need to be accounted for.

$$I(\alpha L) = I_0 T^2 e^{-\alpha L} \quad (\text{A.2})$$

Where T is the transmission coefficient for each mirror (in our case the mirrors are identical). However, since the $b^1\Sigma_g^+ \leftarrow a^1\Delta_g$ system is such a weak transition, it would be advantageous to increase the output intensity. One way to do this is to design a multi-pass off-axis cavity. The benefit is more apparent through the development of the following equations. Equation (A.2) is the relation for light simply traveling through the cavity. If the light were to reflect off both mirrors (also known as one roundtrip) before leaving the cavity, then it would have traveled three times the length of the cavity. This is expressed in the following relation,

$$I(\alpha L) = I_0 T^2 R^2 e^{-3\alpha L} \quad (\text{A.3})$$

where R is the reflectivity of the mirrors. If the light were to complete yet another roundtrip,

$$I(\alpha L) = I_0 T^2 R^4 e^{-5\alpha L} \quad (\text{A.4})$$

The pattern now becomes distinguishable enough to rewrite the expression as a summation,

$$I(\alpha L) = I_0 T^2 e^{-\alpha L} \sum_n (R e^{-\alpha L})^{2n} \quad (\text{A.5})$$

If the number of passes, n , is many orders of magnitude greater than the length of the cavity, L , then equation (A.5) can be approximated in the infinite limit by an integral.

$$I(\alpha L) = I_0 T^2 e^{-\alpha L} \int_0^\infty (R e^{-\alpha L})^{2n} \text{d}n \quad (\text{A.6})$$

One way to reach the gain factor G is to continue this development by solving for the above integral. Although that would be the simpler way to reach G , the form would be too complicated to understand physically (see equation (A.7)).

$$G = -\frac{1}{2 \ln(R e^{-\alpha L})} \quad (\text{A.7})$$

Therefore, what needs to be done is to continue down a more complicated and rigorous road in order to find the simpler and easy-to-visualize form of G ¹. This is done by solving directly for the summation in (A.5). Solving gives,

$$I(\alpha L) = I_0 T^2 \frac{e^{-\alpha L}}{(1 - R e^{-2\alpha L})} \quad (\text{A.8})$$

Which can be re-written as,

$$I(\alpha L) = I_0 T^2 \frac{e^{-\alpha L}}{(1 - R e^{-\alpha L})(1 + R e^{-\alpha L})} \quad (\text{A.9})$$

Now we need to include another intensity which is important to multi-pass absorption spectroscopy, which is the output intensity without the absorbing species present

¹These series of steps was carried out by Dr. Skip Williams

$[I(\alpha L = 0)]$. The next step shows the beauty of obtaining the absorption spectra through direct attenuation methods. If the following relation is written,

$$\frac{I(\alpha L = 0)}{I(\alpha L)} - 1 \quad (\text{A.10})$$

then this gives the direct measurement of the absorbing signal is achieved. Consider for the moment some fictitious numbers. Let $I(\alpha L = 0) = 5$ (the intensity of the output intensity without the absorbing species) and $I(\alpha L) = 4.9999$ (the output intensity with the very weak absorbing species). If these numbers are applied to (A.10), then the result is the intensity of the absorbing feature, in this case 2×10^{-5} . Now, if equation (A.9) is applied to equation (A.10), then we have,

$$\frac{I(\alpha L = 0)}{I(\alpha L)} - 1 = \frac{\frac{I_0 T^2}{(1-R)(1+R)}}{\frac{I_0 T^2 e^{-\alpha L}}{(1-Re^{-\alpha L})(1+Re^{-\alpha L})}} - 1 \quad (\text{A.11})$$

$$\frac{I(\alpha L = 0)}{I(\alpha L)} - 1 = \frac{(1 - Re^{-\alpha L})(1 + Re^{-\alpha L})}{(1 - R)(1 + R)e^{-\alpha L}} - 1 \quad (\text{A.12})$$

Using the following relations,

$$(1 - R \exp(-\alpha L)) = (1 - R) \left[1 + \frac{R(1 - e^{-\alpha L})}{(1 - R)} \right] \quad (\text{A.13})$$

$$(1 + R \exp(-\alpha L)) = (1 + R) \left[1 - \frac{R(1 - e^{-\alpha L})}{(1 - R)} \right] \quad (\text{A.14})$$

Now substitute (A.13) and (A.14) into (A.12) to obtain,

$$\frac{I(\alpha L = 0)}{I(\alpha L)} - 1 = \frac{\left[1 + \frac{R(1 - e^{-\alpha L})}{(1 - R)} \right] \left[1 - \frac{R(1 - e^{-\alpha L})}{(1 - R)} \right]}{e^{-\alpha L}} - 1 \quad (\text{A.15})$$

A term which is known as the single-pass absorption can now be defined as $A = (1 - e^{-\alpha L})$. This description is more readily apparent when a series expansion is

performed on the exponential yielding a first approximation, $A \approx \alpha L$. Therefore,

$$\frac{I(\alpha L = 0)}{I(\alpha L)} - 1 = \frac{\left[1 + \frac{R}{(1-R)}A\right] \left[1 - \frac{R}{(1-R)}A\right]}{e^{-\alpha L}} - 1 \quad (\text{A.16})$$

The next three steps are simply algebraic manipulation.

$$\frac{I(\alpha L = 0)}{I(\alpha L)} - 1 = \frac{\left[1 + \frac{R}{(1-R)}A - \frac{R}{(1-R)}A - \left(\frac{R^2}{1-R^2}\right)A^2\right]}{e^{-\alpha L}} - 1 \quad (\text{A.17})$$

$$\frac{I(\alpha L = 0)}{I(\alpha L)} - 1 = \frac{\left[1 + A \left(\frac{R+R^2-R+R^2}{1-R^2}\right) - \left(\frac{R^2}{1-R^2}\right)A^2\right]}{e^{-\alpha L}} - 1 \quad (\text{A.18})$$

$$\frac{I(\alpha L = 0)}{I(\alpha L)} - 1 = \frac{\left[1 + 2A \left(\frac{R^2}{1-R^2}\right) - \left(\frac{R^2}{1-R^2}\right)A^2\right]}{e^{-\alpha L}} - 1 \quad (\text{A.19})$$

The following step combines the quantity 1 on the right-hand side by using the common denominator. This is done by using the relation $1 = \frac{e^{-\alpha L}}{e^{-\alpha L}}$.

$$\frac{I(\alpha L = 0)}{I(\alpha L)} - 1 = \frac{(1 - e^{-\alpha L}) + 2A \left(\frac{R^2}{1-R^2}\right) - \left(\frac{R^2}{1-R^2}\right)A^2}{e^{-\alpha L}} \quad (\text{A.20})$$

After combining the 1, another $A = (1 - e^{-\alpha L})$ term appears. Making this substitution and extracting the common $e^{\alpha L}$ from the right-hand side gives,

$$\frac{I(\alpha L = 0)}{I(\alpha L)} - 1 = e^{\alpha L} \left[A + 2A \left(\frac{R^2}{1-R^2}\right) - A^2 \left(\frac{R^2}{1-R^2}\right) \right] \quad (\text{A.21})$$

The cavity enhancement factor is now defined as,

$$G = \left(\frac{2R^2}{1-R^2} \right) \quad (\text{A.22})$$

Obviously, equation A.22 is a lot more physically comprehensible than equation A.7 above. Equation A.22 shows explicitly how important the reflectivity of the mirrors are. The closer R approaches 100%, the larger G becomes. Recall that this experiment uses mirrors with reflectivities of greater than 99.997%. (An average value for G in this experiment was 80,000. This yields reflectivities of $R = 99.9988\%$.) Substituting this value of G gives,

$$\frac{I(\alpha L = 0)}{I(\alpha L)} - 1 = e^{\alpha L} \left[A + AG - \frac{A^2 G}{2} \right] \quad (\text{A.23})$$

Multiplying through by $e^{\alpha L}$ and pulling out a factor of GA yields,

$$\frac{I(\alpha L = 0)}{I(\alpha L)} - 1 = GA \left[\frac{e^{\alpha L}}{G} + e^{\alpha L} - \frac{e^{\alpha L} A}{2} \right] = GA \left[\frac{e^{\alpha L}}{G} + e^{\alpha L} - \frac{e^{\alpha L} (1 - e^{-\alpha L})}{2} \right] \quad (\text{A.24})$$

Now if we expand out $\frac{e^{\alpha L} (1 - e^{-\alpha L})}{2}$ and combine terms, we end up with

$$\frac{I(\alpha L = 0)}{I(\alpha L)} - 1 = GA \left[\frac{1}{2} + \frac{e^{\alpha L}}{2} + \frac{e^{\alpha L}}{G} \right] \quad (\text{A.25})$$

The next step in this development brings light as to why this particular technique (multi-pass absorption spectroscopy) really only works for very weak species. Since the absorption cross section is so small (10^{-24}) then $e^{\alpha L} \rightarrow 1$. Also, because we know that G will be high (80,000) then $\frac{e^{\alpha L}}{G} \rightarrow 0$. Therefore we are left with the following.

$$\frac{I(\alpha L = 0)}{I(\alpha L)} - 1 = GA \quad (\text{A.26})$$

This is actually the form used inside the macro file of the program used for the data analysis (IGOR Pro). This step was already explained in the Procedure section in Chapter III.

Equation (A.26) is still not the common form used in ICOS theory. What is now required is a bit of mathematical messaging. Multiplying through by $I(\alpha L)$ in

equation (A.26) gives,

$$I(\alpha L = 0) - I(\alpha L) = GA I(\alpha L) \quad (\text{A.27})$$

Next, we need to add the quantity $GA I(\alpha L = 0)$ to both sides.

$$I(\alpha L = 0) - I(\alpha L) + GA I(\alpha L = 0) = GA I(\alpha L) + GA I(\alpha L = 0) \quad (\text{A.28})$$

Now, subtract both sides by $GA I(\alpha L)$,

$$I(\alpha L = 0) - I(\alpha L) + GA I(\alpha L = 0) - GA I(\alpha L) = GA I(\alpha L = 0) \quad (\text{A.29})$$

Simplifying the left-hand side,

$$(1 + GA)[I(\alpha L = 0) - I(\alpha L)] = GA I(\alpha L = 0) \quad (\text{A.30})$$

Next rearrange the terms, so that the two GA terms are on the right-hand side.

$$\frac{I(\alpha L = 0) - I(\alpha L)}{I(\alpha L = 0)} = \frac{GA}{1 + GA} \quad (\text{A.31})$$

If we define the change in the steady-state cavity output as $\Delta I = I(\alpha L = 0) - I(\alpha L)$, then we have the following usable form that is the basis for ICOS theory.

$$\frac{\Delta I}{I(\alpha L = 0)} = \frac{GA}{1 + GA} \quad (\text{A.32})$$

After further analysis of this relation, it becomes clear that the multi-pass method increases the intensity of the original absorption output signal by a significant amount. As mentioned in Section 3.1.2, equation A.32 says that the absorption information (A) is contained within the change in steady-state output of the cavity. This allows for a direct measurement of the absorption feature [16]. For weak absorption ($GA \gg 1$), the cavity provides a linear absorption signal gain. Physically, G refers to

the number of optical passes that occur within the cavity decay time ($G \approx \frac{\tau c}{L}$) and is also simply related to the cavity finesse ($G \approx \frac{F}{\pi}$) [12].

Appendix B. Term and Band Energies

MATLAB[®]

The following code calculates the term energies for the $b^1\Sigma_g^+ \leftarrow X^3\Sigma_g^-$ (1,0) and the $a^1\Delta_g \leftarrow X^3\Sigma_g^-$ (0,0) transitions. The $b^1\Sigma_g^+ \leftarrow a^1\Delta_g$ (1,0) band is then found by subtracting the appropriate term energies. Lists for $\mathbf{J} = 1 - 20$ are generated for each of these scenarios. The Hamiltonian and spectroscopic constants used in this experiment are those found by Cheah and Lee [27].

B.1 Matlab Code

Listing B.1: The following is the Matlab[®] file used in the thesis.
([Appendix4/cheahtermband2.m](#))

```
1 function []= cheahtermband
%This program will generate term energies for
%a(v=0) and b(v=1). The line positions for the five branches
%are then calculated for the b-a (0,1) band.

6
%Spectroscopic constants according to Cheah and Lee 2000
v0a=7888.107842;
B0a=1.41780381;
D0a=5.11144e-6;
11 Del=2;

v0b=13120.918775;
B0b=1.39124421;
D0b=5.3641e-6;
16 Sig=0;

v1b=14525.65553;
B1b=1.3729659;
D1b=5.4086e-6;
21
fprintf('\nTerm energies for 02(a), v=0, in wavenumbers.\n');

%Generates the energies in wavenumbers for 02(a), v=0
for Ja=2:20
26 Fa(Ja)=v0a + B0a*(Ja*(Ja + 1) - Del^2) - D0a*(Ja*(Ja +1) - ...
Del^2)^2;
fprintf('(J=%1.0f)= %9.9e \n',Ja,Fa(Ja));
end

fprintf('\nTerm energies for 02(b), v=1, in wavenumbers.\n');
31
%Generates the energies in wavenumbers for 02(b), v=1
for Jb=2:2:20
```



```

        Fb1(Jb)=v1b + B1b*(Jb*(Jb + 1) - Sig^2) - D1b*(Jb*(Jb +1) - ...
            Sig^2)^2;
        fprintf('(J=%1.0f)= %9.9e \n',Jb,Fb1(Jb));
36 end

        fprintf('\nThe following line positions are for the b-a (1,0) band...
            in wavenumbers\n');

    for Ja=2:20
41     for Jb=2:2:20
            if Jb-Ja==-2
                O(Ja)=Fb1(Jb)-Fa(Ja);
                fprintf('O(%1.0f)= %9.9e \n',Ja,O(Ja));
            end
46     if Jb-Ja==-1
                P(Ja)=Fb1(Jb)-Fa(Ja);
                fprintf('P(%1.0f)= %9.9e \n',Ja,P(Ja));
            end
            if Jb-Ja==0
51     Q(Ja)=Fb1(Jb)-Fa(Ja);
                fprintf('Q(%1.0f)= %9.9e \n',Ja,Q(Ja));
            end
            if Jb-Ja==1
                R(Ja)=Fb1(Jb)-Fa(Ja);
56     fprintf('R(%1.0f)= %9.9e \n',Ja,R(Ja));
            end
            if Jb-Ja==2
                S(Ja)=Fb1(Jb)-Fa(Ja);
                fprintf('S(%1.0f)= %9.9e \n',Ja,S(Ja));
61     end
            end
    end
end

```

B.2 The Theoretical Term Energies

Term energies for $O_2(a)$, $v=0$ in wavenumbers.

(J=2)=7.890943429e+003
(J=3)= 7.899449945e+003
(J=4)=7.910791394e+003
(J=5)= 7.924967286e+003
(J=6)= 7.941977006e+003
(J=7)= 7.961819819e+003
(J=8)= 7.984494866e+003
(J=9)= 8.010001165e+003

(J=10)= 8.038337614e+003
(J=11)= 8.069502984e+003
(J=12)= 8.103495926e+003
(J=13)= 8.140314969e+003
(J=14)= 8.179958518e+003
(J=15)= 8.222424854e+003
(J=16)= 8.267712139e+003
(J=17)= 8.315818409e+003
(J=18)= 8.366741578e+003
(J=19)= 8.420479440e+003
(J=20)= 8.477029662e+003

Term energies for $O_2(b)$, $v=1$ in wavenumbers.

(J=2)=1.453389313e+004
(J=4)= 1.455311268e+004
(J=6)= 1.458331056e+004
(J=8)= 1.462448104e+004
(J=10)= 1.467661633e+004
(J=12)= 1.473970659e+004
(J=14)= 1.481373985e+004
(J=16)= 1.489870210e+004
(J=18)= 1.499457726e+004
(J=20)= 1.510134713e+004

B.3 The Predicted Band Energies

The following line positions are for the b-a(0,1) band in wavenumbers.

Q(2)= 6.642949702e+003
S(2)= 6.662169255e+003
P(3)= 6.634443185e+003
R(3)= 6.653662739e+003

$O(4)= 6.623101736e+003$
 $Q(4)= 6.642321290e+003$
 $S(4)= 6.672519163e+003$
 $P(5)= 6.628145399e+003$
 $R(5)= 6.658343271e+003$
 $O(6)= 6.611135679e+003$
 $Q(6)= 6.641333551e+003$
 $S(6)= 6.682504031e+003$
 $P(7)= 6.621490738e+003$
 $R(7)= 6.662661218e+003$
 $O(8)= 6.598815691e+003$
 $Q(8)= 6.639986171e+003$
 $S(8)= 6.692121469e+003$
 $P(9)= 6.614479871e+003$
 $R(9)= 6.666615169e+003$
 $O(10)= 6.586143423e+003$
 $Q(10)= 6.638278721e+003$
 $S(10)= 6.701368973e+003$
 $P(11)= 6.607113351e+003$
 $R(11)= 6.670203603e+003$
 $O(12)= 6.573120409e+003$
 $Q(12)= 6.636210660e+003$
 $S(12)= 6.710243923e+003$
 $P(13)= 6.599391617e+003$
 $R(13)= 6.673424880e+003$
 $O(14)= 6.559748069e+003$
 $Q(14)= 6.633781332e+003$
 $S(14)= 6.718743587e+003$
 $P(15)= 6.591314995e+003$

R(15)= 6.676277251e+003
O(16)= 6.546027711e+003
Q(16)= 6.630989966e+003
S(16)= 6.726865117e+003
P(17)= 6.582883696e+003
R(17)= 6.678758847e+003
O(18)= 6.531960527e+003
Q(18)= 6.627835678e+003
S(18)= 6.734605553e+003
P(19)= 6.574097817e+003
R(19)= 6.680867691e+003
O(20)= 6.517547595e+003
Q(20)= 6.624317469e+003

Appendix C. Analyzed Data

This appendix contains all of the 21 lines observed in this research effort. Please reference the left-axis (which describes the signal intensity) for each line, because these lines are not scaled relative to each other. Instead, each line has been zoomed in to fill the graph. These particular graphs were the one's used to measure the absolute line positions to within 0.004cm^{-1} . The helium and oxygen flow rates were 4000 sccm and 400 sccm respectively, and the average pressure within the optical cavity was 23 torr.

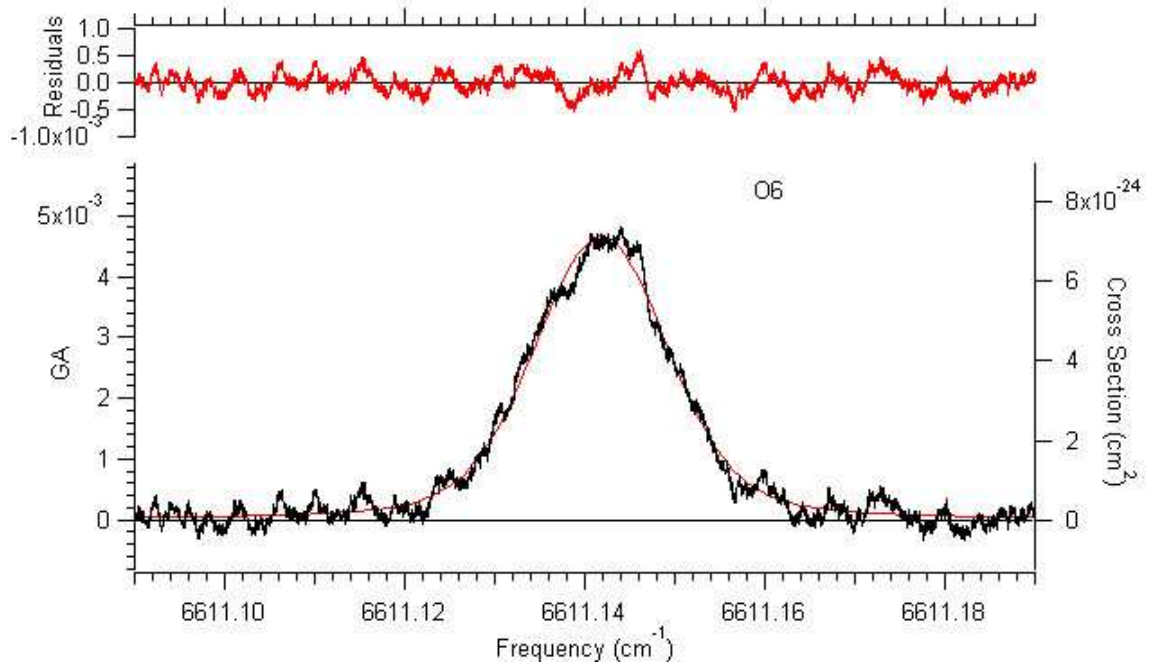


Figure C.1: The O(6) line position at 6611.1418cm^{-1} .

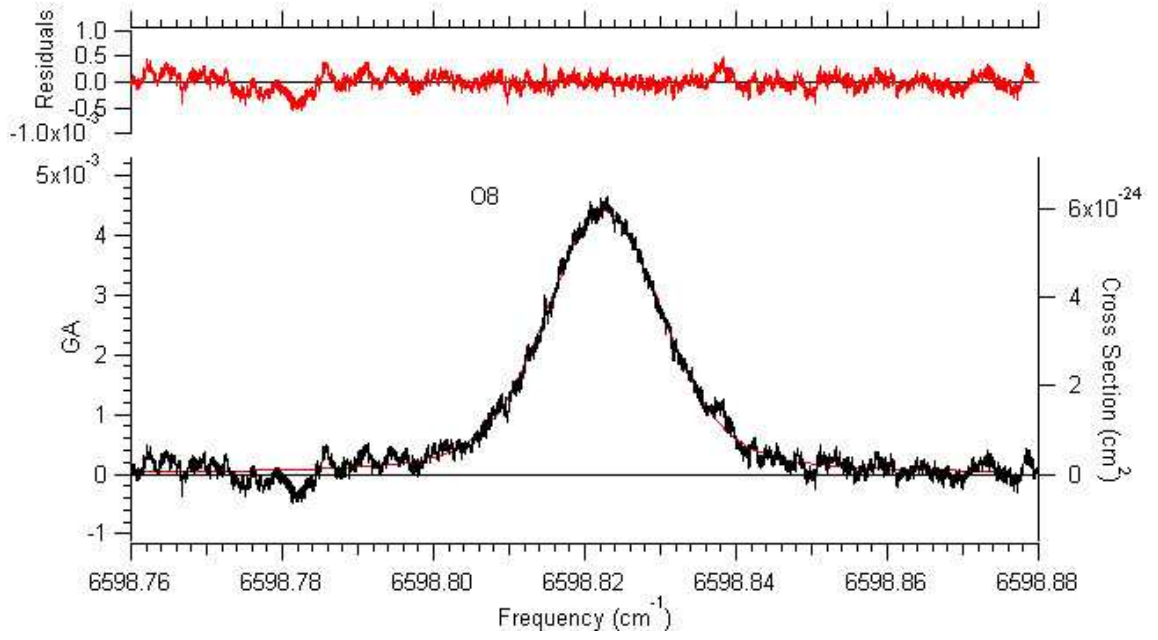


Figure C.2: The O(8) line position at 6598.8226cm^{-1} .

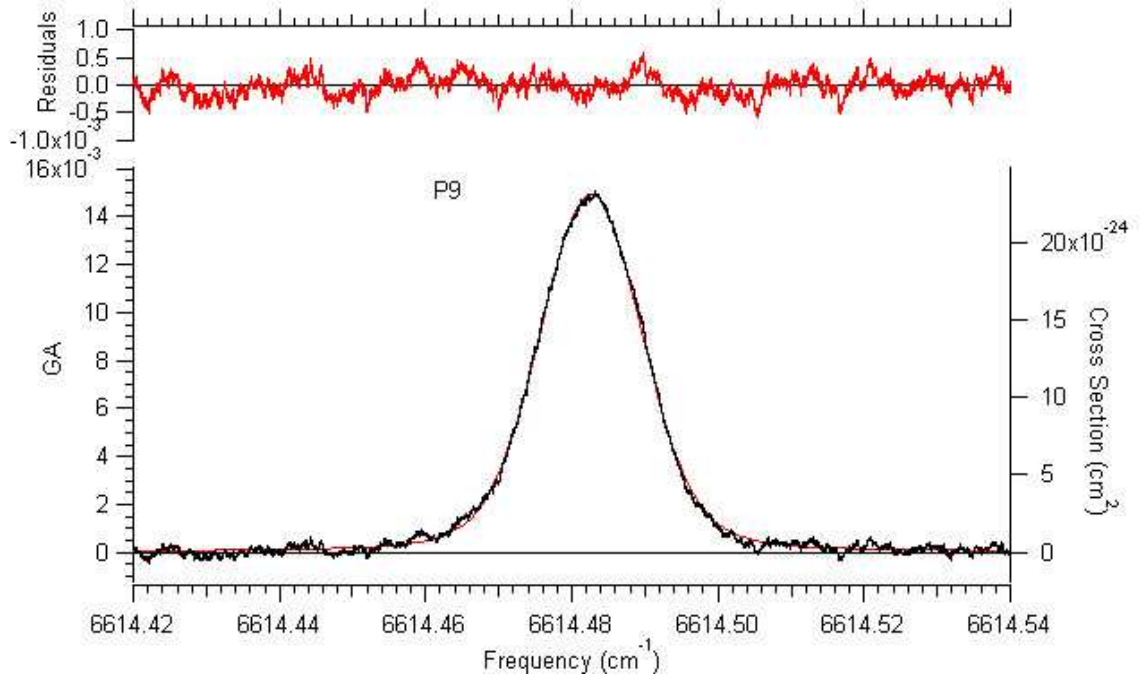


Figure C.3: The P(9) line position at 6614.4826cm^{-1} .

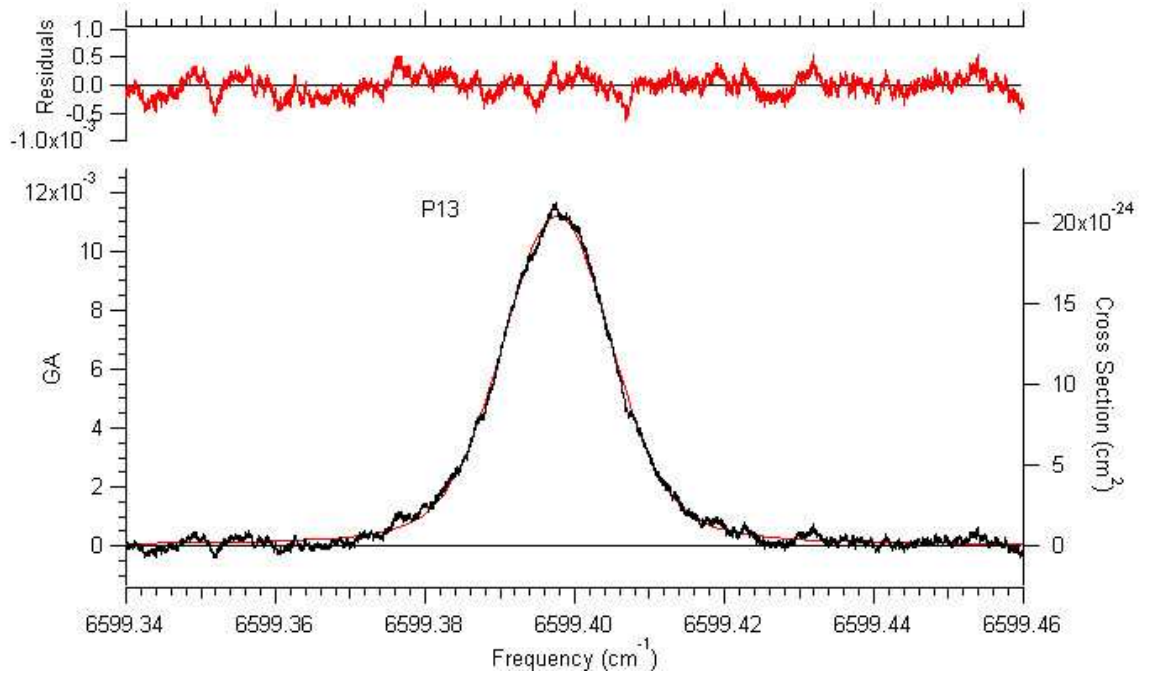


Figure C.4: The P(13) line position at 6599.3977cm^{-1} .

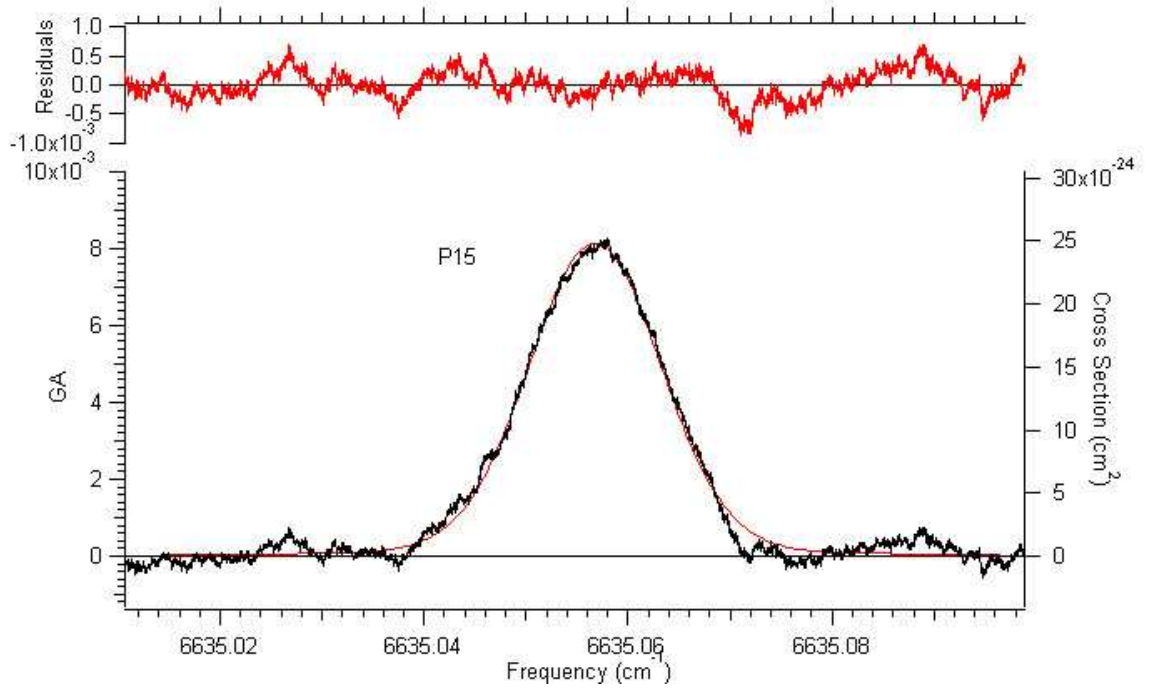


Figure C.5: The P(15) line position at 6591.3228cm^{-1} .

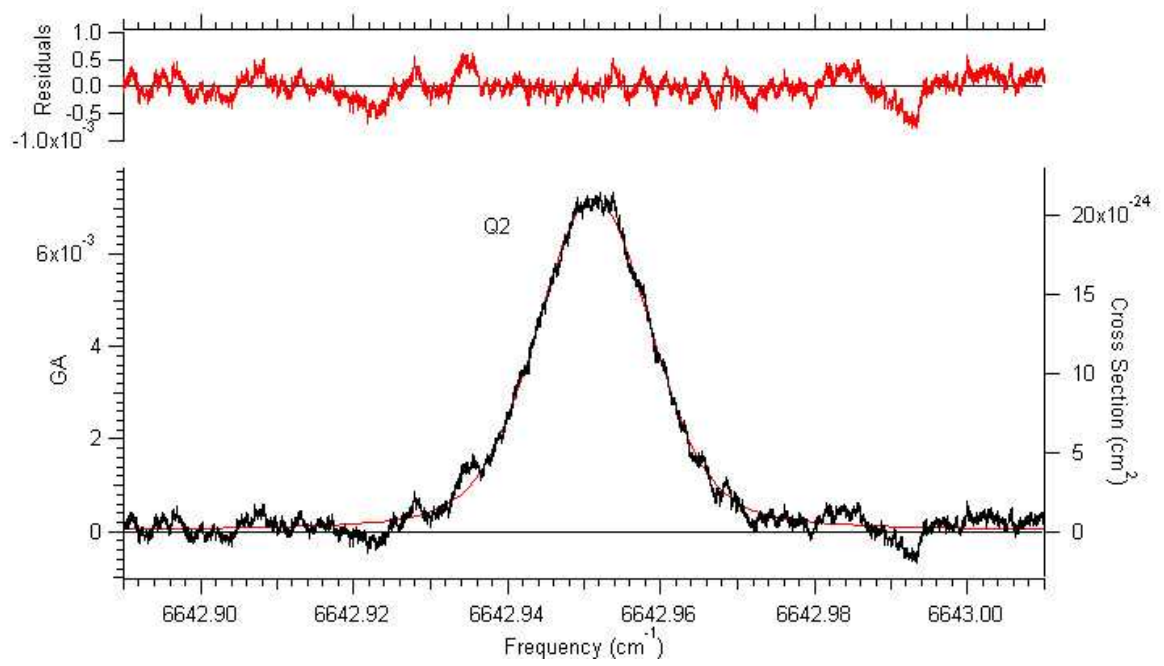


Figure C.6: The Q(2) line position at 6642.9513cm^{-1} .

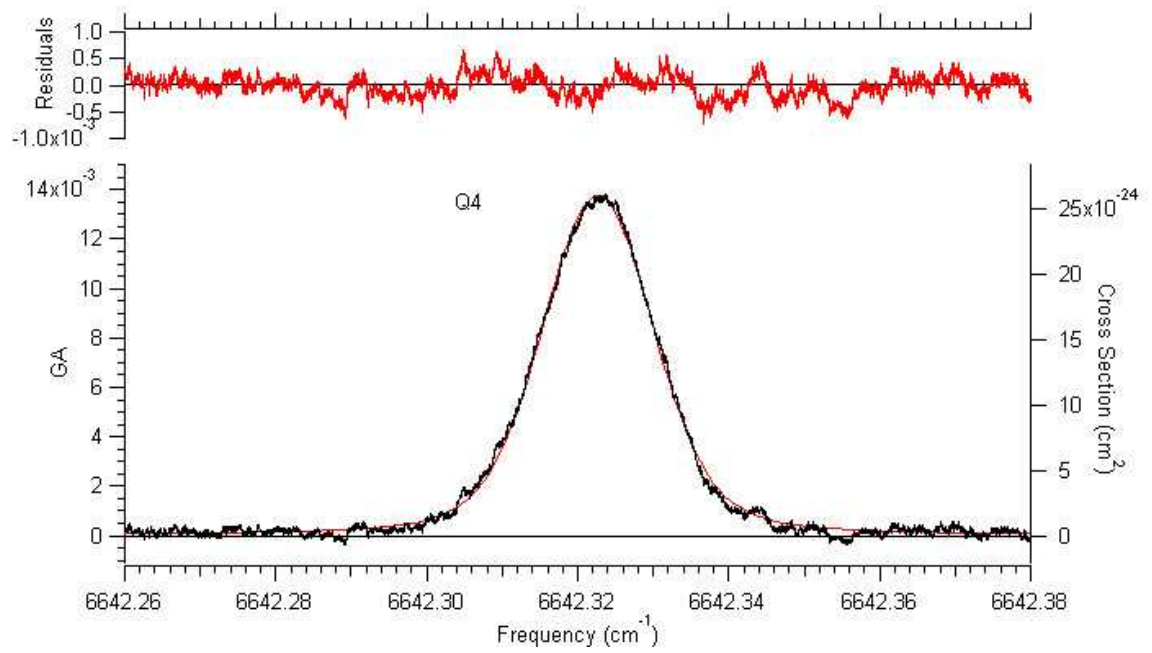


Figure C.7: The Q(4) line position at 6642.3227cm^{-1} .

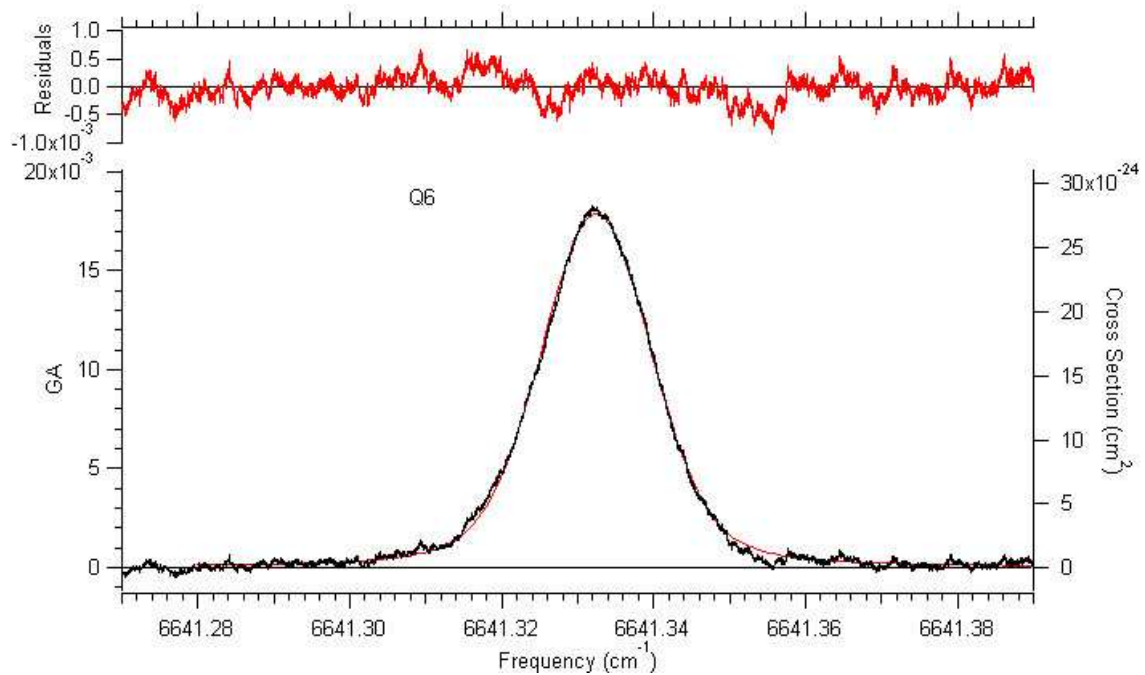


Figure C.8: The Q(6) line position at 6641.3324cm^{-1} .

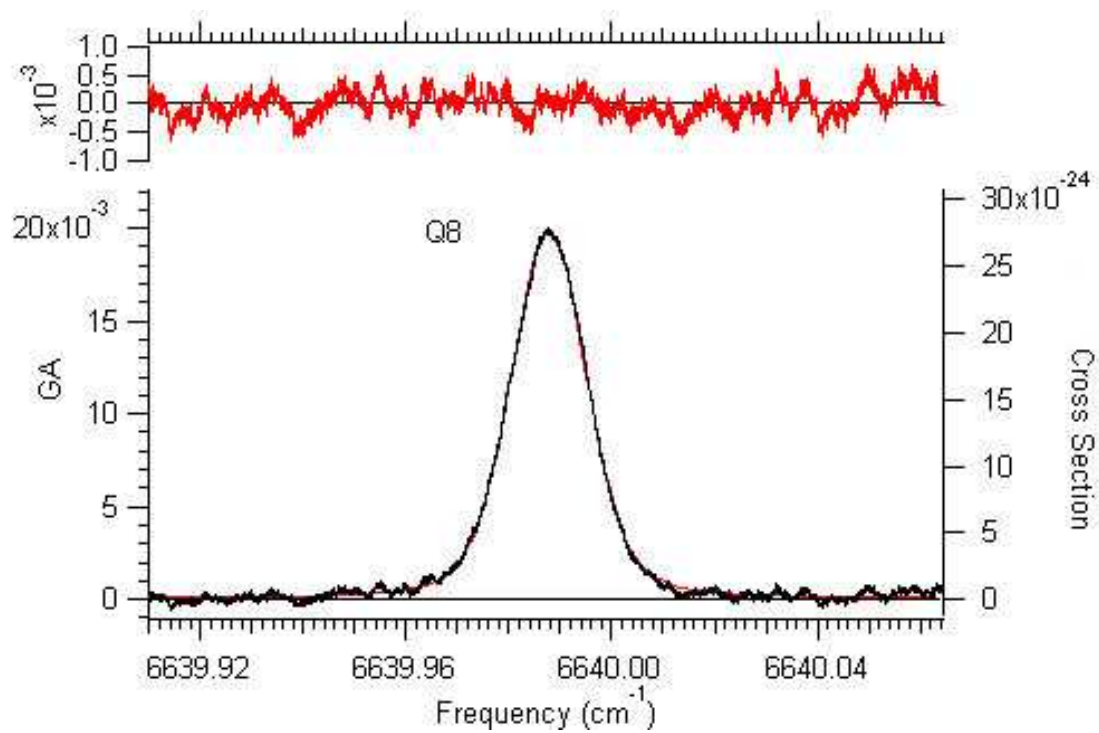


Figure C.9: The Q(8) line position at 6639.9878cm^{-1} .

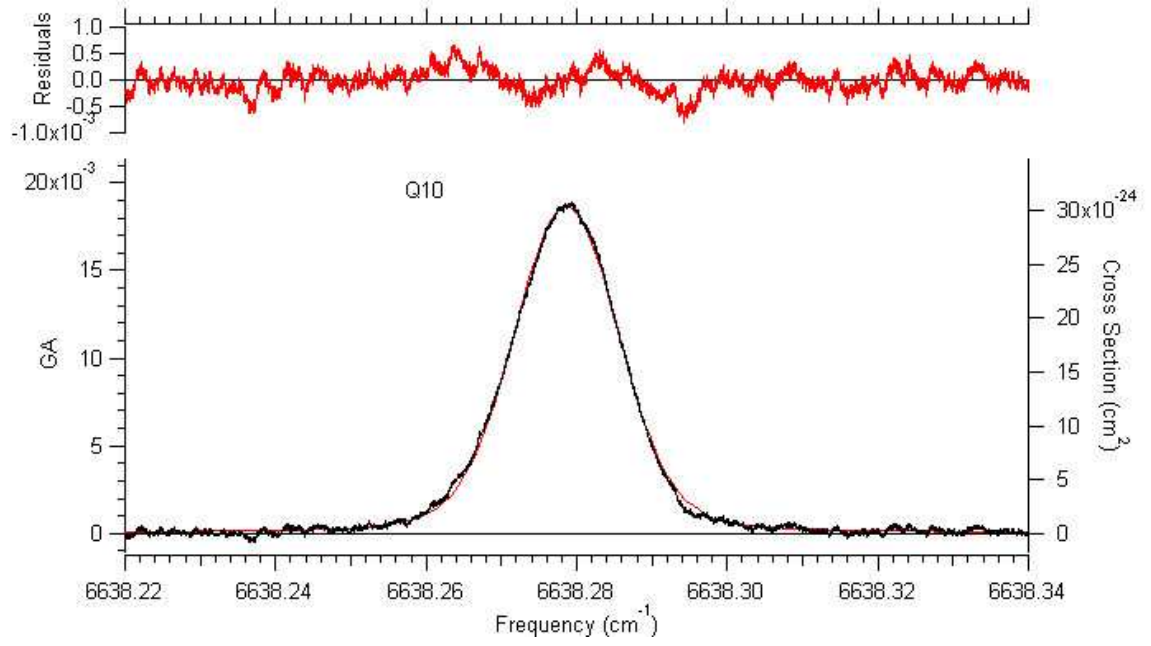


Figure C.10: The Q(10) line position at 6638.2786cm^{-1} .

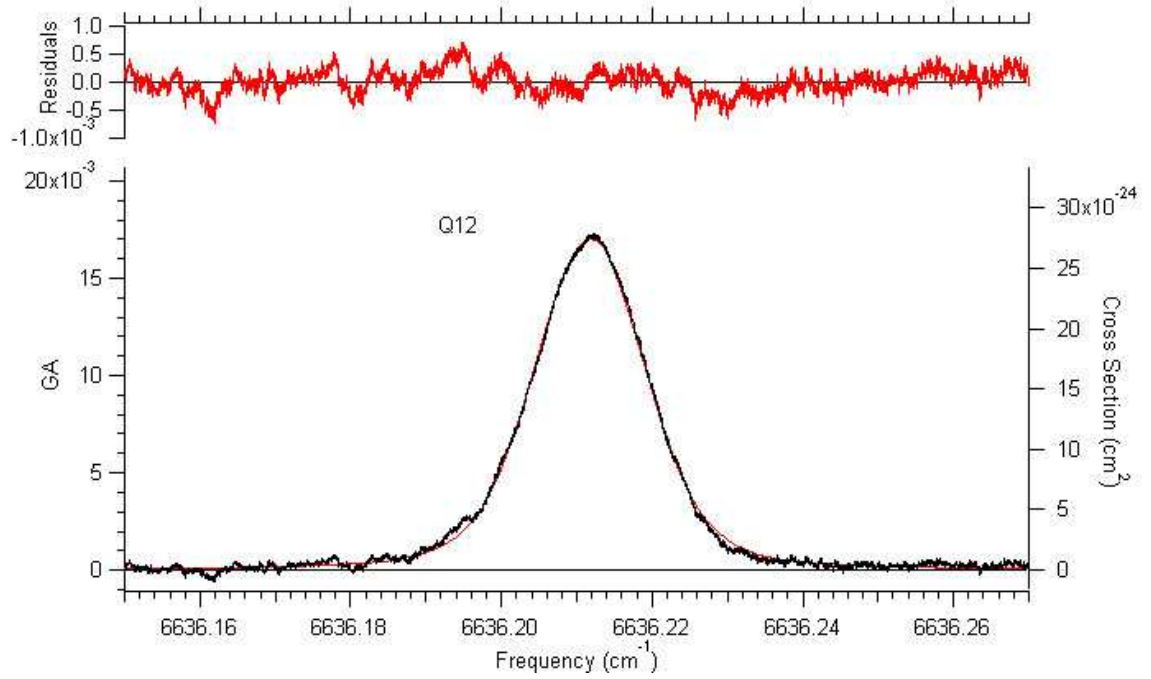


Figure C.11: The Q(12) line position at 6636.2118cm^{-1} .

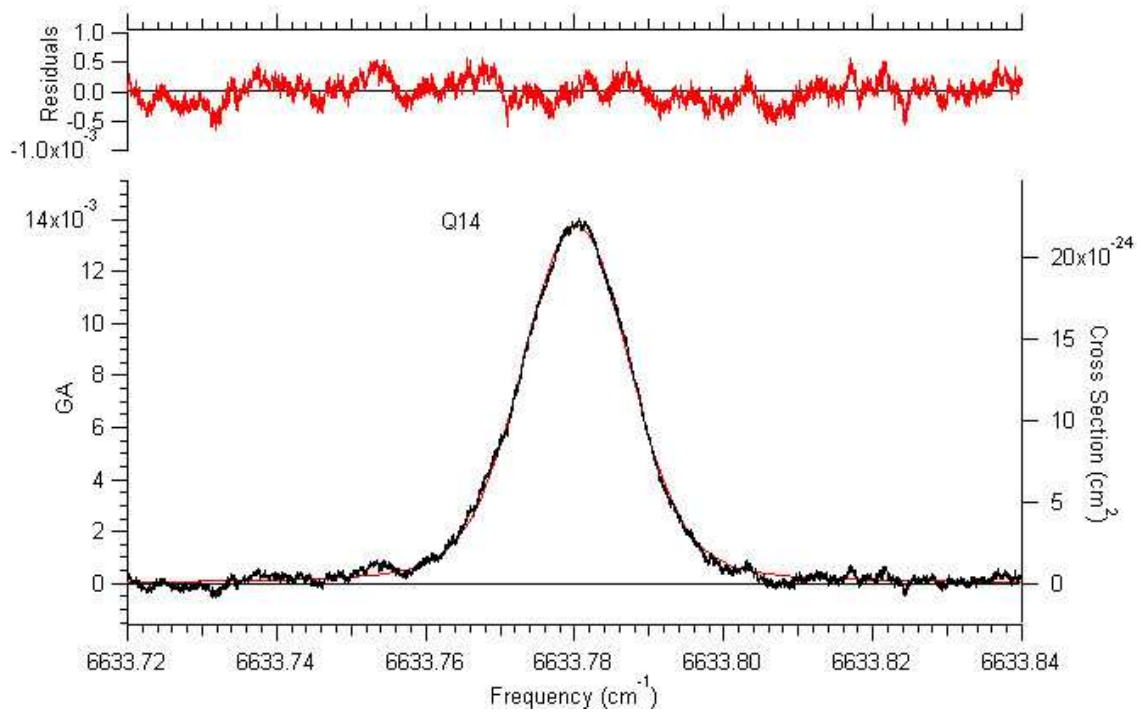


Figure C.12: The Q(14) line position at 6633.7802cm^{-1} .

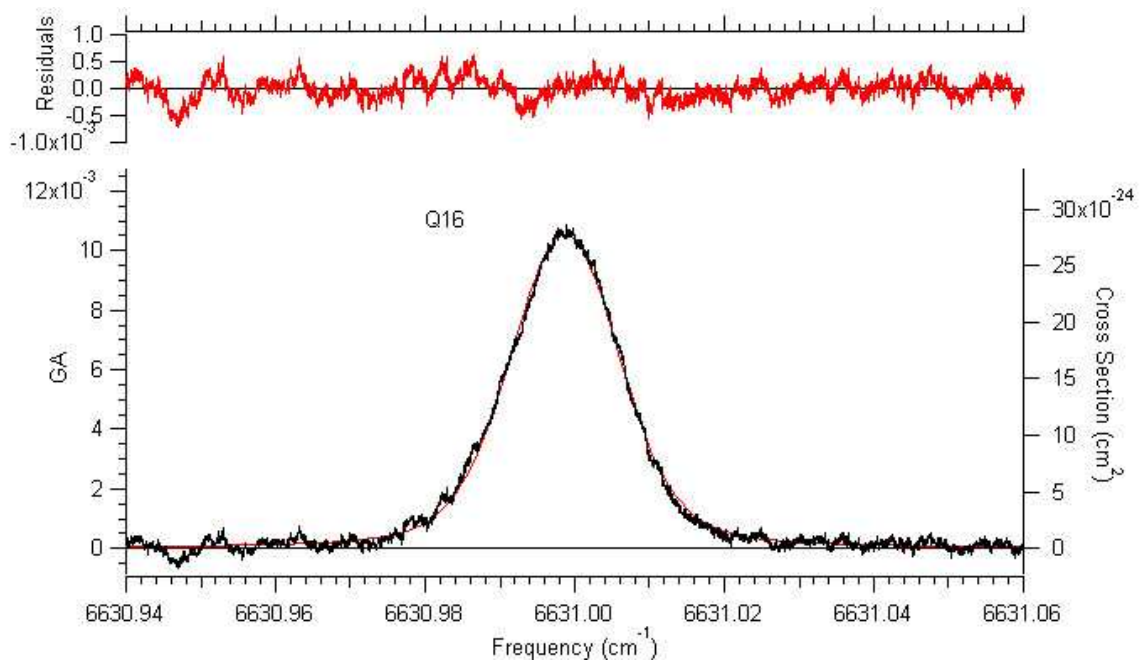


Figure C.13: The Q(16) line position at 6630.9987cm^{-1} .

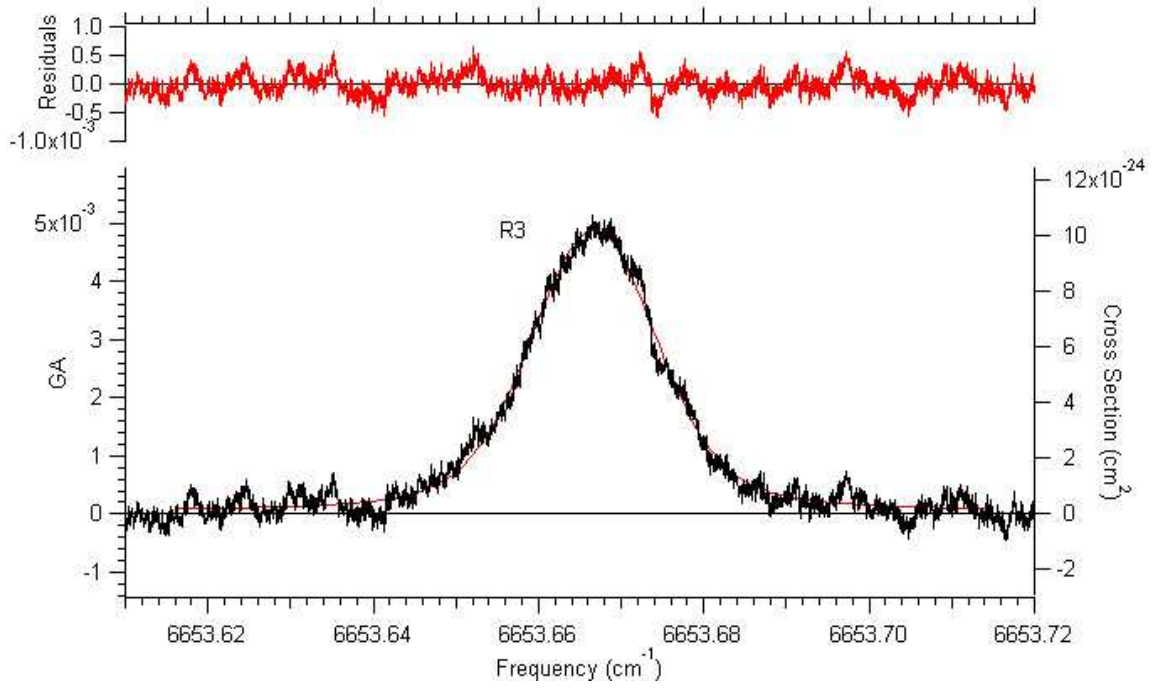


Figure C.14: The R(3) line position at 6653.6667cm^{-1} .

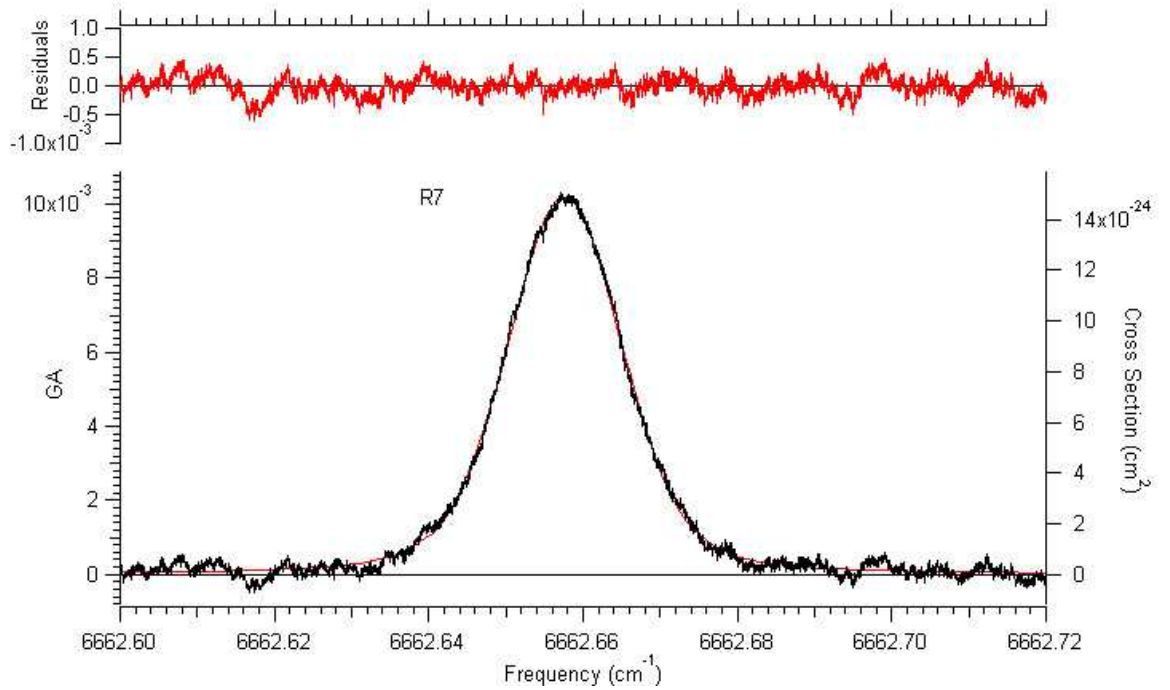


Figure C.15: The R(7) line position at 6662.6576cm^{-1} .

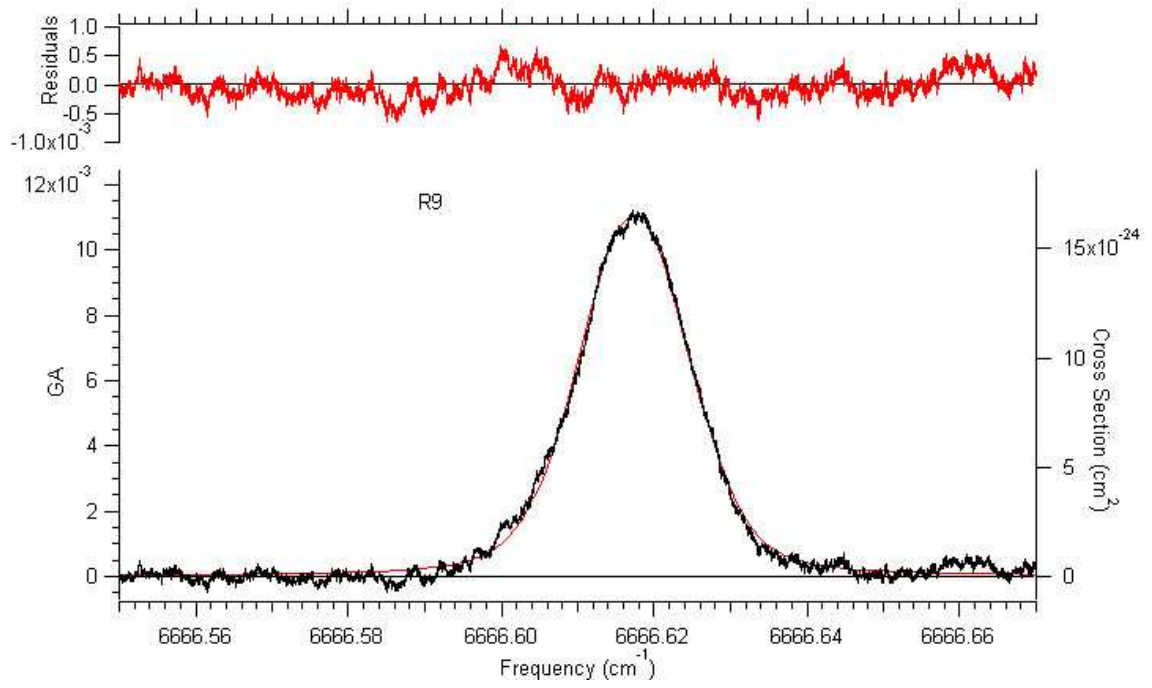


Figure C.16: The R(9) line position at 6666.6174cm^{-1} .

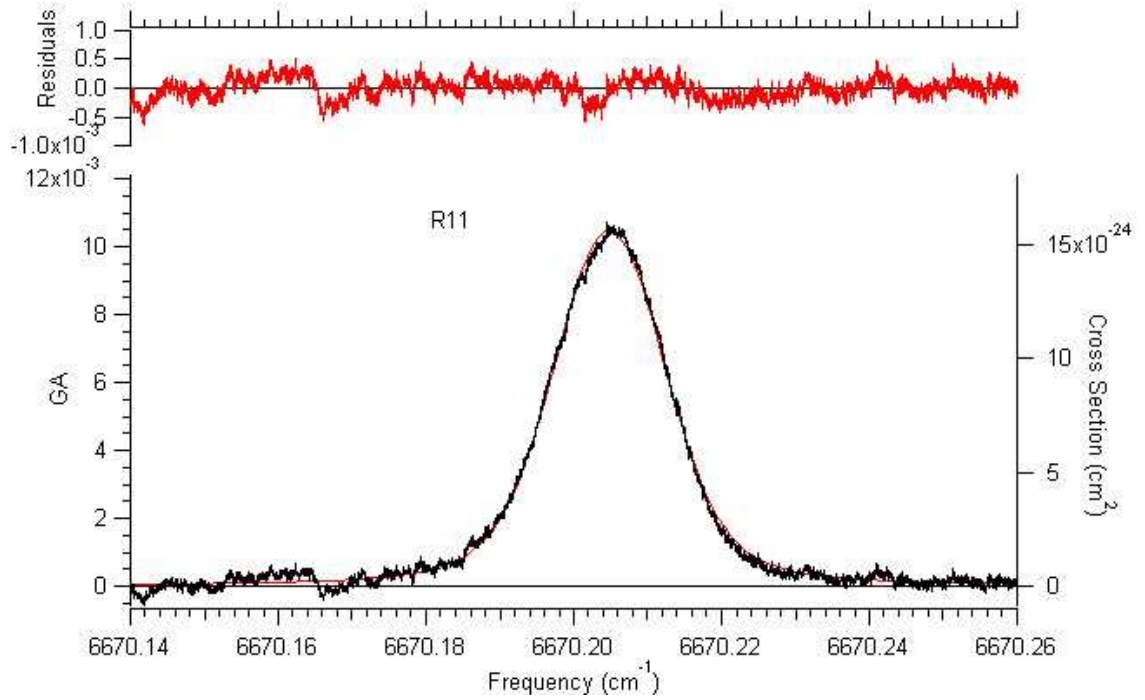


Figure C.17: The R(11) line position at 6670.2048cm^{-1} .

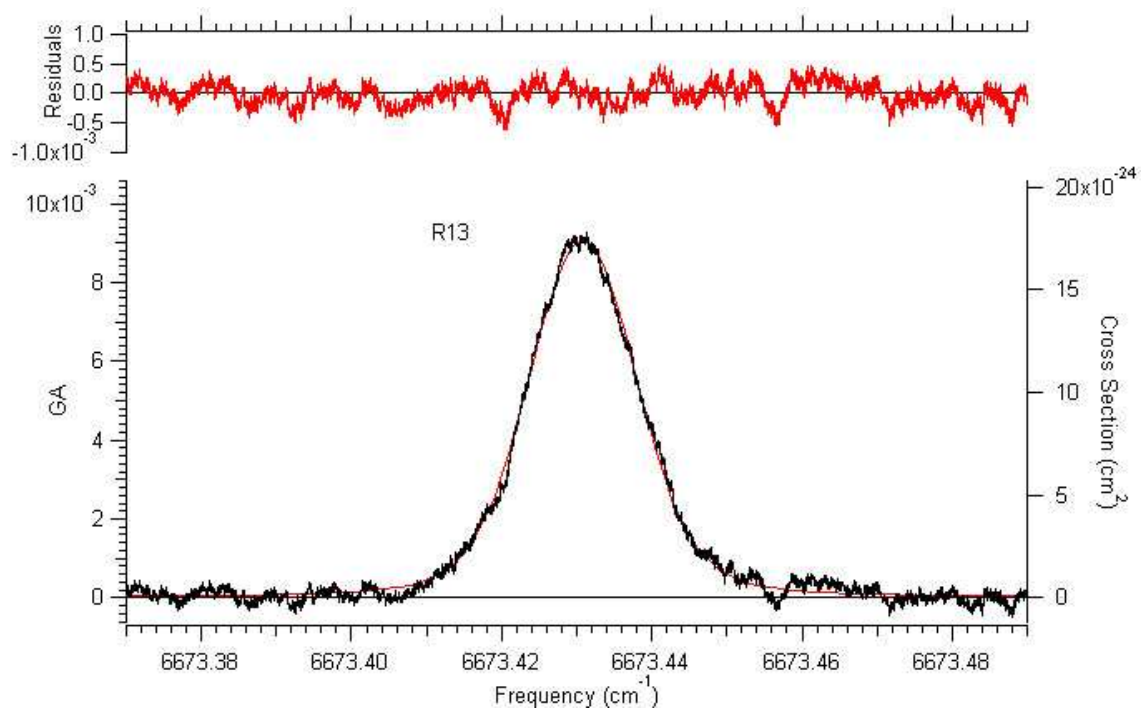


Figure C.18: The R(13) line position at $6673.4308 \text{ cm}^{-1}$.

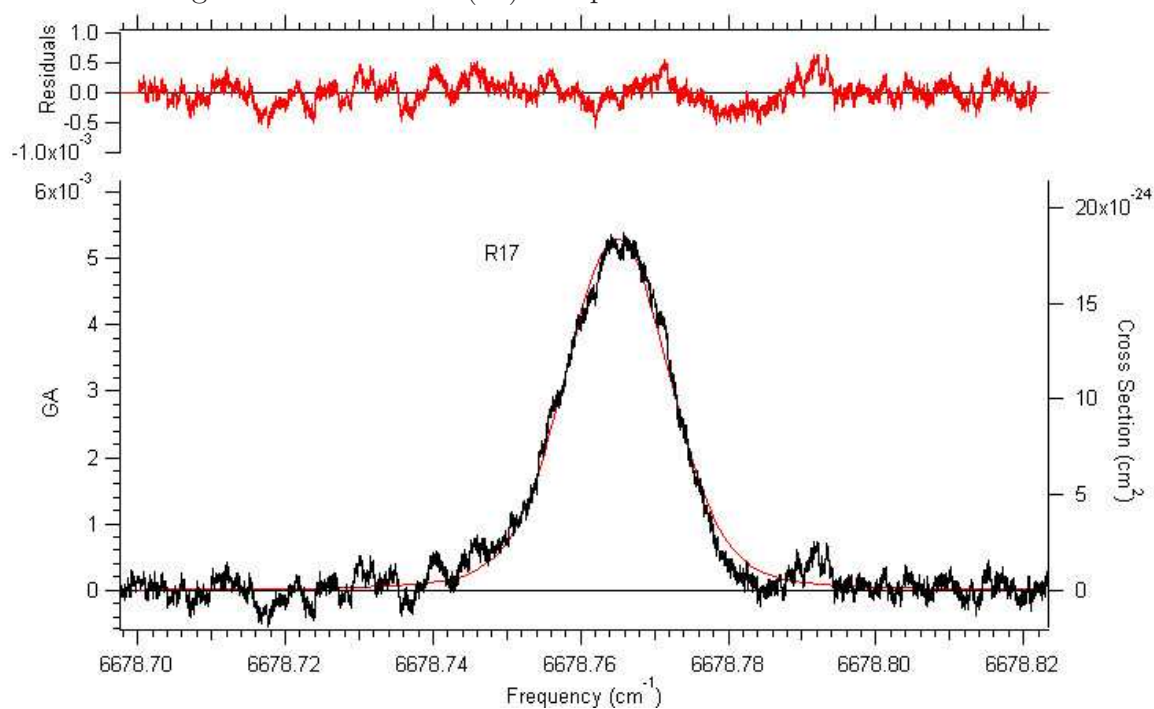


Figure C.19: The R(17) line position at $6678.7650 \text{ cm}^{-1}$.

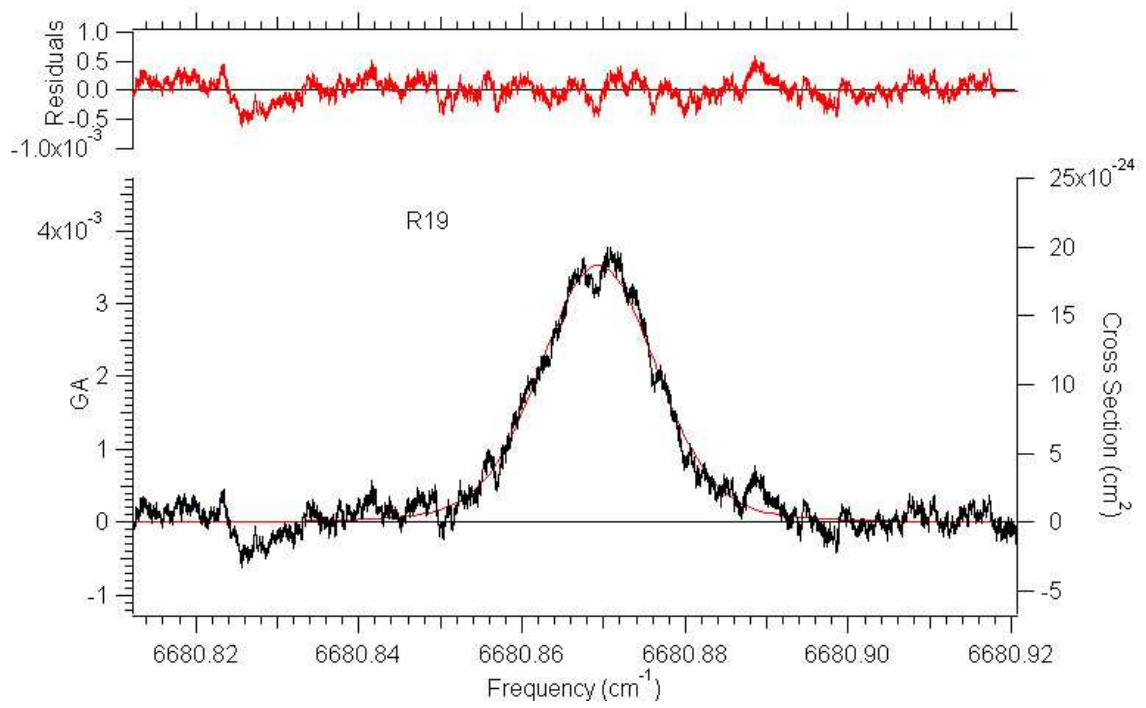


Figure C.20: The R(19) line position at 6680.8693cm^{-1} .

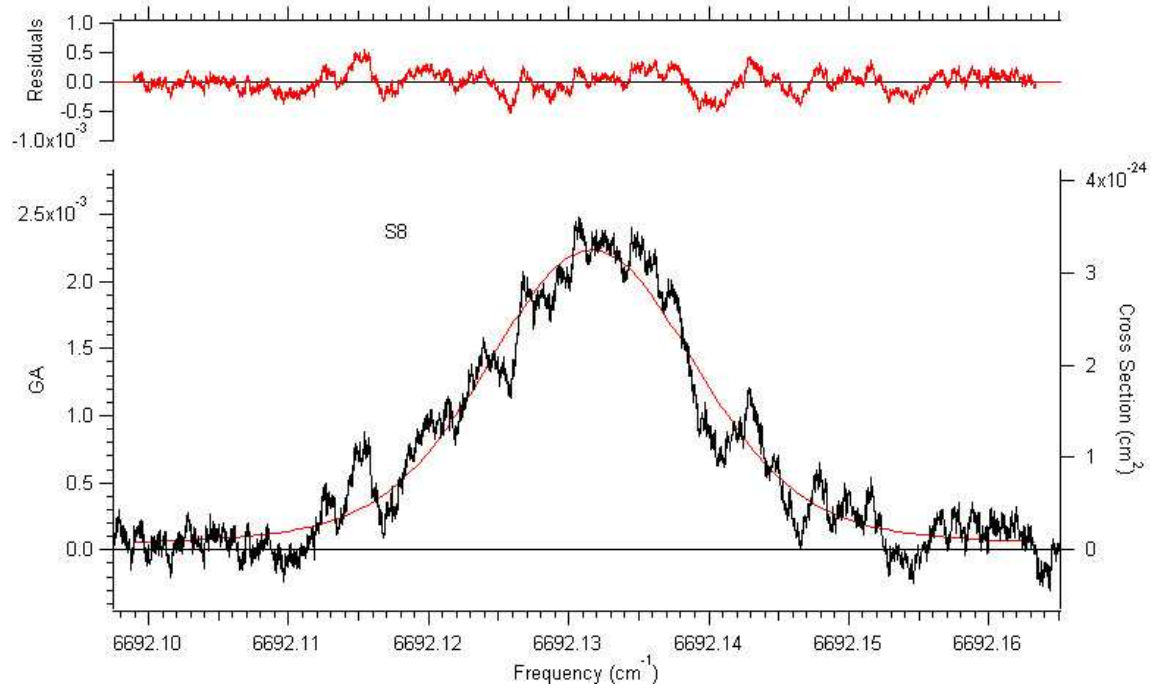


Figure C.21: The S(8) line position at 6692.1316cm^{-1} .

Appendix D. Developing the Hamiltonian

This section describes the various approximations used in quantum mechanics which lead up to the rotation-electronic interaction approximation listed in Hund's cases (a-e). The Hamiltonian for Hund's case (a) will then be briefly mentioned, since this was the Hamiltonian used by Cheah and Lee [27] to come up with their term energies $b^1\Sigma_g^+ \leftarrow X^3\Sigma_g^-$ and $a^1\Delta_g \leftarrow X^3\Sigma_g^-$, and ultimately was used in this experiment to derive the predicted line positions for $b^1\Sigma_g^+ \leftarrow a^1\Delta_g$. Recall that the case (b) Hamiltonian describes the $b^1\Sigma_g^+ \leftarrow a^1\Delta_g$ transition directly, however spectroscopic constants do not yet exist, so the case (b) could not be used in this experiment to determine the line positions.

D.1 The Rigid Rotor to the Case (a) Hamiltonian

Considering rotation only, a good first order approximation of the eigenenergies produced by the homonuclear diatomic is to treat it as a rigid rotor. The molecule can then be seen as two like masses connected by a rigid rod. When rotation occurs the eigenenergies are simply [8],

$$E = \frac{h^2 J(J+1)}{8\pi^2 \mu r_e^2} \quad (\text{D.1})$$

Where μ is the reduced mass of the molecule and r_e is the distance between the two atoms. If the term energies are defined as $F(J) = \frac{E}{hc}$ and the moment of inertia defined as $I = \mu r_e^2$, then the rotational constant, B , can be written as

$$B_e = \frac{h}{8\pi^2 c I} \quad (\text{D.2})$$

However, molecules are not rigid, so a better model must now be considered. If instead the atoms of the diatomic are connected by a spring, then this describes the non-rigid rotor approximation. In this configuration, any increase in rotation will achieve an increase in its moment of inertia. As a result, centrifugal distortion occurs. The centrifugal distortion constant D_e is dependent on the equilibrium vibration

frequency, ω_e [8].

$$D_e = \frac{4B_e^3}{\omega_e^2} \quad (\text{D.3})$$

Equation D.1 then becomes,

$$F(J) = B_e J(J+1) - D_e [J(J+1)]^2 \quad (\text{D.4})$$

Equation D.4 adequately describes the energy levels of a rotating diatomic whose potential energy curve is modeled by the harmonic oscillator. However, when vibration is present, the distance between the two atoms in the diatomic increase and decrease from their equilibrium position. The harmonic oscillator is only a good approximation for energy levels at or close to the equilibrium position. Real molecules must therefore be modeled after the anharmonic oscillator.

Considering vibration only, the eigenvalues for the anharmonic oscillator are [8],

$$E_v = hc\omega_e(v + \frac{1}{2}) - hc\omega_e\chi_e(v + \frac{1}{2})^2 + hc\omega_e y_e(v + \frac{1}{2})^3 \quad (\text{D.5})$$

Where $\omega_e\chi_e$ and $\omega_e y_e$ are simply coefficients to the quadratic and cubic terms, and v is the vibrational state. Writing equation D.5 in terms of term energies ($G(v)$),

$$G(v) = \omega_e \left(v + \frac{1}{2}\right) - \omega_e\chi_e \left(v + \frac{1}{2}\right)^2 + \omega_e y_e \left(v + \frac{1}{2}\right)^3 \quad (\text{D.6})$$

Another term which is used often in spectroscopy is ν_0 .

$$\nu_0 = G(\nu') - G(\nu'') \quad (\text{D.7})$$

This is the vibrational term that describes the energy difference between an upper and lower vibrational state.

An even more realistic model of the diatomic is the vibrating rotator, which involves vibration, rotation, and the interaction between them. If there didn't exist an interaction, the corresponding energy of the vibrating rotator would simply be the sum of equations D.4 and D.6. However, during vibration the internuclear distance will change, which then changes the molecule's moment of inertia, and in turn changes the molecule's rotational constant B_e of equation D.2. Since the period of vibration is very small compared to that of the period of rotation, a mean B_e value for the rotational constant in the vibrational state can be used. In other words, as v increases the molecule spends more of its time at large r where the potential energy curve is flatter. Thus the average internuclear separation $\langle r \rangle$ increases with v , while B_v decreases [8].

$$B_v = \frac{h}{8\pi^2 c \mu} \left\langle \frac{1}{r^2} \right\rangle \quad (\text{D.8})$$

The above equation is parameterized using wave-mechanical calculation to obtain [8],

$$B_v = B_e - \alpha_e \left(v + \frac{1}{2} \right) + \gamma_e \left(v + \frac{1}{2} \right)^2 \quad (\text{D.9})$$

Where α_e and γ_e are just coefficients. The same process is performed for the centrifugal distortion constant,

$$D_v = D_e - \beta_e \left(v + \frac{1}{2} \right) \quad (\text{D.10})$$

Where β_e is also a coefficient. Substituting the constants at equilibrium for their vibration-rotation interaction counterparts, equation D.4 can then be expressed as,

$$F(J) = B_v J(J+1) - D_v [J(J+1)]^2 \quad (\text{D.11})$$

There is still another model which more accurately describes the energy levels for a homonuclear diatomic, because the interaction between the rotational and elec-

tronic motions must also be considered. Hund was the first to categorized the different coupling schemes between the rotational and electronic motions. In fact, Hund discovered that there are five ways for rotational and electronic motions to couple to each other. These are the five well known cases (a-e).

Hund's case (a) states that the electronic motion of the molecule, which includes both the orbital and spin angular momentum, is strongly coupled to the internuclear axis (the axis of rotational symmetry). This coupling scheme is very similar to the symmetric top. Therefore the ro-vibronic energy of a molecule in Hund's case (a) has the form of the symmetric top. Returning to equation D.1 and including the symmetric top energy,

$$F(J) = B_e J(J+1) + (A - B_e)\Lambda^2 \quad (\text{D.12})$$

Where $A\Lambda^2$ can be understood as the spin-orbit coupling term [25], but since $S=0$ for singlet states (i.e. $^1\Sigma$ and $^1\Delta$), then $A=0$. Therefore, equation D.12 reduces to,

$$F(J) = B_v[J(J+1) - \Lambda^2] \quad (\text{D.13})$$

The final Hamiltonian used by Cheah and Lee, includes the symmetric top (equation D.13, the vibrating rotator D.11 and the vibrational term D.7 [27],

$$F(J) = \nu_0 + B_0[J(J+1) - \Lambda^2] - D_0[J(J+1) - \Lambda^2]^2 \quad (\text{D.14})$$

Bibliography

1. Alfano, Angelo J. and Karl O. Christe. "Singlet Delta Oxygen Production from a Gas-Solid Reaction". *Angewandte Chemie*, 114(17):3386–3388, 2002.
2. Bernath, Peter F. *Spectra of Atoms and Molecules*. Oxford University Press, New York, NY, first edition, 1995.
3. Chiu, Ying-Nan. "Electric-Quadrupole and Magnetic-Dipole Radiation in Linear Molecules. Applications to $^1\Pi - ^3\Pi$ Transitions". *Journal of Chemical Physics*, 42(8):2671–2681, November 1964.
4. Demtröder, Wolfgang. *Laser Spectroscopy: Basic Concepts and Instrumentation*. Springer, Kaiserslautern, Germany, second enlarged edition, 1998.
5. D.S. Baer, M. Gupta-A. O’Keefe, J.B. Paul. "Sensitive absorption measurements in the near-infrared region using off-axis integrated-cavity-output spectroscopy". *Applied Physics B*, 75:261–265, 2002.
6. Fink, E.H., H. Kruse, D.A. Ramsay, and M. Vervlot. "An electric quadrupole transition: the $b^1\Sigma_g^+ \rightarrow a^1\Delta_g$ emission system of oxygen". *Canadian Journal of Physics*, 64:242–245, October 1986.
7. H.C. Miller, J. Choy-G.D. Hager, J.E. McCord. "Measurement of the radiative lifetime of $O_2(a^1\Delta_g)$ using cavity ring down spectroscopy". *Journal of Quantitative Spectroscopy & Radiative Transfer*, 69:305–325, May 2001.
8. Herzberg, Gerhard. *Molecular Spectra and Molecular Structure*. Krieger Publishing Company, Malabar, FL, second edition, 1989.
9. Hilborn, Robert C. "Einstein coefficients, cross sections, f values, dipole moments, and all that". *American Journal of Physics*, 50(11):982–986, August 1981.
10. J. I. Steinfeld, G. Millot G. Fanjoux, P. Ruttenberg and B. Lavorel. "Scaling laws for inelastic collision processes in diatomic molecules". *Journal of Physical Chemistry*, 95(1):9638–9647, 1991.
11. J.J. Scherer, A. O’Keefe, J.B. Paul and J. Saykally. "Cavity Ringdown Laser Absorption Spectroscopy: History, Development, and Application to Pulsed Molecular Beams". *Chemical Review*, 97:25–51, 1997.
12. Joshua B. Paul, Larry Lapson and James G. Anderson. "Ultrasensitive absorption spectroscopy with a high-finesse optical cavity and off-axis alignment". *Applied Optics*, 40(27):4904–4910, September 2001.
13. Manish Gupta, Douglas S. Baer Anthony O’Keefe Skip Williams, Thomas Owano. "Quantitative determination of singlet oxygen density and temperature for Oxygen-Iodine Laser Applications". *Chemical Physics Letters*, 400:42–46, October 2004.

14. Martyn D. Wheeler, Andrew J. Orr-Ewing, Stuart M. Newman and Michael N.R. Ashfold. "Cavity ring-down spectroscopy". *Journal of the Chemical Society. Faraday Transactions*, 94(3):337–351, 1998.
15. Noxon, J.F. "Observation of the ($b^1\Sigma_g^+ \rightarrow a^1\Delta_g$) Transition in O_2 ". *Canadian Journal of Physics*, 39:1110–1119, May 1961.
16. O’Keefe, Anthony. "Integrated cavity output analysis of ultra-weak absorption". *Chemical Physics Letters*, 293:331–336, September 1998.
17. O.V. Braginski, et al. "Generation of singlet oxygen for an oxygen-iodine laser in a radio-frequency discharge". *Quantum Electronics*, 35(1):21–26, 2005.
18. Pazyuk, Raspopov, Podmar’kov and Frolov. *Quantum Electronics (Russian)*, 31:363, 2001.
19. Pope, Robert S. *Collisional Effects in the Absorption Spectra of the Oxygen A Band and Nitric Oxide Fundamental Band*. Ph.D. thesis, Graduate School of Engineering, Air Force Institute of Technology (AETC), Wright-Patterson AFB OH, March 1998. AFIT/DS/ENP/98-03.
20. Ranby, B. and J.F. Rabek. *Singlet Oxygen: Reactions with Organic Compounds and Polymers*. John Wiley & Sons, New York, NY, first edition, 1979.
21. Robert S. Pope, Glen P. Perram, Paul J. Wolf. "Collision broadening of rotational transitions in the O_2A band by molecular perturbers". *Journal of Quantitative Spectroscopy & Radiative Transfer*, 64:363–377, 2000.
22. Robert S. Pope, Glen P. Perram, Paul J. Wolf. "A study of collision broadening in the O_2 A-band with the noble gases using fourier transform spectroscopy". *Journal of Molecular Spectroscopy*, 223:205–213, 2004.
23. Romanini, D. and K.K. Lehmann. "Ring-down cavity absorption spectroscopy of the very weak HCN overtone bands with six, seven, and eight stretching quanta". *Journal of Chemical Physics*, 99(9):6287–6295, November 1993.
24. Skip Williams, Thomas Owano Douglas S. Baer-Anthony O’Keefe David R. Yarkony, Manish Gupta and Spiridoula Matsika. "Quantitative detection of singlet O_2 by cavity-enhanced absorption". *Optics Letters*, 29(10):1066–1068, May 2004.
25. Steinfeld, Jeffrey I. *Molecules and Radiation*. The MIT Press, Cambridge, MA, second edition, 1989.
26. Stuart M. Newman, David A. Newnham John Ballard, Andrew J. Orr-Ewing. "Temperature and Pressure Dependence of Line Widths and Integrated Absorption Intensities for the $O_2a^1\Delta_g \leftarrow X^3\Sigma_g^-$ (0,0) Transition". *Journal of Physical Chemistry A*, 104(42):9467–9480, August 2000.
27. Swee-Lan Cheah, Yuan-Pern Lee and J.F. Ogilvie. "Wavenumbers, strengths, widths and shifts with pressure of lines in four bands of gaseous 1O_2 in the systems

- $a^1\Delta_g \rightarrow X^3\Sigma_g^-$ and $b^1\Sigma_g^+ \rightarrow X^3\Sigma_g^-$ ". *Journal of Quantitative Spectroscopy & Radiative Transfer*, 64:467–482, 2000.
28. Wangsness, Roald K. *Electromagnetic Fields*. John Wiley & Sons, University of Arizona, 2nd edition edition, 1986.
 29. Wasserman, Harry H. and Robert W. Murray. *Singlet Oxygen*. Academic Press, New York, NY, first edition, 1979.

REPORT DOCUMENTATION PAGE					<i>Form Approved</i> <i>OMB No. 0704-0188</i>	
The public reporting burden for this collection of information is estimated to average 1 hour per response, including the time for reviewing instructions, searching existing data sources, gathering and maintaining the data needed, and completing and reviewing the collection of information. Send comments regarding this burden estimate or any other aspect of this collection of information, including suggestions for reducing this burden to Department of Defense, Washington Headquarters Services, Directorate for Information Operations and Reports (0704-0188), 1215 Jefferson Davis Highway, Suite 1204, Arlington, VA 22202-4302. Respondents should be aware that notwithstanding any other provision of law, no person shall be subject to any penalty for failing to comply with a collection of information if it does not display a currently valid OMB control number. PLEASE DO NOT RETURN YOUR FORM TO THE ABOVE ADDRESS.						
1. REPORT DATE (DD-MM-YYYY) 23-03-2006		2. REPORT TYPE Master's Thesis		3. DATES COVERED (From — To) July 2005 — Mar 2006		
4. TITLE AND SUBTITLE Singlet Delta Oxygen: A Quantitative Analysis Using Off-Axis Integrated-Cavity-Output-Spectroscopy (ICOS)				5a. CONTRACT NUMBER 5b. GRANT NUMBER 5c. PROGRAM ELEMENT NUMBER 5d. PROJECT NUMBER 5e. TASK NUMBER 5f. WORK UNIT NUMBER		
6. AUTHOR(S) Jeffrey E. Gallagher, Capt, USAF				8. PERFORMING ORGANIZATION REPORT NUMBER AFIT/GAP/ENP/06-05		
7. PERFORMING ORGANIZATION NAME(S) AND ADDRESS(ES) Air Force Institute of Technology Graduate School of Engineering and Management 2950 Hobson Way WPAFB OH 45433-7765				10. SPONSOR/MONITOR'S ACRONYM(S) 11. SPONSOR/MONITOR'S REPORT NUMBER(S)		
9. SPONSORING / MONITORING AGENCY NAME(S) AND ADDRESS(ES) Skip Williams Air Force Research Laboratory Propulsion Directorate 1950 Fifth Street WPAFB OH 45433-7251				12. DISTRIBUTION / AVAILABILITY STATEMENT Approval for public release; distribution is unlimited		
13. SUPPLEMENTARY NOTES						
14. ABSTRACT Off-axis integrated-cavity-output spectroscopy (ICOS) has been applied to detect singlet oxygen in the (1,0) band of the electric-quadrupole allowed Noxon system ($b^1\Sigma_g^+ \leftarrow a^1\Delta_g$) of oxygen. Absolute line positions were determined for 21 lines to within 0.004cm^{-1} . Ten of these lines were pressure broadened from 25 to 100 torr, and pressure broadening coefficients were determined from $\gamma_p = 3.61 \times 10^{-6}\text{cm}^{-1}/\text{torr}$ to $5.81 \times 10^{-6}\text{cm}^{-1}/\text{torr}$. The singlet oxygen was generated in a microwave plasma and the off-axis ICOS measurement system consisted of an 82-cm long high-finesse (≈ 248000) optical cavity. The mirror reflectivity, R , was determined using a cavity ringdown measurement and observing ringdown times of 220 μs in a range from 1494 nm to 1512 nm. The absorption within the cavity leads to a decrease in transmitted intensity, ΔI , given by $\Delta I/I_o = GA/(1 + GA)$, where I_o is incident laser intensity, A is the single pass absorption ($\approx 5 \times 10^{-8}$), and $G = 2R^2/(1 - R^2) \approx 80,000$ is the cavity enhancement factor.						
15. SUBJECT TERMS cavity enhancement factor, cavity ringdown, electric-quadrupole transition, off-axis ICOS, singlet delta oxygen						
16. SECURITY CLASSIFICATION OF:			17. LIMITATION OF ABSTRACT UU	18. NUMBER OF PAGES 111	19a. NAME OF RESPONSIBLE PERSON Glen P Perram	
a. REPORT U	b. ABSTRACT U	c. THIS PAGE U			19b. TELEPHONE NUMBER (include area code) (937) 255-3636, ext 4504	